COLLISION-INDUCED ABSORPTION SPECTRA OF H_2 IN THE FIRST OVERTONE REGION AND THE FUNDAMENTAL BAND OF D_2 IN BINARY MIXTURES: D_2-N_2, D_2-CO, D_2-He, D_2-Ar AND D_2-Kr

CLIFFORD FRANCIS JOSEPH STAMP

COLLISION-INDUCED ABSORPTION SPECTRA OF H_2 IN THE FIRST OVERTONE REGION AND THE FUNDAMENTAL BAND OF D_2 IN BINARY MIXTURES : D_2-N_2, D_2-CO, D_2-He, D_2-Ar and D_2-Kr

By

©Clifford Francis Joseph Stamp

A THESIS SUBMITTED IN PARTIAL
FULFILLMENT OF THE REQUIREMENTS
FOR THE DEGREE OF
DOCTOR OF PHILOSOPHY

DEPARTMENT OF PHYSICS AND PHYSICAL OCEANOGRAPHY
MEMORIAL UNIVERSITY OF NEWFOUNDLAND
MARCH, 2006

ST. JOHN'S NEWFOUNDLAND

Acknowledgements

I express my appreciation to my supervisor, Professor S. P. Reddy for his guidance and encouragement throughout the progress of this research project and in the preparation of this thesis.

I would like to thank Dr. Paul Gillard for his help in the experimental work, numerical analysis, computer programming, and some theoretical considerations. I would also like to thank Dr. J. C. Lewis for very helpful discussions pertaining to various theoretical considerations and numerical analysis. Thanks are also given to Dr. George Varghese for assistance in the experimental work and proofreading of the thesis.

I also acknowledge the financial support received from Professor Reddy's NSERC grant, and am grateful to Memorial University of Newfoundland for the support in the form of a Graduate Fellowship.

Abstract

The present research project consisted of three distinct spectral regions of study. First there was a refinement to the spectral analysis of the collision-induced absorption (CIA) spectra of the first overtone band of hydrogen. This consisted primarily of an investigation of the density dependence of the so-called "fudge factor" by use of various semi-empirical line shapes.

The second part was an analysis of the CIA of the fundamental band of D_2 in D_2-N_2 and D_2-CO mixtures. The absorption coefficients were determined using appropriate statistical methods applied to a density expansion of the integrated absorption of the spectra, as well as calculation of the characteristic parameters of various semi-empirical line shapes applied to the experimental data.

The third part of the thesis consisted of a systematic study of the CIA spectra of the fundamental band of D_2 enhanced by He, Ar, and Kr at room temperature. The absorption coefficients were determined using appropriate statistical methods applied to a density expansion of the integrated absorption of the spectra, and the characteristic parameters of various semi-empirical line shapes were deduced from a nonlinear fitting procedure applied to the experimental data.

During the course of the above work, the FORTRAN programs used to transform the raw data into the desired numerical quantities and complete the necessary analysis were updated and as necessary completely rewritten to advance the data analysis. This work was commenced in earnest during the author's M.Sc. thesis with the goal being to maximize the robust nature of the analysis and propagation of errors throughout all calculations to obtain maximum reliability in the results[1].

Contents

List of Tables

List of Figures

Chapter 1

Introduction

Isolated homonuclear diatomic molecules, H_2, D_2, N_2, and O_2, etc., in their lowest (ground) electronic states have no permanent static or oscillatory electronic dipole moments because of the symmetry of charge distribution. Consequently, they have no electric dipole absorption at their translational, rotational, or vibrational frequencies. But they do have higher order multipole moments such as quadrupole, hexadecapole, and tetrahexadecapole moments. Collision-induced absorption(CIA) occurs as a result of induced transient electric dipole moments during binary or higher-order collisions. The mechanisms include a short-range electron overlap interaction arising from the distortion of the electron clouds and various multipole induction mechanisms. As a result peaks are seen in CIA spectra due to normally forbidden translational and vibrotatonal-rotational transitions.

Collision-induced absorption was first observed in 1949 in compressed N_2 and O_2 in the region of their fundamental bands by Crawford, Welsh and Locke[2]. The CIA of the fundamental band of gaseous H_2 was first identified by Welsh, Crawford and Lock in the same year. The H_2 molecule and its isotopomers such as D_2 and T_2 occupy a unique place in molecular physics on account of their simplicity and in particular the abundance of H_2 in the universe and the accessibility to both experiment and theoretical studies. Molecules of this class can be considered as benchmarks in the field of CIA.

The electric dipole moment induced in a pair of homonuclear diatomic molecules during a collision is a function of the intermolecular separation R and the relative orientation

of each molecule with respect to R. This induced dipole moment μ can be represented as a sum of (i) a short-range electron-overlap isotropic moment with $\mu_{overlap}$ having an exponential dependence, (ii) a short-range anisotropic overlap component similar to (i), (iii) a long-range, quadrupole-induced and angle-dependent moment, μ_{quad}, proportional to R^{-4}, and (iv) an intermediate range, hexadecapole-induced and angle-dependent moment, μ_{hexa}, proportional to R^{-6}. The first and third parts have been taken into account in the the "exponential-4 model"[3]. The first part gives rise mainly to the broad $Q_{overlap}$ ($\Delta J = 0$) transitions, J being the rotational quantum number. The third part gives rise to the relatively less broad transitions O ($\Delta J = -2$), Q_{quad} ($\Delta J = 0$) and S ($\Delta J = +2$). For the induced fundamental band, the quadrupolar induction arising from the isotropic part of the polarizability contributes to the intensity of the transitions of the type, $O_1(J) + Q_0(J)$, $Q_1(J) + Q_0(J)$, $S_1(J) + Q_0(J)$, and $Q_1(J) + S_0(J)$. The anisotropic polarizability contributes to the intensity of transitions of the form $S_1(J) + S_0(J)$. The hexadecapolar part of the dipole moment gives rise to the transitions of $\Delta J = 0, \pm 2, \pm 4, +4$ gives rise to the the U transitions and the tetrahexadecapole moment gives rise to the transitions $\Delta J = 0, \pm 2, \pm 4 \pm 6$ and $+6$ gives rise to the W transitions.

For CIA first overtone band, the isotropic overlap induction mechanism is found to give no visible contribution to the absorption. This is due to the mechanism being forbidden for like pairs so the 1-1 transisions have no isotropic overlap contribution, and the contribution from the 0-2 transitions is not significant due to the much reduced matrix elements for the overtone in comparison to the fundamental band[4]. The isotropic part of the polarizability contributes to the intensity of the transitions of the type $O_2(J) + Q_0(J)$, $Q_2(J) + Q_0(J)$, $S_2(J) + Q_0(J)$, $O_1(J) + Q_1(J)$, $Q_1(J) + Q_1(J)$, $S_1(J) + Q_1(J)$, $Q_2(J) + S_0(J)$ and $Q_1(J) + S_1(J)$. The anisotropic polarizability contributes to the intensity of transitions of the form $S_2(J) + S_0(J)$ and $S_1(J) + S_1(J)$. It is also proposed that the anisotropic overlap induction contributes to the transitions of the form $Q_2(J) + Q_0(J)$

and $Q_2(J) + S_0(J)$. Subscripts 0,1 and 2 represent $\Delta v = v' - v''$.

Welsh[5] has reviewed the experimental work done until 1971 on the translational, rotational and vibrational spectra of H_2 and D_2. The CIA vibrational spectra of the isotopomers H_2, D_2 and HD have been reviewed in detail by Reddy[6]. The reader is referred to these reviews for experimental aspects of the CIA and to Van Kranendock[7, 3, 8, 9], Lewis[10], Poll[11], Birnbaum et al[12, 13] and Fromhold[4] and the references therein for the theoretical aspects. A comprehensive bibliography on CIA has been compiled by Rich and McKellar[14].

For the first stage of the present work, enhancement CIA spectra of the infrared fundamental band of D_2 in D_2-N_2 and D_2-CO binary mixtures previously recorded at 298 K with an absorption cell of sample path length 105.2 cm were studied. Five base densities of D_2 in the range 12-20 amagat and several total gas densities of the mixtures up to 130 amagat were used. The observed spectra show the usual characteristic dip near the band origin $Q_1(0)$ of the Q branch with two well resolved components Q_P and Q_R as well as the absorption peaks $O_1(3)$, $O_1(2)$ and $S_1(J)$, J=0 to 4. Binary and ternary absorption coefficients of the band arising from collisions of the type D_2-X and D_2-X-X where X stands for N_2 or CO have been determined. The spectra are interpreted in terms of the overlap transitions $Q_{ov}(J)$, J=0 to 4 and the following quadrupolar transitions of D_2-N_2 and D_2-CO : $O_1(1)(D_2)+Q_0(J)(N_2/CO)$; $Q_1(1)(D_2)+Q_0(J)(N_2/CO)$; $S_1(1)(D_2)+Q_0(J)(N_2/CO)$; $Q_1(1)(D_2)+S_0(J)(N_2/CO)$; with J=0 to 4 for D_2 and J=0 to 25 for N_2 / CO. An analysis of the absorption profiles was carried out by assuming appropriate line shape functions for the short range overlap and long range quadrupolar contributions. Characteristic half-width parameters δ_d and δ_c for the overlap induction transitions and δ_q for the quadrupole induced transitions were obtained from the profile analysis. Although CO has a small permanent electric dipole, the present analysis does not indicate that it makes any measurable contribution to the absorption in the D_2-CO

mixtures. The results of this work has recently been published[15].

In the second stage of the thesis, non-linear least squares fits were performed on CIA spectra of the pure gas of hydrogen at three temperatures, 77, 201 and 295 K, and 48 different densities to study the "fudge factor" used by van Nostrand[16] to explain an observed systematic discrepancy between the observed band and the calculated transition intensities in the first overtone band. This correction method was introduced by Gillard[17] who noted a similar problem with the first overtone band of deuterium. With use of the Birnbaum-Cohen lineshape function all 48 experimental profiles were fitted including the correction factor as a variable in the fitting to investigate any correlation of the magnitude of the factor to the density and temperature of the gas. It was found that as both density and temperature decreased the magnitude of the correction factor increased but did not extrapolate back to one, which would be no correction. The new lineshape also gave a better match overall to the spectra.

As the final stage, enhancement CIA spectra of the fundamental band of D_2 in D_2-He, D_2-Ar and D_2-Kr, binary mixtures were recorded at 298 K with a 2m absorption cell. Sixty four mixture densities were studied in total for the three binary mixtures. The observed spectra show the usual characteristic dip near the band origin $Q_1(0)$ of the Q branch with two well resolved components Q_P and Q_R as well as the absorption peaks $O_1(3)$, $O_1(2)$ and $S_1(J)$, J=0 to 4. Binary and ternary absorption coefficients of the band arising from collisions of the type D_2-X and D_2-X-X where X stands for He, Ar or Kr have been determined. The spectra are interpreted in terms of the overlap transitions $Q_{ov}(J)$, J=0 to 4 and the following quadrupolar transitions of D_2-He, and D_2-Ar, and D_2-Kr : $O_1(1)(D_2)+Q_0(J)(He/Ar/Kr)$; $Q_1(1)(D_2)+Q_0(J)(He/Ar/Kr)$; $S_1(1)(D_2)+Q_0(J)(He/Ar/Kr)$; with J=0 to 4 for D_2 and He, Ar, Kr making orientational transitions. An analysis of the absorption profiles was carried out by assuming

appropriate line shape functions for the short range overlap and long range quadrupolar contributions. Characteristic half-width parameters δ_d and δ_c for the overlap transitions and δ_q for the quadrupole induced transitions were obtained from the profile analysis.

Chapter 2

Theory of collision-induced absorption and spectral lineshapes

2.1 Induction Mechanisms in Molecular Collisions

For a collision of two symmetric diatomic molecules the coordinate system is schematically shown in Figure 2.1(a). The induced dipole moment $\vec{\mu}$ is a function of the internuclear molecular separations $\vec{r}_1$ and $\vec{r}_2$ and the intermolecular separation $\vec{R}$ as :

$$\vec{\mu} = \vec{\mu}(\vec{r}_1, \vec{r}_2, \vec{R}) \ , \tag{2.1}$$

where $\vec{r}_1 = (r_1, \omega_1)$ and $\vec{r}_2 = (r_2, \omega_2)$ represent the orientation of the internuclear axes of molecule 1 and 2, respectively, and $\vec{R} = (R, \Omega)$ the separation between their centers of mass along the z-axis. A collision between a symmetric diatomic molecule and a monoatomic molecule is shown in Figure 2.1(b) and the expression for $\vec{\mu}$ is represented simply by

$$\vec{\mu} = \vec{\mu}(\vec{r}, \vec{R}) \ . \tag{2.2}$$

In detail, the spherical components μ_ν of the induced dipole moment for a colliding pair of molecules 1 and 2 in a space-fixed coordinate system can be written as[18, 19] :

$$\begin{aligned} \mu_\nu(\vec{r}_1, \vec{r}_2, \vec{R}) \ = \ & \frac{(4\pi)^{3/2}}{\sqrt{3}} \Sigma_{\lambda_1 \lambda_2 \Lambda L} A_\Lambda(\lambda_1 \lambda_2 L; r_1 r_2 R) \\ & \Sigma_{\mu_1 \mu_2 M} C(\Lambda L 1; \mu_1 + \mu_2, M, \nu) C(\lambda_1 \lambda_2 \Lambda; \mu_1, \mu_2, , \mu_1 + \mu_2) \\ & Y_{\lambda_1, \mu_1}(\omega_1) Y_{\lambda_2, \mu_2}(\omega_2) Y_{L,M}(\Omega) \ , \end{aligned} \tag{2.3}$$

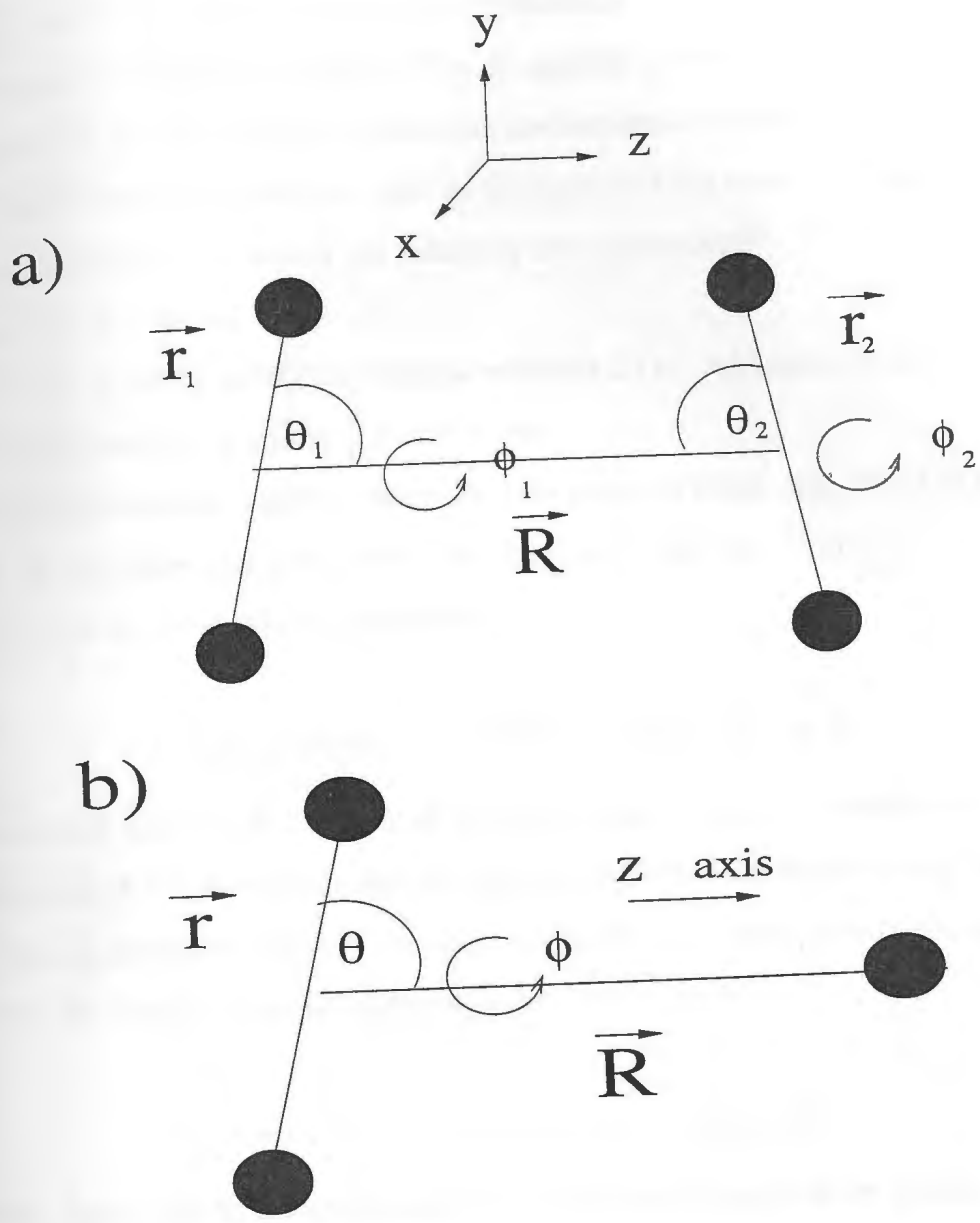

Figure 2.1: A schematic representation of a collision between (a) two symmetric diatomic molecules and (b) a symmetric diatomic molecule and a monoatomic molecule. See the text for details of the symbols.

where the C's are the Clebsch-Gordan coefficients[20], Y's are the spherical harmonics, and $A_\Lambda(\lambda_1\lambda_2 L; r_1 r_2 R)$'s are the expansion coefficients of the dipole moment which are real functions of the radial variables. The A's provide a coordinate-independent representation of the strength of various induction mechanisms specified by the indices λ_1, λ_2, Λ and L and whose R dependence rests on the nature of the induction mechanism. The expansion coefficients A's satisfy the following five constraints[21, 22] :

(i)$\lambda_1 + \lambda_2 + L$ is odd ,

(ii)λ_1 , λ_2, Λ and L satisfy the triangle relations $\Delta(\lambda_1, \lambda_2\Lambda)$ and $\Delta(\Lambda L1)$,

(iii)A_Λ are real for all values of λ and L, and

(iv) for homonuclear diatomic molecules only even λ's occur, and thus L is odd from relation (i). For molecules such as HD odd values of λ also can occur.

(v) for two identical diatomic molecules

$$A_\Lambda(\lambda_1\lambda_2 L; r_1 r_2 R) = (-1^{\lambda_1+\lambda_2-\Lambda+L}) A_\Lambda(\lambda_2\lambda_1 L; r_2 r_1 R). \tag{2.4}$$

The matrix element of the induced dipole moment $< |\mu| >$ represents the physical manifestation of the absorption, and for the induced vibration bands arising from collisions between molecules 1 and 2, the expansion coefficients of the matrix elements B are related to the dipole expansion coefficients A by the expression

$$B_\Lambda(\lambda_1\lambda_2 L; R) = < v_1, v_2 | A_\Lambda(\lambda_1\lambda_2 L; r_1 r_2 R) | v_1', v_2' > . \tag{2.5}$$

Concisely $B_\Lambda(\lambda_1\lambda_2 L; R)$ is written as $B_{L\Lambda}(R)$. The matrix elements are usually expressed in atomic units with the various induction mechanisms represented by the appropriate B which is specified by the indices L and Λ. For $L = 1$ there is the isotropic overlap component which is represented by

$$B_{10}(R)/ea_0 = \lambda_{10} \exp[-(R-\sigma)/\rho_{10}] \,, \tag{2.6}$$

and the anisotropic overlap component is expressed as

$$B_{12}(R)/ea_0 = \lambda_{12} \exp[-(R-\sigma)/\rho_{12}]. \tag{2.7}$$

For L=3 the anisotropic overlap and isotropic quadrupolar component is represented by [21]

$$B_{32}(R)/ea_0 = [\lambda_{32} \exp[-(R-\sigma)/\rho_{32}] + \sqrt{3} < vJ|\Lambda|v'J' >< vJ|Q|v'J' >](R/a_0)^{-4}. \tag{2.8}$$

In equation 2.8 the exponential term corresponds to the anisotropic overlap induction and the R^{-4} term corresponds to the quadrupolar induction. As the absorption coefficient is proportional to the squares of these coefficients, for the L=3 term the following three factors occur :

$$3 < vJ|\alpha|v'J' >^2 < vJ|Q|v'J' >^2 (R/a_0)^{-8} \tag{2.9}$$

(major term)

$$\lambda_{32}^2 \exp[-2(R-\sigma)/\rho_{32}] \tag{2.10}$$

(term with small value), and

$$2\sqrt{3}\lambda_{32} \exp[-(R-\sigma)/\rho_{32}] < vJ|\alpha|v'J' >< vJ|Q|v'J' > (R/a_0)^{-4} \,. \tag{2.11}$$

(mixed term)

From the work presented in the first overtone band of H_2 (as well as higher overtone bands), the mixed term is found to contribute negatively to the quadrupolar transitions ($\Delta v = 2$) and represents a type of destructive interference.

2.2 Absorption Coefficients

The strength of the absorption produced via the various induction mechanisms at a specific wavenumber ν (in cm^{-1}) is defined as the absorption coefficient $\alpha(\nu)$ which is written as

$$I(\nu) = I_0(\nu)e^{-\alpha(\nu)l}, \tag{2.12}$$

where $I_0(\nu)$ is the transmitted intensity of the source radiation through an evacuated cell of sample path length l, and $I(\nu)$ the transmitted intensity through the cell which contains the gas at a given density.

For collision induced absorption in a pure gas the above absorption coefficient is readily understood to represent induced absorption from binary, ternary and higher order interactions between molecules of the same gas. However when studying collision absorption in binary gas mixtures between two gases of type a and b, the absorption coefficient has multiple components and thus equation 2.12 is expanded

$$I_2(\nu) = I_0(\nu)e^{-[\alpha_{aa}(\nu)+\alpha_{ab}(\nu)+\alpha_{bb}(\nu)]l}, \tag{2.13}$$

where $I_2(\nu)$ is the transmitted intensity through the cell which contains the binary mixture gas at a given density, and $\alpha_{aa}(\nu)$, $\alpha_{ab}(\nu)$, and $\alpha_{bb}(\nu)$ are absorption coefficients arising from interactions of molecules of gas a with molecules of gas a, molecules of gas a

with molecules of gas b, and molecules of gas b with molecules of gas b, respectively. To eliminate $\alpha_{aa}(\nu)$, the absorption coefficient of the "base" gas from equation 2.13, $I_1(\nu)$ is defined as

$$I_1(\nu) = I_0(\nu)e^{-\alpha_{aa}(\nu)l} \ . \tag{2.14}$$

Here $I_1(\nu)$ is the intensity transmitted through the cell containing the base gas at a specific density. This definition allows simplification of equation 2.13 to

$$I_2(\nu) = I_1(\nu)e^{-[\alpha_{ab}(\nu)+\alpha_{bb}(\nu)]l} \ . \tag{2.15}$$

If $\alpha_{bb}(\nu)$ is negligible in the region of interest of the $a-b$ induced spectra, which is the case for the mixtures studied here (in particular it is zero for the gases He, Ar, and Kr), this equation reduces to

$$I_2(\nu) = I_1(\nu)e^{-\alpha_{ab}(\nu)l} \ . \tag{2.16}$$

The absorption coefficient $\alpha_{ab}(\nu)$ can therefore be expressed as

$$\alpha_{ab}(\nu) = (1/l)\ln[I_1(\nu)/I_2(\nu)] \ . \tag{2.17}$$

This coefficient $\alpha_{ab}(\nu)$ can be determined experimentally from the measured intensities, $I_1(\nu)$ and $I_2(\nu)$. It can also be calculated theoretically by summing over all possible molecular transitions m from all possible induction mechanisms I as follows

$$\alpha_{ab}(\nu) = \sum_{Im} \alpha_{ab,Im}(\nu) \ . \tag{2.18}$$

Here $\alpha_{ab,Im}(\nu)$ represents the absorption from the mth transition of the induction mechanism I. For the D_2-X mixtures studied here, where X=He, Ar, Kr, N_2 and CO, the spectra observed are enhancements and thus $\alpha_{ab}(\nu)$ is referred to as $\alpha_{en}(\nu)$.

2.3 Integrated Absorption Coefficients

The integral of the absorption coefficient $\alpha(\nu)$ is defined as

$$A = \int \alpha(\nu) d\nu \tag{2.19}$$

and can be expanded in terms of density. For a pure gas this is written as

$$A = A_{aa}{\rho_a}^2 + A_{aaa}{\rho_a}^3 + \ldots, \tag{2.20}$$

where the expansion coefficients correspond to the influence of a particular order of collision; A_{aa} is the binary absorption coefficient arising from collisions of type $a-a$, and A_{aaa} is the the ternary absorption coefficient arising from collisions of type $a-a-a$. With a slight rearrangement of equation 2.20 a more straightforward relationship is produced. Keeping up to ternary coefficients in the density expansion, we have

$$(1/\rho_a^2)A = A_{aa} + A_{aaa}\rho_a + \ldots, \tag{2.21}$$

which produces a straight line graph whose intercept and slope give the binary and ternary absorption coefficients, A_{aa} and A_{aaa}, respectively.

For a binary mixture, the density expansion of the integrated enhancement absorption coefficient is dependent on the densities of both gases. For the mixtures studied here the spectra are pure enhancement and the expansion expressed as

$$A_{en} = \int \alpha_{en}(\nu) d\nu = A_{ab}\rho_a\rho_b + A_{abb}\rho_a{\rho_b}^2 + A_{aab}{\rho_a}^2\rho_b + \ldots, \tag{2.22}$$

where A_{ab} is the binary absorption coefficient arising from collisions of type $a-b$, and A_{abb} and A_{aab} are the ternary absorption coefficients arising from collisions of types $a-b-b$ and $a-a-b$, respectively. As before this equation can be rearranged to produce a linear plot if coefficients beyond ternary are neglected :

$$(1/\rho_a\rho_b)A_{en} = A_{ab} + A_{abb}\rho_b + A_{aab}\rho_a \ . \tag{2.23}$$

This can be rewritten as

$$(1/\rho_a\rho_b)A_{en} = (A_{ab} + A_{aab}\rho_a) + A_{abb}\rho_b \ . \tag{2.24}$$

When $(1/\rho_a\rho_b)A_{en}$ is plotted against ρ_b the resulting straight line produces an intercept $(A_{ab} + A_{aab}\rho_a)$ and a slope A_{abb}. Since the intercept is dependent on the density of the base gas, this is plotted against ρ_a which gives A_{aab} as the slope. Recently[23] an alternate method has been used in our laboratory by constructing a surface plot of the integrated absorption against both densities ρ_a and ρ_b and determining all absorption coefficients simultaneously. This method is significantly more robust and considers correlations between all coefficients.

These density expansions are also studied for the integrals of the dimensionless absorption coefficient $\tilde{\alpha}(\nu)$ $(= \alpha(\nu)/\nu)$ as it is more theoretically tractable. For a pure gas this gives

$$\tilde{A} = c\int \tilde{\alpha}(\nu)d\nu = \tilde{A}_{aa}{\rho_a}^2 n_0^2 + \tilde{A}_{aaa}{\rho_a}^3 n_0^3 + \ldots, \tag{2.25}$$

where the new coefficients are related to those in equation 2.20 via

$$\begin{aligned} \tilde{A}_{aa} &= \frac{(c/n_0^2)A_{aa}}{\overline{\nu}} \\ \tilde{A}_{aaa} &= \frac{(c/n_0^3)A_{aaa}}{\overline{\nu}}. \end{aligned} \tag{2.26}$$

Here c is the speed of light, n_0 is Loschmidt's number, 2.687x10^{19} cm^{-3} (the number of molecules per cubic centimeter of gas at STP), and $\overline{\nu}$ is the band center given by

$$\overline{\nu} = \frac{\int \alpha(\nu) d\nu}{\int \tilde{\alpha}(\nu) d\nu} \,. \tag{2.27}$$

Similarly the expansion for the enhancement is

$$\tilde{A}_{en} = c \int \tilde{\alpha}_{en}(\nu) d\nu = \tilde{A}_{ab} \rho_a \rho_b n_0^2 + \tilde{A}_{aab} {\rho_a}^2 \rho_b n_0^3 + \tilde{A}_{abb} \rho_a {\rho_b}^2 n_0^3 + \ldots , \tag{2.28}$$

and the relations for the coefficients are

$$\begin{aligned} \tilde{A}_{ab} &= \frac{(c/n_0^2) A_{ab}}{\overline{\nu}} \\ \tilde{A}_{aab} &= \frac{(c/n_0^3) A_{aab}}{\overline{\nu}} \\ \tilde{A}_{abb} &= \frac{(c/n_0^3) A_{abb}}{\overline{\nu}} \end{aligned} \tag{2.29}$$

2.4 Binary Absorption Coefficients

The frequency dependence of the absorption coefficient $\alpha(\nu)$ or $\tilde{\alpha}(\nu)$ cannot be expressed theoretically except for the simplest systems. However, the binary absorption coefficient $\tilde{A}_{ab}$ has been the focus of considerable theoretical work. For the gases studied in the present work there are only two significant absorption mechanisms and thus the binary absorption coefficient has two components

$$\tilde{A}_{ab} = \tilde{A}_{OvJ} + \tilde{A}_{Lm} \,, \tag{2.30}$$

where $\tilde{A}_{Ov}$ and $\tilde{A}_{Lm}$, are the contributions from the overlap and multipolar induction mechanisms, respectively. The overlap induction component is proportional to the normalized Boltzmann factor $P_J^{[3]}$:

$$\tilde{A}_{OvJ} \propto P_J \ , \tag{2.31}$$

where P_J is given by

$$P_J = \frac{g_T(2J+1)e^{-E_J/kT}}{\sum_J g_T(2J+1)e^{-E_J/kT}} \ , \tag{2.32}$$

where g_T is the nuclear statistical weight of the molecule in a given rotational state (J), g_T is 1 and 3 for even and odd J for H_2, and 6 and 3 for even and odd D_2 and N_2, respectively, and E_J is the rotational energy.

For multipole induction the binary absorption coefficient can be expressed in the most general form as[6, 24, 25]

$$\tilde{A}_{Lm} = \frac{4\pi^3 n_0^2 e^2}{3ch} {a_0}^5 (a_0/\sigma)^{2L+1} \tilde{J}_L X_{Lm}, \tag{2.33}$$

where

$$\tilde{J}_L = 4\pi(L+1)\int_0^\infty x^{-2(L+2)} g_0(x) x^2 dx, \tag{2.34}$$

$$\begin{aligned} X_{Lm} = P_{J_1}P_{J_2} \ [\ & C(J_1L_1J'_1;00)^2 C(J_20J'_2;00)^2 \\ & < v_1J_1|Q_{L_1}|v'_1J'_1 >^2 < v_2J_2|\alpha_2|v'_2J'_2 >^2 + \\ & C(J_2L_2J'_2;00)^2 C(J_10J'_1;00)^2 \\ & < v_2J_2|Q_{L_2}|v'_2J'_2 >^2 < v_1J_1|\alpha_1|v'_1J'_1 >^2] + Y_{Lm} \end{aligned} \tag{2.35}$$

and

$$Y_{Lm} = P_{J_1}P_{J_2} \ [\ C(J_1LJ'_1;00)^2 C(J_22J'_2;00)^2$$

$$\frac{2}{9} < v_1 J_1|Q_{L_1}|v'_1 J'_1 >^2 < v_2 J_2|\gamma|v'_2 J'_2 >^2 +$$
$$+ \quad C(J_1 2 J'_1; 00)^2 C(J_2 L J'_2; 00)^2$$
$$\frac{2}{9} < v_2 J_2|Q_{L_2}|v'_2 J'_2 >^2 < v_1 J_1|\gamma|v'_1 J'_1 >^2$$
$$- \quad \frac{4}{15} C(J_1 2 J'_1; 00)^2 C(J_2 2 J'_2; 00)^2$$
$$< v_1 J_1|Q_{L_1}|v'_1 J'_1 >< v_2 J_2|\gamma_2|v'_1 J'_2 >$$
$$< v_2 J_2|Q_{L_2}|v'_2 J'_2 >< v_1 J_1|\gamma_1|v'_1 J'_1 >]. \qquad (2.36)$$

In these equations, L sets the multipole order (2^L) , $L = 2$, for quadrupole, $L = 4$, for hexadecapole, $L = 6$ for tetrahexadecapole, etc., a_0 is the first Bohr radius, $g_0(x)$ is the pair correlation function for the gas and $x = R/\sigma$, where R is the intermolecular separation and σ is the intermolecular separation at potential V(0)=0. The subscripts 1 and 2 refer to the two colliding molecules; and $< |Q| >$,$< |\alpha| >$, and $< |\gamma| >$ are the matrix elements of the multipole moment, isotropic and anisotropic polarizability, respectively. As γ is small for H_2 or D_2, Y_{Lm} (equation 2.36) contributes a small amount to the main transitions $Q_{\Delta v}(J_1) + Q_{\Delta v}(J_2)$ $Q_{\Delta v}(J_1) + S_{\Delta v}(J_2)$ $Q_{\Delta v}(J_1) + O_{\Delta v}(J_2)$, etc., but accounts completely for the transitions of the type $S_{\Delta v}(J_1) + S_{\Delta v}(J_2)$[6]

The squares of the Clebsch-Gordan coefficients for the O ($\Delta J = -2$), Q ($\Delta J = 0$), and S ($\Delta J = +2$) transitions are given by the following equations[20] :

$$Q \ : \ C(J0J'; 00)^2 = \delta_{JJ'}$$
$$O \ : \ C(J2J-2; 00)^2 = \frac{3J(J-1)}{2(2J-1)(2J+1)}$$
$$Q \ : \ C(J2J; 00)^2 = \frac{J(J+1)}{(2J-1)(2J+3)}$$
$$S \ : \ C(J2J+2; 00)^2 = \frac{3(J+1)(J+2)}{2(2J+1)(2J+3)} \ . \qquad (2.37)$$

For the D_2-N_2 and D_2-CO mixtures, the anisotropic contribution was ignored in equation

2.35 as it is very small. For the various pure enhancement spectra of D_2 in D_2-X mixtures, where X=He, Ar, and Kr, the expression for X_{Lm} is simplified to

$$X_{Lm} = P_{J1} C(J_1 L_1 J'_1; 00)^2 < v_1 J_1 | Q_{L_1} | v'_1 J'_1 >^2 < v_2 | \alpha_2 | v'_2 >^2 \ . \tag{2.38}$$

The quadrupole and isotropic polarizability matrix elements for N_2 and CO were set to values of 1.22 and 1.27 a_0^3[3, 26] and 11.8 and 13.23 a_0^3[27, 28], respectively. For He, Ar, Kr, the polarizability matrix elements were set to 1.6, 16.8, and 27.4 a_0^3 respectively[3].

2.5 Spectral Line Shapes

In order to investigate the experimental spectra, the frequency dependence of the absorption coefficient can be modeled by various semi-empirical lineshapes $W(\Delta\nu)$

$$\tilde{\alpha}_{Im}(\nu) = \tilde{A}_{Im} \frac{NW(\Delta\nu)}{1 + \exp(-hc\Delta\nu/kT)} \ . \tag{2.39}$$

Here $\tilde{A}_{Im}$ is the total integrated absorption of the m'th transition of the induction mechanism I, N normalizes the lineshape, $\Delta\nu = \nu - \nu_m + \nu_s$, where ν_m is the wavenumber of a particular transition, and ν_s accounts for any shift (perturbation) in the molecular wavenumbers ν_m. The factor $1 + \exp(-hc\Delta\nu/kT)$ satisfies the detailed balance condition converting the lineshape to an asymmetric function. In order to calculate the total dimensionless absorption coefficient, $\tilde{\alpha}(\nu)$, a summation is performed over all transitions m from all induction mechanisms I

$$\tilde{\alpha}(\nu) = \sum_{Im} \tilde{\alpha}_{Im}(\nu) \ . \tag{2.40}$$

For the overlap induction the line shape function $W_{ov}(\Delta\nu)$ is given by

$$W_{ov}(\Delta\nu) = W^0_{ov}(\Delta\nu) D(\Delta\nu). \tag{2.41}$$

where the intracollisional line shape function $W^0_{ov}(\Delta\nu)$ is written as

$$W^0{}_{ov}(\Delta\nu) = (2\Delta\nu/\delta_d)^2 K_2(2\Delta\nu/\delta_d) \tag{2.42}$$

and the intercollisional line shape function $D(\Delta\nu)$[29] is expressed as

$$D(\Delta\nu) = 1 - \frac{\gamma}{1+(\Delta\nu/\delta_c)^2}. \tag{2.43}$$

The influence of the parameters γ, δ_c and δ_d on these component functions are shown in Figure 2.2.

Many lineshapes have been used to study the quadrupolar absorption. The first was the dispersion-type function

$$W_q(\Delta\nu) = \frac{1}{1+(\Delta\nu/\delta_q)^2}, \tag{2.44}$$

where δ_q is the half-width at half height of the line. Gillard[17] modeled quadrupolar transitions with a modified dispersion lineshape function

$$W_q(\Delta\nu) = \frac{1}{1+(\Delta\nu/\delta_2)^2+(\Delta\nu/\delta_4)^4}, \tag{2.45}$$

where the fourth power term allows better reproduction of the spectrum, specifically adjusting the height of the tails as shown in Figure 2.3 for curves generated at 298 K. As δ_4 gets very large the lineshape trivially reduces to the dispersion lineshape, equation 2.44. See also Reddy et al.[30], and Lewis and Tjon[31] for further details on this lineshape.

Birnbaum and Cohen[12] have proposed a more complicated lineshape function which allowed similar modeling of the tails and which was first used in the analysis of the pure rotational spectra of H_2. The Birnbaum-Cohen (BC) lineshape function can be written as

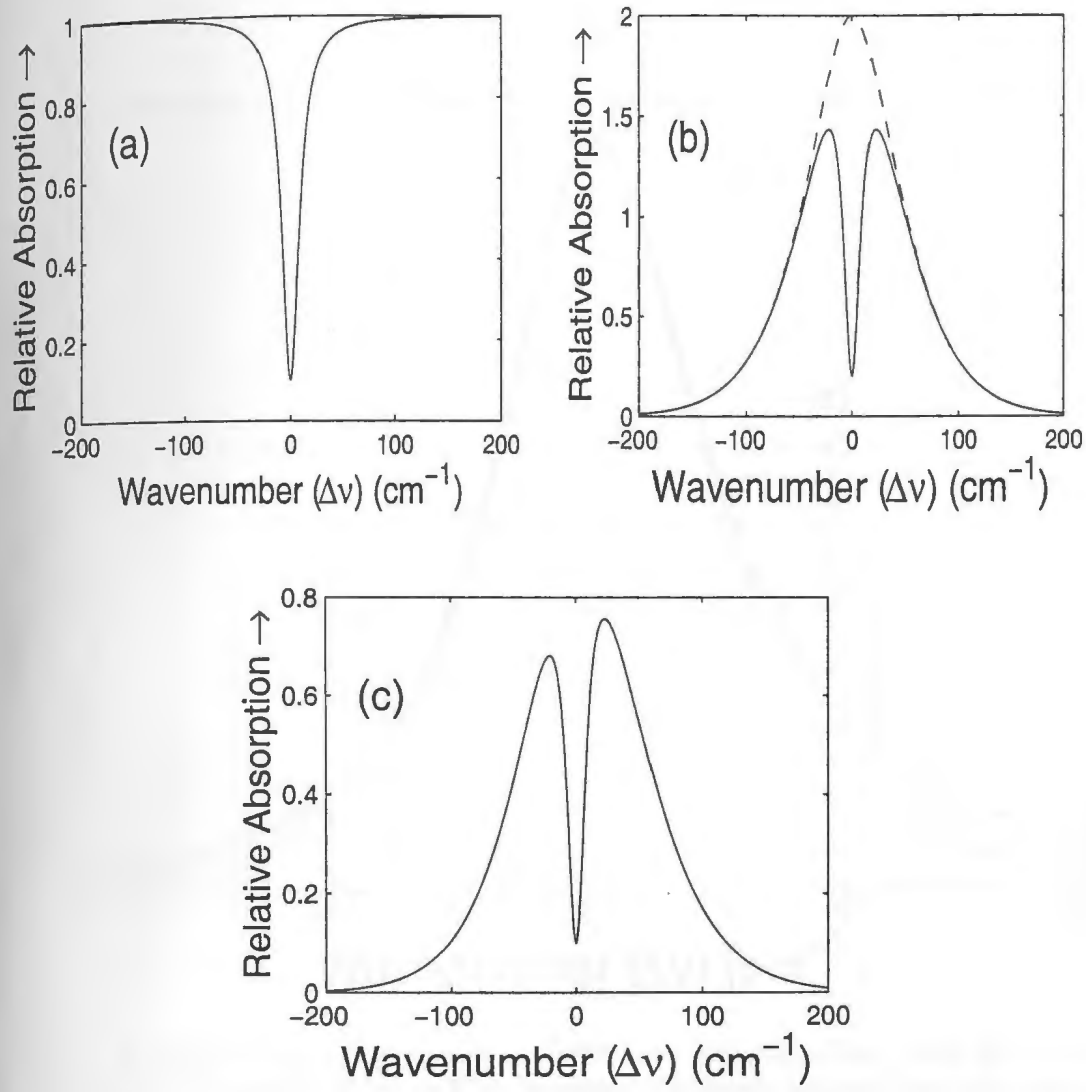

Figure 2.2: Plots of the overlap component functions at 298 K; (a) $D(\Delta\nu)$ with $\gamma = 0.9$ and $\delta_c = 10.0$ cm^{-1}, (b) the dashed line represents W^0_{ov}, the solid line represents the product $W^0_{ov}(\Delta\nu)\ D(\Delta\nu)$ with $\delta_d = 100$ cm^{-1}, and the total overlap lineshape after accounting for detailed balance is given in (c).

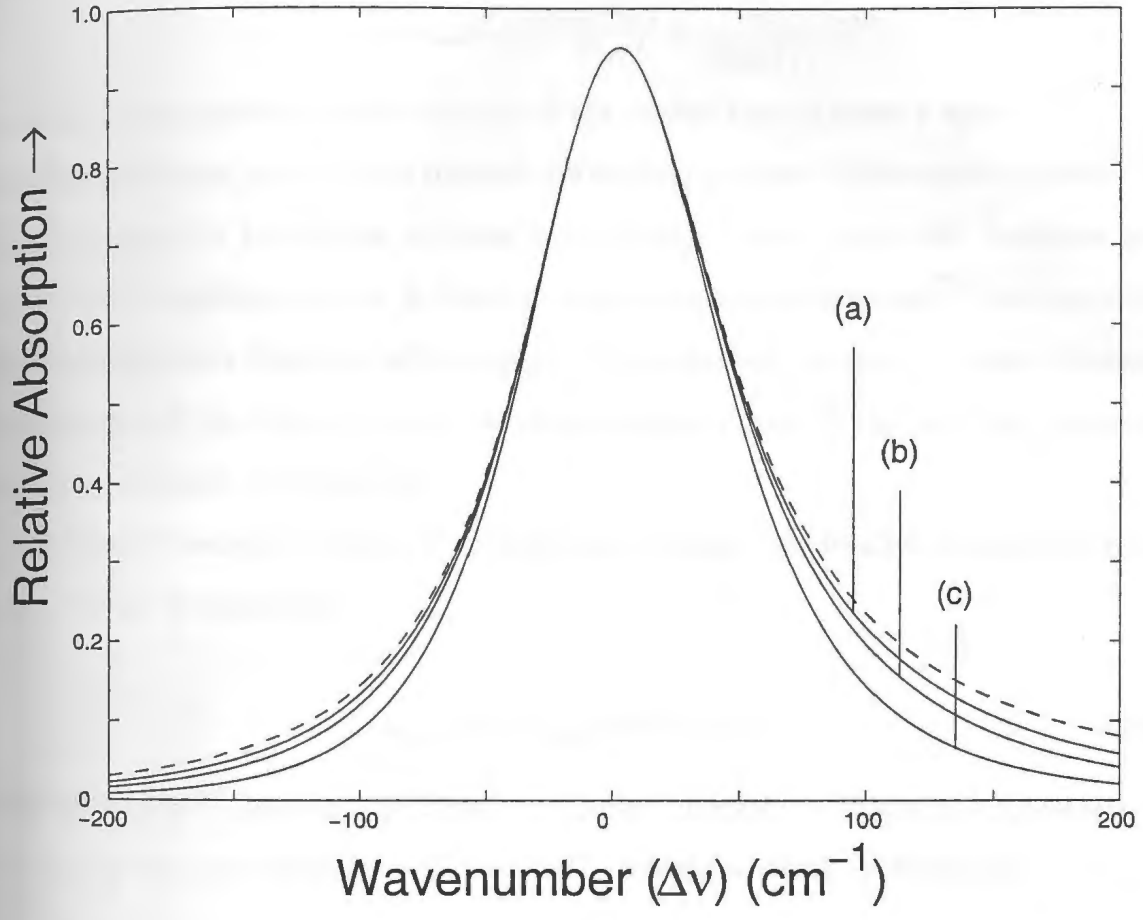

Figure 2.3: In the above plot, the dispersion lineshape (equation 2.44) with $\delta_q = 50$ cm^{-1} is represented by a dashed curve, and the modified dispersion lineshapes (equation 2.45) with $\delta_1 = 50$ cm^{-1} and δ_2= 125, 100, and 75 cm^{-1} are represented in (a), (b) and (c), respectively.

$$W^{BC}(\Delta\nu) = \frac{\tau_1}{\pi}\exp(\frac{\tau_2}{\tau_1})\exp(\frac{hc\Delta\nu}{2kT})\frac{zK_1(z)}{1+(2\pi c\Delta\nu\tau_1)^2}\ , \tag{2.46}$$

where

$$z = [1+(2\pi c\Delta\nu\ \tau_1)^2]^{1/2}[(\frac{\tau_2}{\tau_1})^2 + (\frac{h}{4\pi kT\tau_1})^2]^{1/2}, \tag{2.47}$$

Here $K_1(z)$ is a modified Bessel function of the second kind of order 1 and τ_1 and τ_2 are characteristic times in the dipole moment correlation function. Wavenumber parameters δ_1 and δ_2 can also be used by defining $\delta_i = 1/2\pi c\tau_i$. As δ_2 in the BC lineshape gets large the BC lineshape reduces in behavior to the dispersion lineshape[32], similar to the modified dispersion lineshape with large δ_4. The additional parameter τ_2 also influences the behavior of the wings in much the same way as δ_2 does in the modified dispersion lineshape, as shown in Figure 2.4.

As the BC lineshape function W^{BC} inherently satisfies the detailed balance condition, equation 2.39 is simplified to

$$\tilde{\alpha}_{Lm}(\nu) = \tilde{A}_{Lm}NW^{BC}(\Delta\nu)\ . \tag{2.48}$$

Recently Lewis[33] modified the Birnbaum-Cohen lineshape with the new lineshape referred to as the Lewis-Birnbaum-Cohen (LBC) lineshape which is written as

$$W^{LBC}(\Delta\omega) = \frac{2}{1+e^{-\beta\hbar\Delta\omega}}\frac{e^{\tau_2/\tau_1}}{\pi}\frac{\tau_2}{\sqrt{1+\Delta\omega^2{\tau_1}^2}}K_1(\frac{\tau_2}{\tau_1}\sqrt{1+\Delta\omega^2{\tau_1}^2}). \tag{2.49}$$

Here K_1 is the same as defined in equation 2.46, and $\Delta\omega = \omega - \omega_m + \omega_s$ where ω_m is the frequency of the m'th transition ($\omega = c/\nu$). The LBC lineshape function is derived from a slight modification of the procedure used in developing the Birnbaum-Cohen (BC) lineshape function[12]. The same time correlation function is used in both; however, the

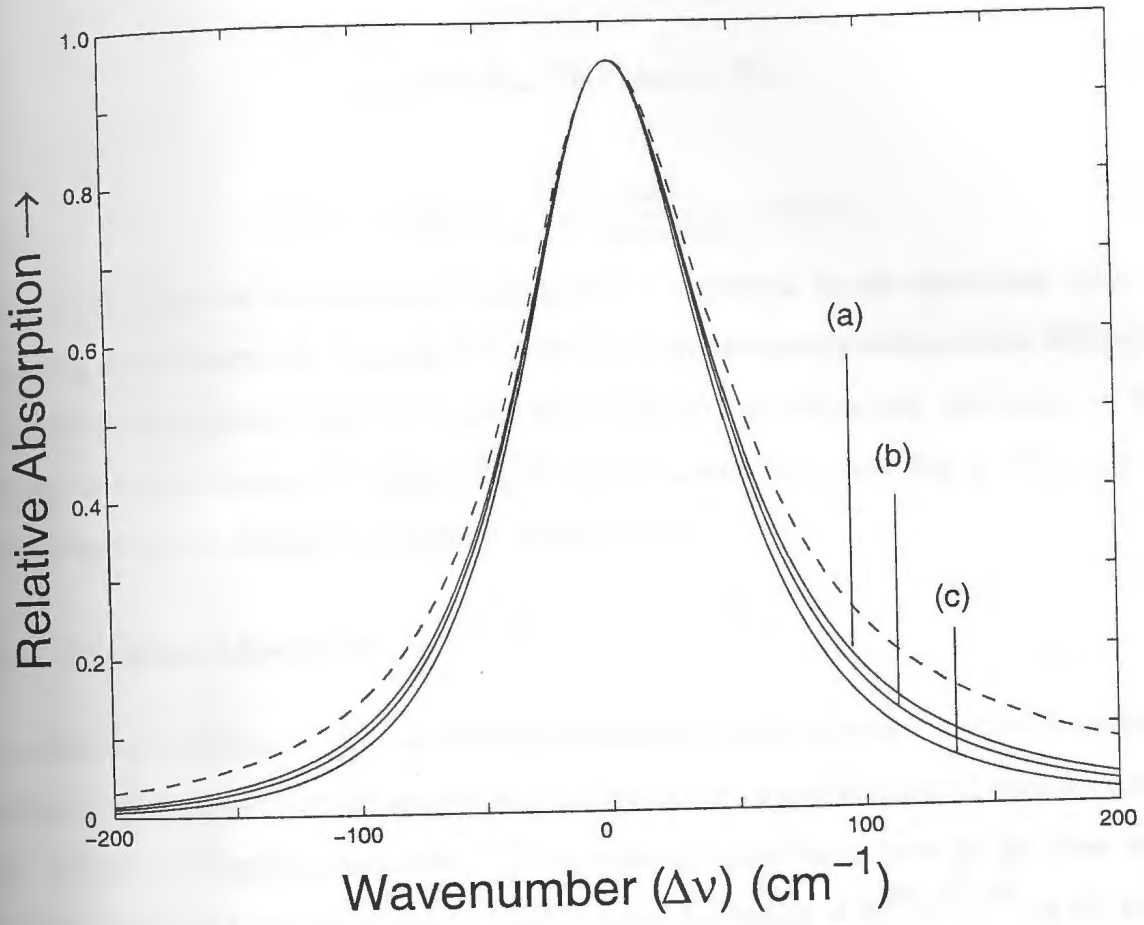

Figure 2.4: In the above plot, the dispersion lineshape with $\delta_q = 50$ cm^{-1} is represented by a dashed curve, and the BC lineshape (equation 2.46) with $\delta_1 = 50$ cm^{-1} and δ_2=125, 100, and 75 cm^{-1} are represented in (a), (b) and (c), respectively.

LBC lineshape uses Boltzmann asymmetrization to satisfy detailed balance and the BC lineshape uses Egelstaff time[34].

For the present experiments it was necessary to slightly modify equation 2.48 and 2.39 as follows

$$\tilde{\alpha}_{Lm}(\nu) = \tilde{A}_{Lm} SNW(\Delta\nu) + B/\nu, \tag{2.50}$$

$$\tilde{\alpha}_{Im}(\nu) = \tilde{A}_{Im} \frac{SNW(\Delta\nu)}{1 + \exp(-hc\Delta\nu/kT)} + B/\nu \ . \tag{2.51}$$

where S accounts for any necessary multiplicative correction to the theoretical value of the integrated absorption $\tilde{A}_{Lm}$ and B accounts for any frequency-independent difference between the background spectrum and binary gas mixture absorption spectrum. In the fitting, the total integrated absorption factors $\tilde{A}_{Lm}$ and $\tilde{A}_{Im}$ were set to their binary approximations as defined in equations 2.33 and 2.31.

2.6 Quantum Lineshapes

In addition to the semi-empirical lineshapes discussed in the previous section there exist quantum lineshapes[35] which are derived from purely quantum mechanical considerations and contain no floating parameters. These quantum lineshapes have so far been used mainly on the CIA spectra of the 1-0 and 2-0 and 3-0 bands of H_2[36, 37, 38] in the pure gas and the 1-0 band of H_2 in H_2-He[39] mixtures, and the 1-0 band of N_2[40].

2.7 Irreducible three-body interactions

Most of the theoretical work on the absorption coefficients has focused on binary interactions, however there has also been experimental evidence of triple transitions arising from collisions of H_2-H_2-H_2 in the second overtone band of molecular hydrogen observed

in our laboratory[41] and the theoretical calculations [42] which show general agreement with the observed spectra.

Chapter 3

Apparatus and experimental Details

The experimental set up consisted mainly of a 2 m high-pressure, low-temperature, stainless-steel absorption cell, a gas handling system, an infrared spectrometer and a microprocessor-controlled data acquisition system. Details of the apparatus and the experimental techniques are presented in this chapter.

3.1 The 2 m Absorption Cell

The 2 m long, transmission-type absorption cell, designed and constructed earlier in our laboratory[17] for work with gases at high pressures up to 2000 atmospheres and temperatures in the range 77 to 298 K, was used in the present work. A schematic diagram of the cross section of one end of the cell is shown in Figure 3.1. The absorption cell T was constructed from type 303 stainless-steel tubing, 2 m long, 7.62 cm in outer diameter and 2.54 cm in inner diameter with a wall thickness of 2.54 cm. The polished light guide L was made in five sections and has a rectangular aperture, 1.00 cm high by 0.50 cm wide. A sapphire window W_1, 2.54 cm in diameter and 1.00 cm thick, was attached to the polished stainless steel window seat S having a circular aperture of 1.00 cm with General Electric Silicone Sealant. With invar O-ring R_1 between the window seat and the absorption cell, a pressure-tight seal was secured by tightening a stainless steel piece P against the cell body using eight Allen head bolts. A stainless steel capillary tube with a outer diameter of 0.64 cm was connected to the cell body with an Aminco fitting M to act as the gas inlet I.

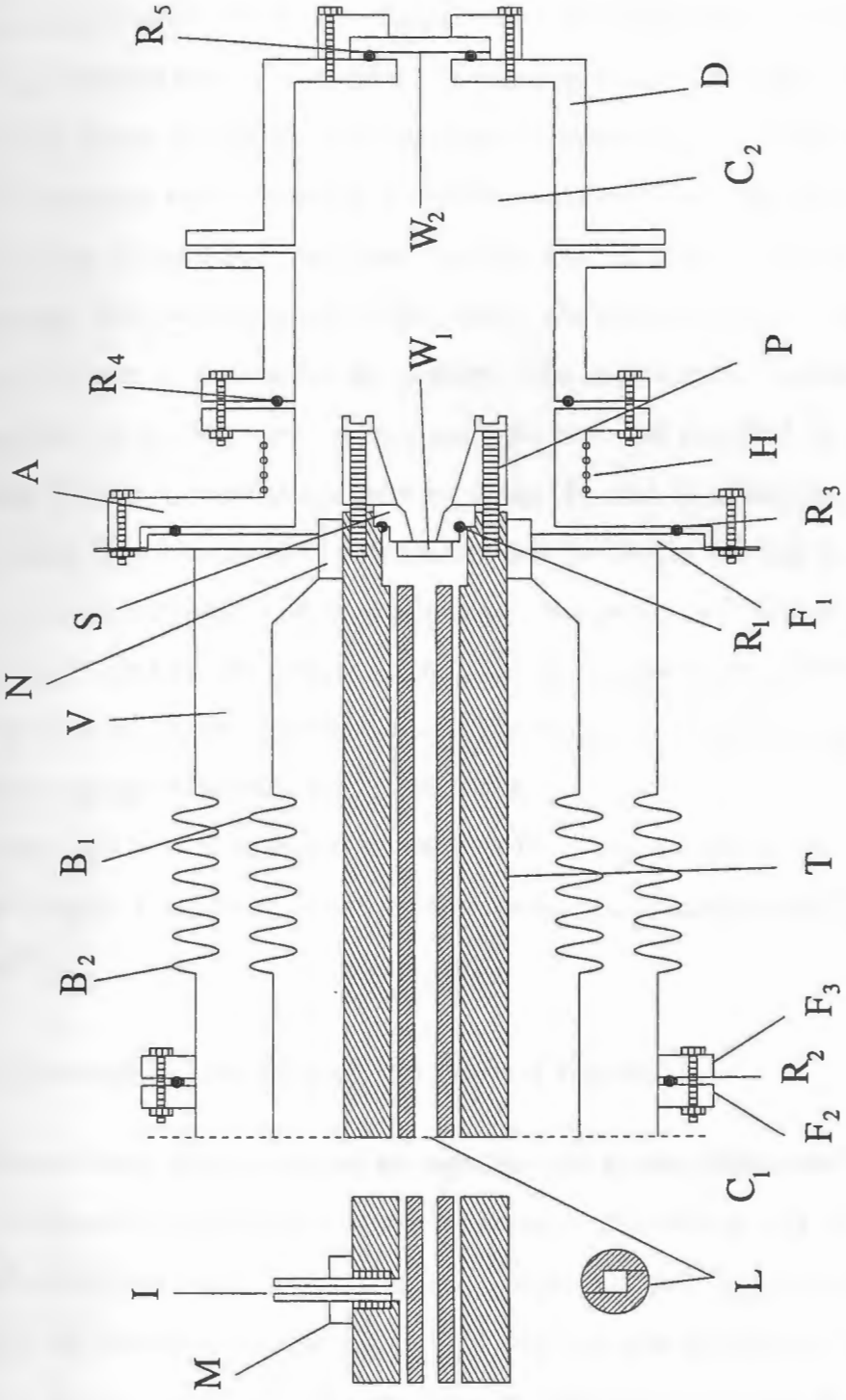

Figure 3.1: A schematic diagram of one end of the 2 m absorption cell (See text for details of the symbols).

A stainless-steel nut N, 1.50 cm long and 7.62 cm in inner diameter, was threaded onto the end of the cell and welded on to it. A flange F_1 and bellows B_1 (10.16 cm in diameter), both made from stainless steel, were welded to a stainless-steel cone. Bellows B_2 (16.5 cm in diameter) and flanges F_2 and F_3 were also made of stainless steel. These two bellows allow relative expansion and contraction of the absorption cell and the vacuum jacket V. A neoprene O-ring R_2 maintained between the tightened flanges F_2 and F_3 provided a good vacuum seal. For low temperature experiments, chamber C_1 is filled with a coolant such as liquid nitrogen or alcohol-dry ice mixture. The end vacuum chamber C_2 is 10.0 cm long and 10.5 cm in diameter. A vacuum-tight seal was provided by means of a silicone rubber O-ring R_3, maintained between flange F_1 and an aluminum cap A, and a neoprene O-ring R_4 between the aluminum cap and the Delrin end cap D. A sapphire window W_2, 0.30 cm thick and 5.08 cm in diameter, was sealed to D with a neoprene O-ring R_5 between W_2 and D. The purpose of the vacuum chamber C_2 is to prevent frosting on the cell window W_1 in the low temperature experiments. Freezing is prevented by means of a heating tape H wound around the cap A.

For the work on the CIA fundamental band of D_2 in D_2-N_2 and D_2-CO mixtures as described in Chapter 5 a transmission-type absorption cell of sample path length 105.2 cm was used[43].

3.2 The Experimental Setup and the Optical Layout

The experimental setup and the optical arrangement are shown schematically in Figure 3.2 : here L is the source of radiation, M_1 and M_2 are spherical mirrors, A is the absorption cell, M is a Perkin-Elmer model 99 prism monochromator, P_1 and P_2 are Plexiglas boxes. S_1 and S_2 are the entrance and exit slits, M_3 is a 21^o off-axis parabolic mirror, P is a prism, M_4 is a littrow mirror, M_5 - M_8 are plane mirrors (M_8 has a hole in the center),

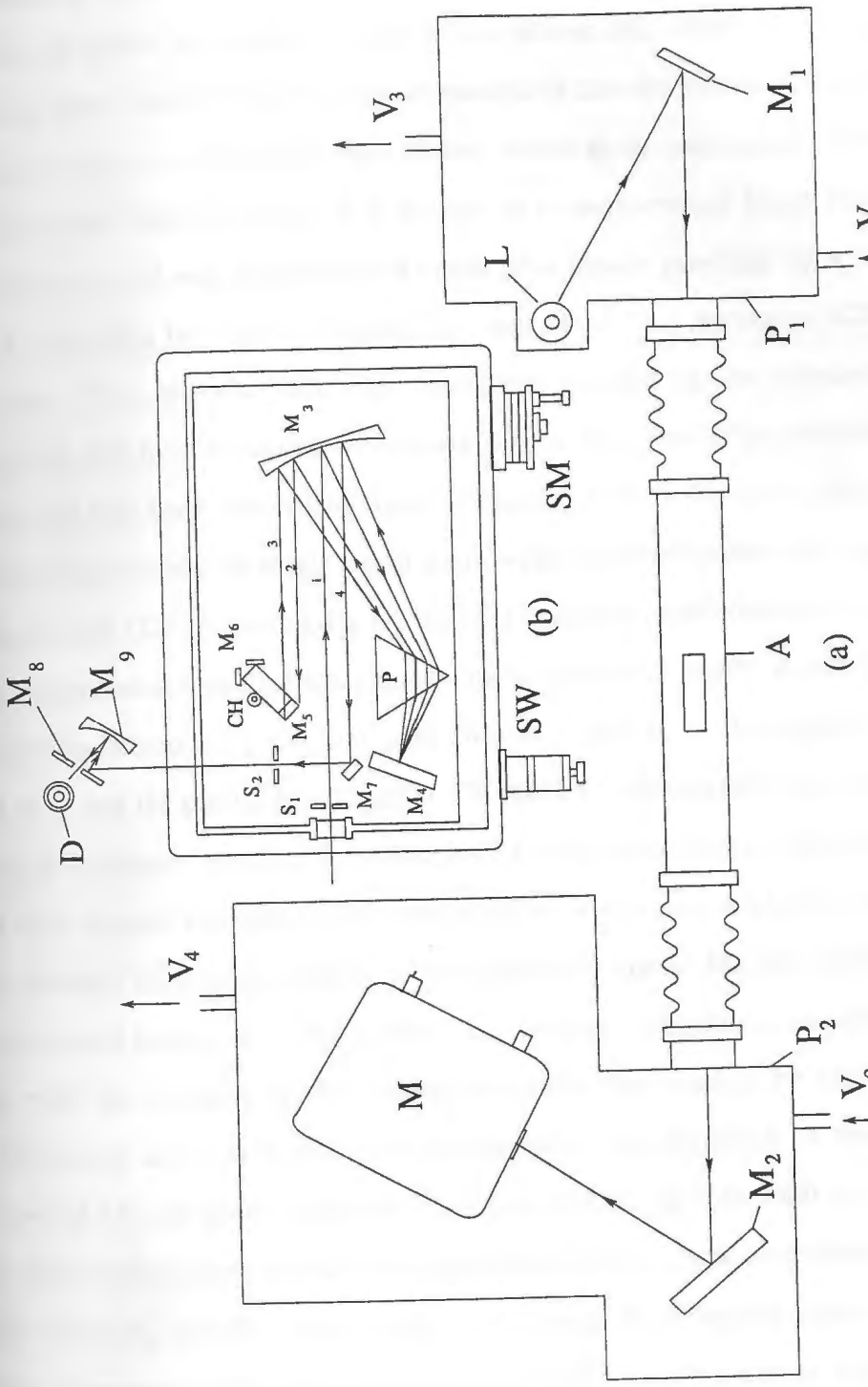

Figure 3.2: (a) A schematic diagram of the experimental setup. b) Path of monochromatic radiation inside the monochromator is shown for simplicity. See text for details of the symbols

M_9 is a parabolic mirror, CH is the tuning fork chopper, D is a cooled PbS detector, SM connects to the screw for manual control of the Mirror M_4, which is also connected to the stepping motor, and SW is the manual control of the slit widths S_1 and S_2.

The light source is a silicon carbide globar which gives continuous radiation in the near infrared and visible regions. It is housed in a water-cooled brass jacket designed in our laboratory and was operated at 9 amps from power provided by a Variac model WJOMT3A supplied by General Radio USA, stabilized by a Sorensen ACR 2000 voltage regulator. The radiation from the source was focused on the entrance window of the absorption cell by a front-coated concave mirror M_1. Radiation transmitted by the absorption cell was then focused by another concave mirror M_2 on to the entrance slit of a Perkin-Elmer model 99 single-beam double-pass monochromator M, equipped with a lithium fluoride (LiF) prism and a cooled lead sulphide (PbS) detector D. The optical path of monochromatic radiation inside the monochromator is also shown in Figure 3.2. The focused radiation after the first pass (beams 1 and 2) in the monochromator was chopped by a 260 Hz tuning-fork chopper CH, model L-40, supplied by American Time Products, and reflected back to the prism for a second pass (beams 3 and 4). The radiation was then focused through the exit slit of the monochromator where it passed outside and was reflected off a plane mirror, on to a parabolic mirror M_9 then back through the plane mirror and finally on to the cooled PbS detector. The linear response of the PbS detector with the intensity of the incident radiation was checked by earlier researchers in our laboratory and was found to be satisfactory. The slit width of the spectrometer maintained at 150 μm gave a spectral resolution of 4.43 cm^{-1} at 3000 cm^{-1}.

The entire optical path outside the absorption cell was contained within two airtight Plexiglas boxes P_1 and P_2 (Figure 3.2). Both boxes were flushed continuously during the entire experiment with dry nitrogen gas produced by evaporating liquid nitrogen in a 200 litre container with a small electrical heater (a 100 Ω 25 W resistor). The inlet

(V_1 and V_2) and outlet (V_3 and V_4) of the Plexiglas boxes are one-way plastic valves which prevent outside air from entering the boxes. It took about 4 to 5 days to reduce atmospheric water vapor absorption to a stable reduced level.

3.3 The Data Acquisition System

A block diagram of the modified signal detection and recording system is shown in Figure 3.3. The signal from the PbS detector was sent to a lock-in amplifier, model SR510, with a built-in preamplifier, supplied by Stanford Research Systems. The signal from the lock-in amplifier was then sent to the decade divider, model DV412, supplied by Electro-Measurement Inc., for attenuation. The attenuated signal was then sent to a microprocessor-controlled analog-to-digital converter (ADC) which in turn transmitted the data to a computer for storage. This computer was a 486DX operating under windows 95 running the QBASIC data collection program[17, 44]. This setup is a significant modification to that which was described previously[44] with the addition of an additional computer, a Pentium 100.

The previous setup[44] had two main limitations and drawbacks. First, it was not possible to run even simple checks on the quality or stability of the data during collection because calling another program under the Windows operating system, would cause a short break in the execution of the QBASIC program which controlled the data acquisition as the computer allocated the necessary resources. As the QBASIC program is responsible for controlling the rotation of the screw, a short and sudden stop in the incremental advances could cause the screw to skip and introduce a systematic error into the data. Second, at times it is necessary to run data collection for an extended period of time, often hours or even days. These long runs are necessary mainly for mixing, or simply to gather data at night when the load on the lines is small and thus the signal

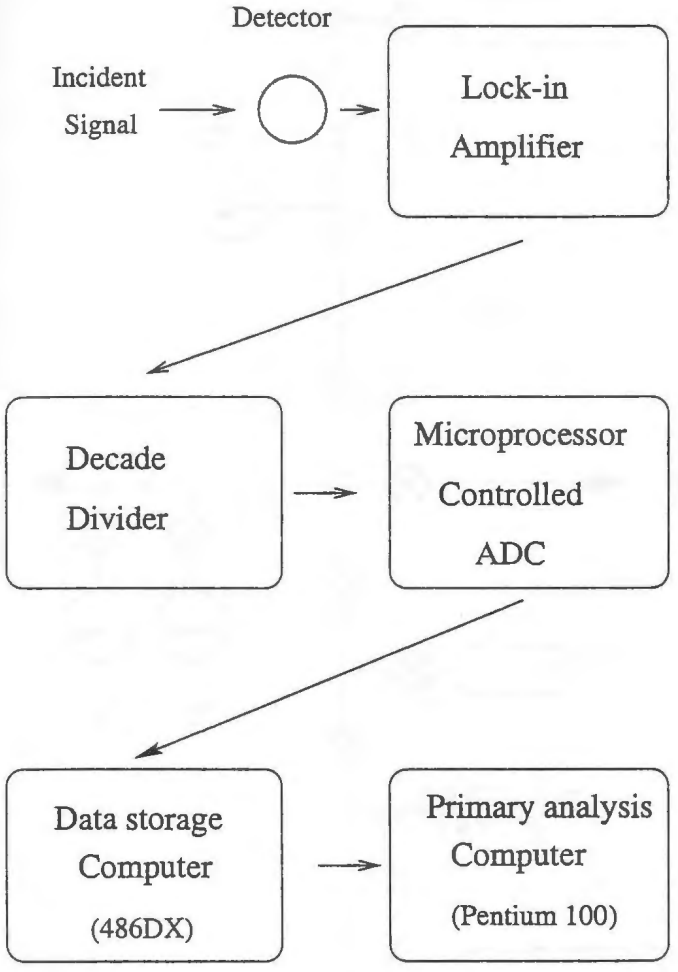

Figure 3.3: A block diagram of the signal detection system.

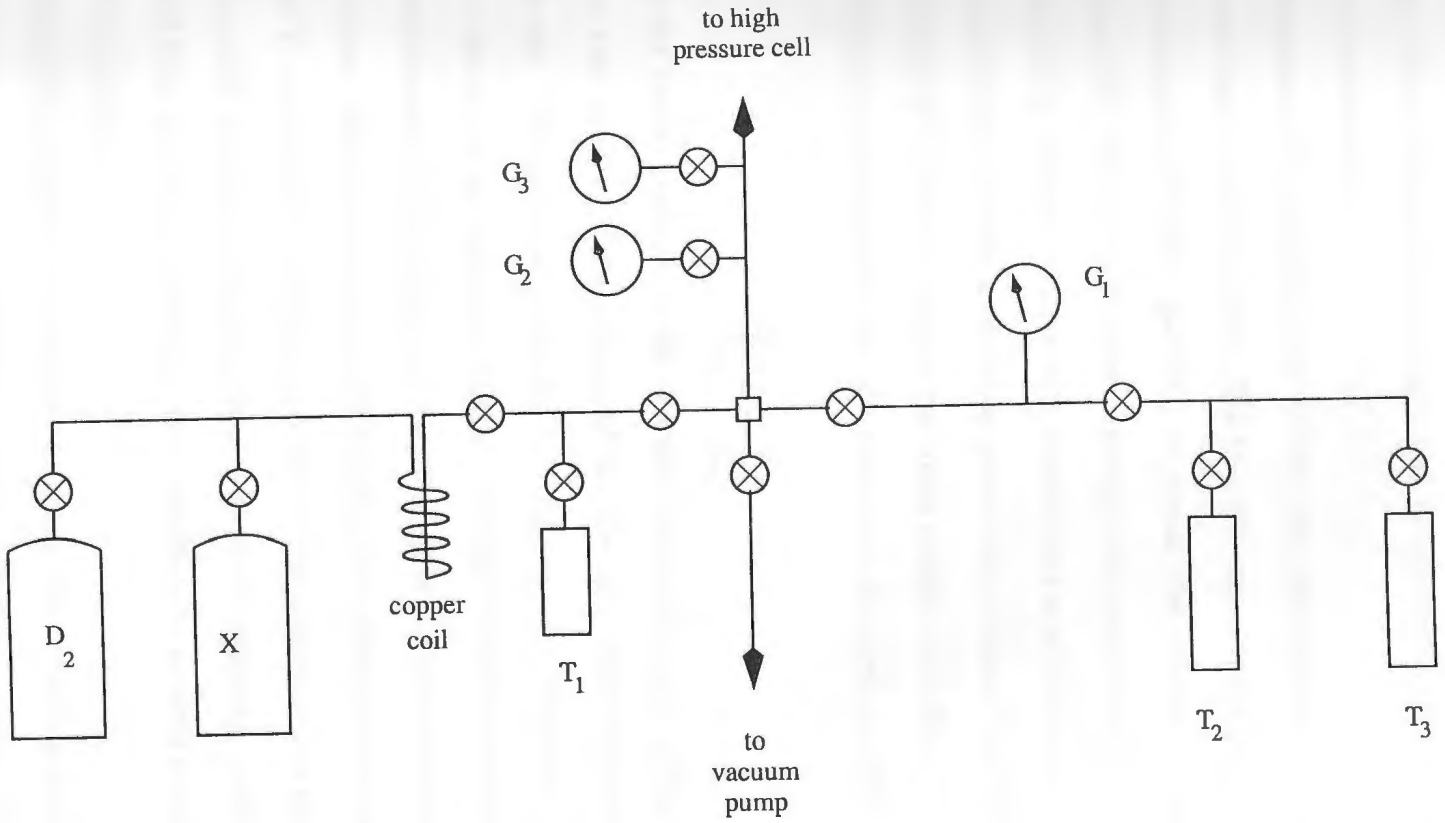

Figure 3.4: The high-pressure gas handling system. T_1, T_2 and T_3: thermal compressors; G_1, G_2, and G_3: Ashcroft-type Bourdon tube gauges : X is the perturbing gas.

the gas cylinders, were Aminco stainless steel high-pressure fittings, rated for pressures up to 60,000 psi. Ultra high-purity gases supplied by Matheson Gas Products, Canada were used in the experiments.

Thermal compressor T_1 (pressure limit $\approx$ 7500 psi) and T_2 and T_3 (pressure limits $\approx$ 25000 psi) were made of stainless steel. The low volume, medium pressure compressor T_1 was used to compress the base gas (D_2) to obtain the necessary pressures for the required densities after the gas had passed through the copper coil which was cooled with liquid nitrogen in order to remove any impurities via solidification. The required higher pressures necessary for the perturbing gases were obtained by means of T_2 and T_3. As the volumes of T_2 and T_3 are several times greater than the volume of the cell they allow efficient pressurization of the cell. Assuming the ideal gas law,

$$\frac{\Delta P_{cell}}{\Delta P_{tc}} = \frac{V_{tc}}{V_{cell}} , \tag{3.1}$$

where ΔP_{tc} is the loss in pressure of the thermal compressor, and ΔP_{cell} is the gain in pressure of the cell, and V_{tc} is the volume of the thermal compressors and V_{cell} is the volume of the cell. The required pressures for krypton were obtained by transferring the complete contents of the krypton cylinder into the cooled thermal compressor T_2 producing approximately 2500 psi, used as required in the binary mixtures. For helium, argon and krypton, thermal compressors T_2 and T_3 were filled with the gas at cylinder pressure, then T_2 was cooled with liquid nitrogen, which drew in the gas from T_3. T_3 was filled again with the gas at cylinder pressure while T_2 remained cooled. The gas was then transfered from T_3 to T_2, refilling T_3 and repeating the process as required to build up the necessary pressure.

A photograph of a quarter inch stainless steel net (SC), covering the absorption cell (C), is shown in Figure 3.4. This was an enhancement of the existing system added to

protect those in the laboratory in case of a pressure overload of the thermal compressors, a very unlikely but possible scenario. The cage was designed to contain any materials which would be propelled by the pressurized gas to the enclosed area. The quarter inch net was welded onto square steel tubing which was then reinforced by quarter inch flat bar stock which was bolted over the net through the tubing with quarter inch thick bolts. The square tubing was welded into quarter inch flat stock which was bolted to the floor. Also shown in the same picture are several pressure gauges (G), a 200 litre liquid nitrogen container (D), and plexiglas boxes P_1 and P_2.

3.5 Gauge calibration

The standard Ashcroft-type Bourdon tube gauges were calibrated via a two step process. First the gauges were calibrated against a test gauge. Gas was introduced into a system containing both gauges and once the pressure was stabilized, the readings of both gauges were recorded. This set of data was used to determine a polynomial fit, represented by

$$P_t = \sum_i^O a_i P_s^i, \tag{3.2}$$

where a_i are the expansion coefficients determined by a regression, P_s the pressure of the standard gauge, P_t is the pressure of the test gauge, and O is the order of the polynomial. The order was chosen using the F statistic to judge the significance of an extra order [45, 46, 44]. The specific criterion used to reject a higher order was that the the extra term had greater than 5 percent probability of simple random correlation, this criterion was used in all such order determinations. The test gauges were calibrated against an Ashcroft dead-weight pressure balance which has an accuracy of 0.1%. This again produced another set of data, and another polynomial similar to equation 3.2 was used :

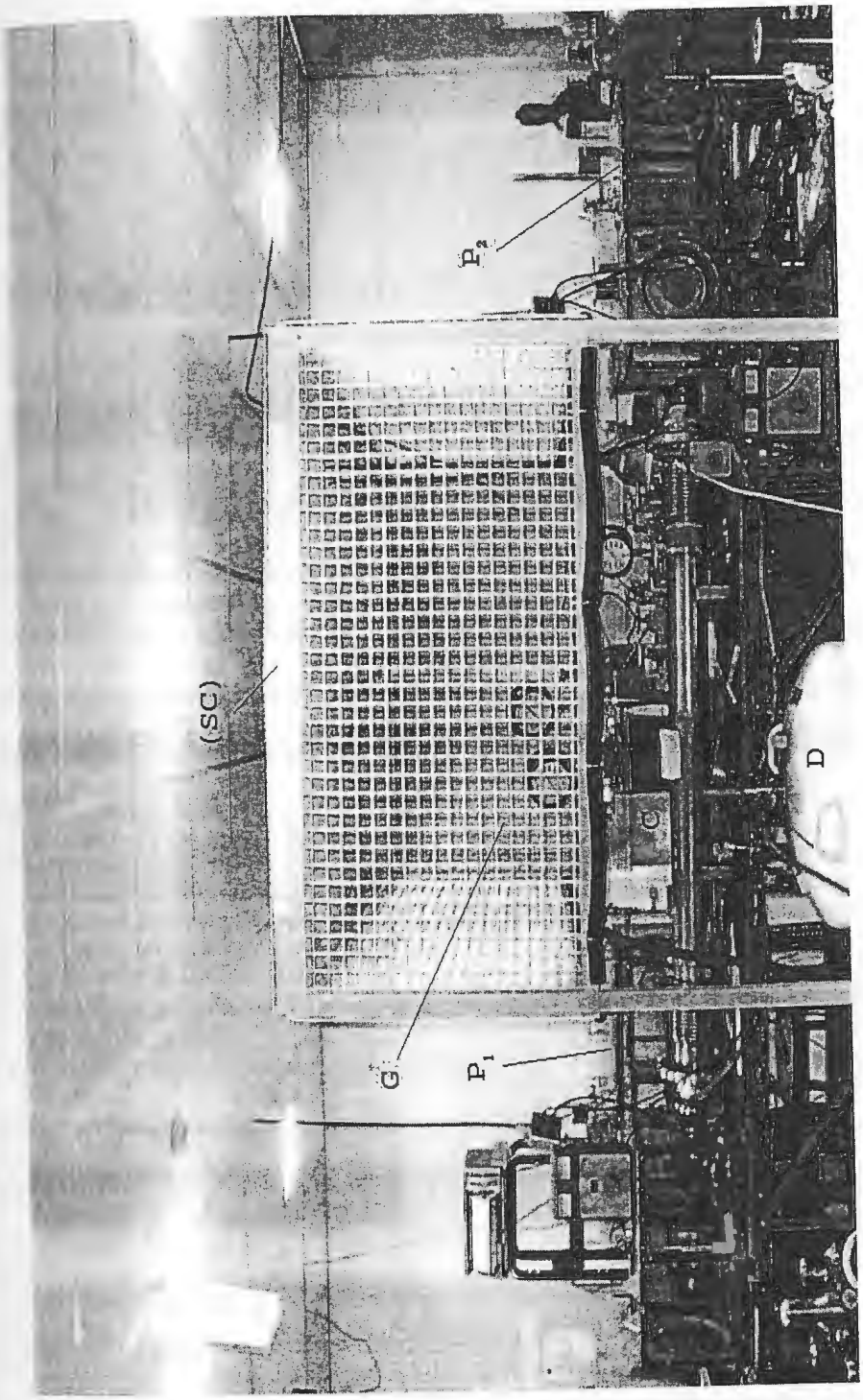

Figure 3.5: The experimental setup (See text for details of the symbols).

$$P_{dw} = \sum_{i}^{O} a_i P_t^i, \tag{3.3}$$

where P_{dw} is the pressure given by the dead weight tester. These polynomials (equations 3.2 and 3.3) were used in succession to determine the absolute pressure P_{dw} from the recorded pressure on the standard gauge (P_s).

During the course of this work the existing calibration programs were enhanced to allow a more robust prediction of the uncertainty of the pressures calculated from the calibration which would give a more reliable estimate of the uncertainly of the densities deduced from them which is critical to calculation of robust absorption coefficients. Upon inspection of the results of the fitting of the pressures to the expansions given in equations 3.2 and 3.3, in particular after examining the correlation matrix, it was found that the correlation between the expansion coefficients was high, and thus in order to determine the error produced it was necessary to use not only the uncertainties in the expansion coefficients themselves but also the correlation coefficients [47]. The resultant uncertainty in the pressure $U(p)$ is given by

$$U(p) = \sqrt{PD^t \; CM \; PD}\;, \tag{3.4}$$

where PD is the column matrix $U(a_i)$ $(\frac{\partial F}{\partial a_i})$. Here $U(a_i)$ are the uncertainties in the expansion coefficients a_i, F is the polynomial, and CM is the correlation matrix. In this case the correlation coefficients generally tend to reduce the overall uncertainty. The calibration programs were also modified to include the effect of the uncertainty in the input pressures P_s and P_t, which came from the limitations of reading the analog gauges. These experimental errors were set to one fifth of a division of the calibrating analog markings and were due mainly to parallax variance, were propagated through the calculations by normal means and also add an uncertainty to the final result.

3.6 Isothermal Data

The density of a gas for the recorded pressure was calculated from its isothermal PVT data. A least-squares fit was used to determine the coefficients in the polynomial relationship

$$\rho = \sum_{i}^{O} a_i P^i, \tag{3.5}$$

where a_i are the regression determined expansion coefficients, P is the pressure in atm and ρ is the density in amagat.

To calculate the partial densities in a mixture, first the fixed base density ρ_a was was directly obtained from its known base pressure using equation 3.5. The partial density ρ_b of the secondary gas was then calculated using the approximation [48]:

$$\rho_b = [1/(1+\beta')][(\rho_a)_P + \beta'(\rho_b)_P] - \rho_a \ , \tag{3.6}$$

where $(\rho_a)_P$ and $(\rho_b)_P$ are the densities of gas a and b respectively at the total pressure P of the mixture, $\beta' = \rho_b'/\rho_a$, where ρ_b' is the approximate partial density of gas b corresponding to the partial pressure $P_b = P - P_a$, P_a being the base pressure of gas a in the mixture which is measured directly. It is noted that $\rho_a + \rho_b$ represents the total density of the mixture.

Since equation 3.6 is nonlinear it lends itself to an iterative solution, where convergence was defined as the point at which the difference between successive values of ρ_b was smaller than 10^{-4} %. This limit is set much larger than the machine precision limit of 10^{-13} % for double precision reals, which were used for all numerical calculations, as all such densities calculated have uncertainties of ≈ 1 % anyway due to uncertainties in measuring the corresponding pressures.

The above algorithm had been previously implemented in a FORTRAN program[44] and was enhanced during this work through the addition of code which performed error propagation on the uncertainties of the input pressures described in the previous section through all stages of the above calculations. In addition the slight temperature variation of the system due to changes in room temperature was taken into account using an interpolation of the relevant expansion coefficients[49] in equation 3.5 to calculate the magnitude of its influence.

3.7 Reduction of Experimental Data

The experimental data is first collected as a two column file consisting of a drum number, which is an incremental step of the screw which determines the frequency of light collected, and the corresponding intensity at that drum number. Supplementary data is added to this file which includes the time, a predefined user description of the region and mixture composition. A measure of the trace quality was also added to the file and was determined by sampling at the start and end of the spectral region with the shutter closed. This measurement of the line noise was used to weight the quality of the trace so as to allow greater precision through averaging. The spectral region was scanned for multiple passes at each specific mixture density composition and at least five consecutive traces were found to be consistent before the the mixing was consider to be complete.

Before the data can be "reduced", which is to say, the desired absorption coefficients calculated from the recorded intensities using equation 2.17, it is necessary to "normalize"[17] and then average the data sets to reduce the random errors and systematic variances. The normalizing process takes into account several systematic factors. First, there can be a systematic drift S in the drum number n due to the stepping motor not being in the same starting position for each run. This occurs mainly due to

random loads on the power line which may cause an extra step. This would not be a major problem by itself as it could be eliminated by aligning the spectra using known constant features of the spectra, such as the positions of the water vapor peaks. However, the problem is compounded by a couple of other systematic factors which may also be simultaneously present in the trace.

Apart from the drift S, the intensity can also be affected by a multiplicative factor M and/or an additive factor A. The effect of each of these factors is very small and is of the order of less than one percent. These factors can often be ignored; however, in the present case, there is a low signal to noise ratio in the low wavenumber wing and thus it is critical to minimize these random variations to maximize the quality of the spectra. The signal to noise ratio is low in that spectral region because of limitations of the light source and the detector. These small factors do not have a large effect on the calculated absorption coefficients, but are critical in the profile analysis. Previously, the algorithm implemented to perform the required calculations necessary for the reduction was a segmented one, which dealt with the aforementioned factors individually and was in part not rigorously quantified statistically as it depended on human judgment in certain cases rather than a statistically- defined selection criteria[44].

During the course of collecting the data for this work, it was desired to minimize the human influence in the reduction of the data to allow for a more robust data set to be determined. This was achieved by combining the various FORTRAN computer programs into one cohesive package by defining the problem in terms of a quantity which represented the quality of the optimal trace. This then allowed the determination of the three variables S, M, and A by a least squares regression. The quantity which was minimized during the regression is the expected residuals $R(n)$ between two traces which is readily defined as :

$$R(n) = I_i(n) - M\ I_j(n+S) + A\ . \tag{3.7}$$

Here I_j and I_i are the intensity of two traces i and j, The wavenumber-independent regression constants S, M and A are simultaneously obtained by a nonlinear least squares fit using the Levenberg-Marquardt algorithm[50]. The complete process took one reference trace I_i and deduced the three constants for all other traces I_j to minimize those systematic errors. As a further enhancement to the existing algorithms, the median trace was then taken to best represent the spectral absorption instead of the mean as was used previously as the median is a more robust estimator, especially when dealing with outlier contamination.

The program which implemented the above calculations also performed many secondary calculations and provided additional output such as the mean deviations between the reference trace and all other traces individually which was used for checking the stability of the traces and the overall quality. Additional refinements were also made to the program such as it could either use the entire spectral region for comparison or a number of restricted subsets. Care must be taken in the defined subsets as in order for the algorithm to determine a set of accurate constants the regions specified for comparison must include data with three distinct behaviors : the spectral region I with distinct peaks allows accurate determination of the shift factor S; the spectral region II of low intensity allows accurate determination of the additive constant A; and the spectral region III of high intensity allows accurate determination of the multiplicative constant M in equation 3.7. The intensity in regions II and III should be close to uniform to minimize the correlation from A and M to S. In the current spectra, the low wavenumber wing is of uniform low intensity so it was chosen to be region I and the high wavenumber wing contains a uniform high intensity section with distinct water vapor peaks so it was chosen

to be regions II and III.

As noted in the above the goal of the procedure is to reduce human subjective bias as ideally the data reduction should give the same results regardless of the operator who performs the calculations, from this perspective the influence of the selection of the reference trace $I_i(n)$ is equation 3.7 was examined with use of Monte Carlo methods[51, 52, 46]. Specifically a wrapper was added to the regression program used on equation 3.7 which took each trace in succession and calculated the median trace after the systematic factors were removed and thus a set of medians were produced. This consistency check was performed on several sets of data periodically throughout the analysis and found to not cause a significant difference. The final implementation of the above algorithm simply picked a trace at random using a built in random number generator for a reference. As a precaution, the traces were initially plotted and compared visually to ensure the elimination of a large systematic distortion such as a power fluctuation.

On a final note, the "averaging" described in the above could be performed with a direct minimization on the set of traces producing one data set which has the minimal residual when compared against the other traces when taking into account the systematic errors S,M, and A. This is a more robust method, but the previously described algorithm was a natural extension of the existing procedures[17, 44] and it has the added benefit of producing the normalized traces individually which can be viewed by the operator performing the data reduction as yet another consistency check.

3.8 Calibration of the Spectral Region

As noted in the previous section the spectral intensities were recorded as a function of the drum number of the spectrometer. The drum number is a counter, incremented uniformly during the rotation of the stepping motor which turns the littrow mirror M_4 in

some simple Monte Carlo methods were used in the present work as a natural extension of the existing linear regression routines[17, 50, 44]. A wrapper was written for the FORTRAN regression program which took the set of wavenumbers ν, drum numbers n, and associated uncertainties and created a user defined number of data sets distributing the values of n and ν about their uncertainties assuming a normal deviation. These synthetic data sets were then fitted and the results compiled and analyzed. Due to a high correlation between n and ν the reversed uncertainty ratio did not actually make a large influence on the calibration, but the same technique was used to more significance during the calculation of the absorption coefficients (see Section 2.3).

One final comment on the calibration is that since the drum numbers are not determined absolutely, the absorption spectra need to be aligned with the calibration spectra before the results of the regression on equation 3.8 can be applied. As the CIA and standard spectra are very dissimilar, the method used in the previous section to quantify the shift factor S can not be used. Traditionally, any shift in drum number was taken into account by graphically aligning the spectra to a standard mercury line or water vapor peak[57]. Here the existing calibration program[17] was enhanced by directly minimizing any systematic shift using a weighted average[46] of the difference in positions of a user defined number of reference peaks (usually five sharp water vapor peaks were chosen) in both the absorption and calibration spectra. The mean shift S which was determined from the weighted average, given by

$$S = \frac{\sum_1^N w_i x_i}{\sum_1^N w_i}, \tag{3.9}$$

where N is the number of data (in the present case N is equal to 5), x_i is the difference in peak positions of the i'th water vapor peak in the calibration and absorption spectra, and w_i is the weight which is the inverse of the variance of the difference in peak positions.

The variance in the peak position difference is just the sum of the variance in the peak positions, which is the square of the uncertainty in determining the position of the central maximum of a given peak, usually 1-5 drum numbers. The error δ_S in the shift was also calculated by the standard formula

$$\delta_S^2 = \left(\frac{\sum_1^N w_i x_i^2}{\sum_1^N w_i} - S^2\right)\frac{N}{N-1}. \tag{3.10}$$

The uncertainty δ_S was propagated through the calibration by adding the difference in the calibrated trace shifted by S and by $S + \delta_S$ to the existing uncertainty in intensity.

3.9 General remarks on data handling

As the existing algorithms for the collection, reduction and calibration of the data were modified, there were two general goals always in mind for the enhancements. The first was that all measured data have corresponding estimates of quality. These uncertainties were used in all calculations of quantities from said data and by error propagation allowed the determination of uncertainties of the resultants. When the calculations are simple the error propagation is achieved by the required differentials using equation 3.4; however, in some more involved calculations such as those involving iterative algorithms, the influence of uncertainty is determined by a Monte Carlo simulation, repeating the calculation with normally distributed perturbed values.

The second goal of the refinements was to reduce operator bias. This was achieved by examining how human judgment was performed and by defining a corresponding mathematical criterion in its place, such as the use of the F statistic to judge the quality of additional terms in regression analysis. When it was not possible to eliminate this judgment, steps are taken to minimize the effect. For example, as noted in Section 3.8 on calibration, peak positions for water vapor are still determined visually. Determination

of the positions of the water vapor peaks mathematically is not trivial because of the highly irregular shape in the region of maximum intensity due to spectral noise. Thus to minimize systematic error from human bias, multiple standard peaks are used to obtain any shift.

These methods were started in earnest during this author's work for M.Sc. thesis[44] which described in detail much of the statistics. The methods were extended during the present work to the remaining calculations, and existing programs enhanced with the use of median based statistics and Monte Carlo methods.

Chapter 4

First overtone band of hydrogen

4.1 Introduction

Before proceeding to the first overtone band, it is worthwhile to note that in the fundamental band, which contains absorption from both overlap and quadrupolar induction mechanisms, the use of the Birnbaum-Cohen lineshape (equation 2.46) was found to give a high quality fit to the spectra, in particular in the wings. Figures 4.1, 4.2 and 4.3 show the BC lineshape applied to data collected by Youden[58] in this labratory using a stainless steel cell with a two cm sample pathlength.

4.2 Experimental Details

The data of the first overtone band of hydrogen discussed in this chapter, was gathered earlier by van Nostrand[16] in this laboratory, who performed experiments at three different temperatures. Forty-eight densities of hydrogen were examined in total, and specific details are given in Table 4.1. The analysis of the data by van Nostrand included the calculation of the absorption coefficients and a nonlinear fit to the spectrum using the

Table 4.1: Experimental details

Temperature	Path length	Number of densities used	Maximum density
K	cm		amagat
77	194.6	14	365
201	194.8	18	403
295	209.7	16	433

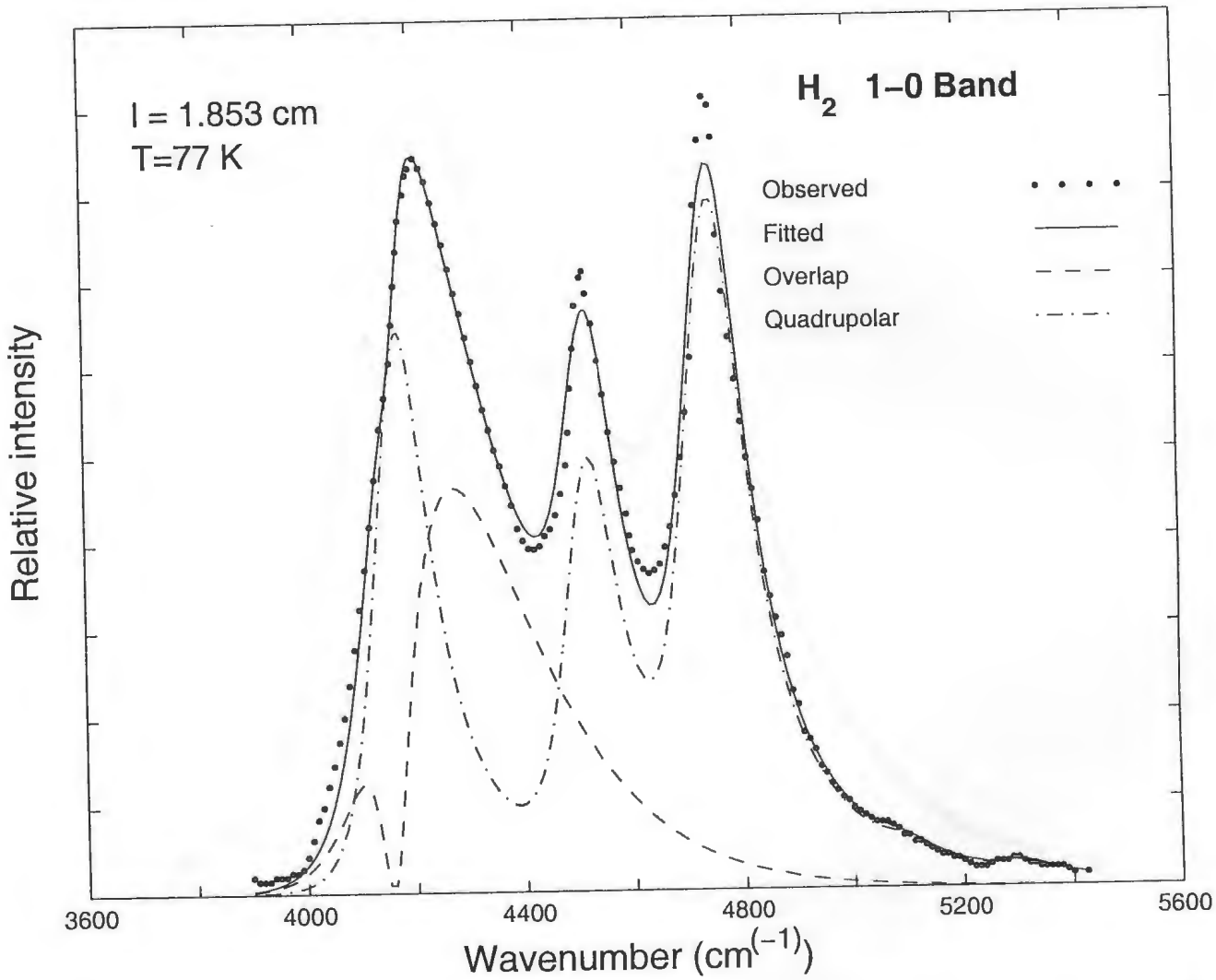

Figure 4.1: Analysis of an absorption profile for the fundamental band of hydrogen at 77 K.

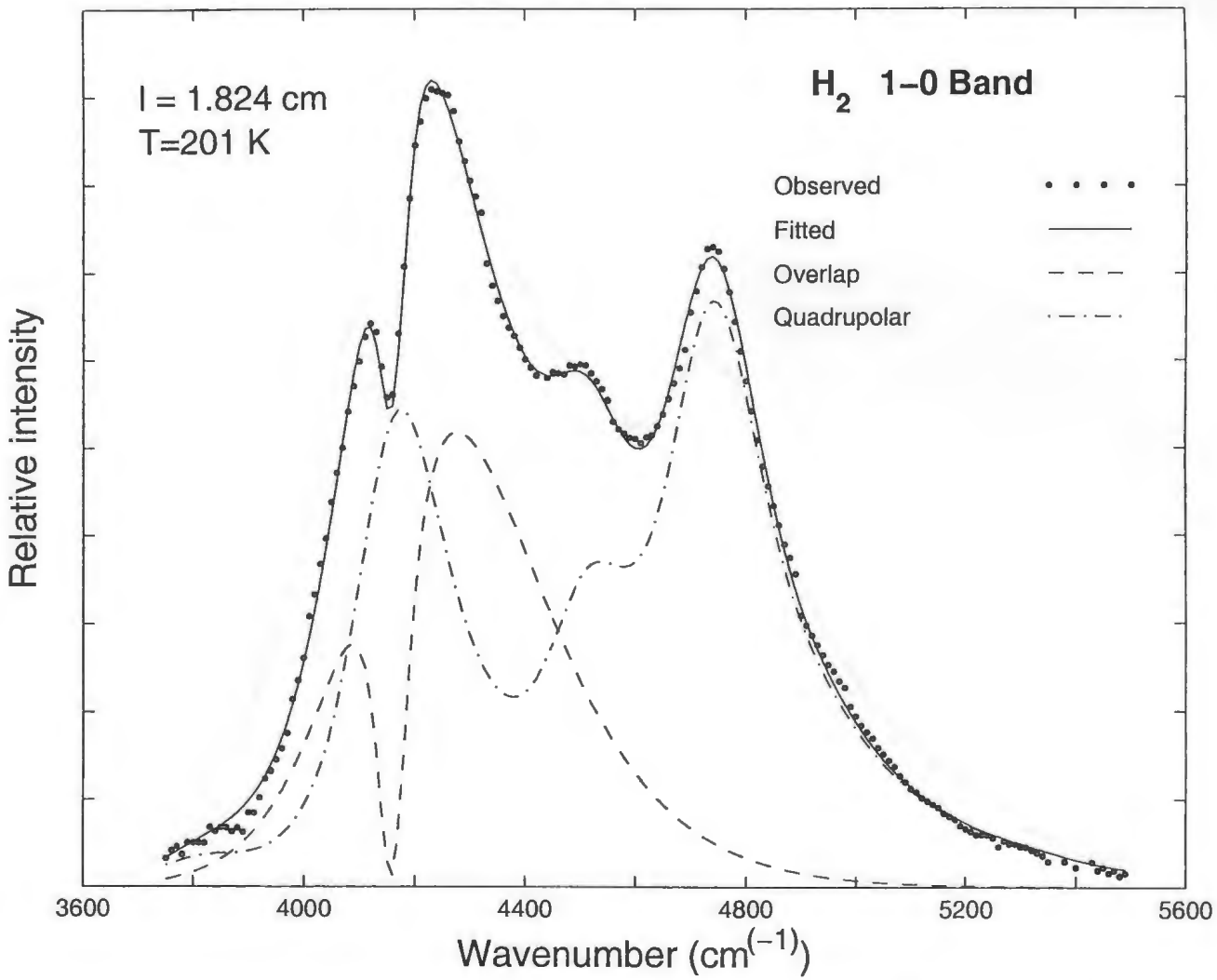

Figure 4.2: Analysis of an absorption profile for the fundamental band of hydrogen at 201 K.

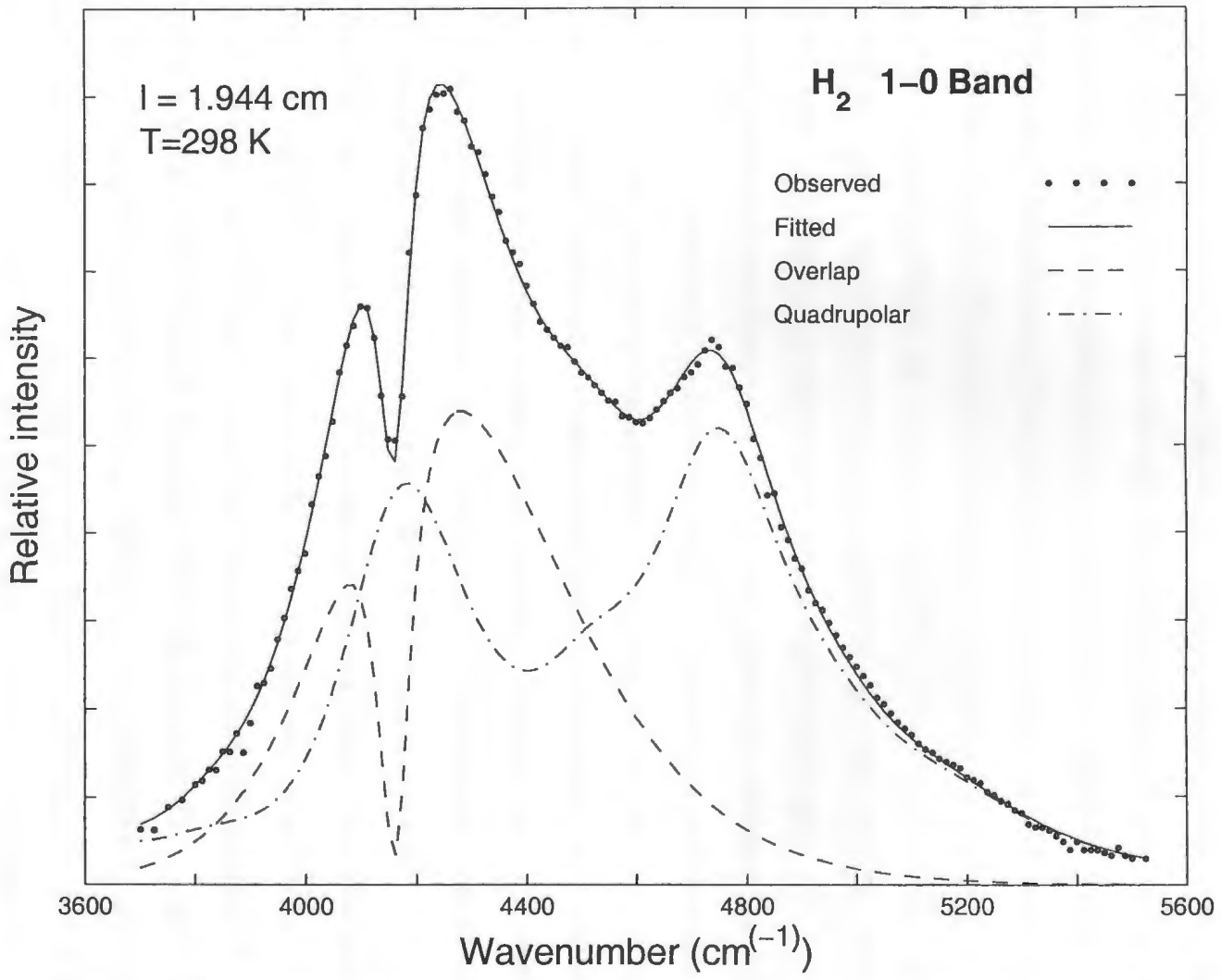

Figure 4.3: Analysis of an absorption profile for the fundamental band of hydrogen at 298 K.

modified Lorentzian lineshape function.

The results presented here offer two refinements to the lineshape analysis performed by van Nostrand. First, the more recent Birnbaum Cohen lineshape function was used as an update to the modified Lorentzian lineshape function to provide a better fit, especially in the wings of the spectra. Secondly, and the main point of the reanalysis, was an exploration of the density dependence of the matrix adjustment factor used by van Nostrand to allow a satisfactory fit of the experimental data. The proposal and implementation of the matrix adjustment factor was originated by Gillard[17] to explain a discrepancy in the overtone band of deuterium between the observed and fitted spectra. A similar method was used by Xiang[41] on the second overtone band of hydrogen.

Essentially Gillard noticed there was a distinct and systematic difference between the $\Delta v = 1$ and $\Delta v = 2$ transitions, specifically the $\Delta v = 2$ transitions were too high and thus reduced the corresponding matrix elements to compensate. This was not a proposal of the need to correct the matrix elements themselves, this was just a computationally efficient way to effect the necessary alterations to the intensity of the $\Delta v = 2$ transitions. Gillard investigated the adjustment factor over a range of magnitudes and concluded that 0.68 was optimal considering its average effect on all spectra recorded.

The present work is an extension of the method used by Gillard, van Nostrand and Fan. Here the analysis procedure was modified by including the correction factor as a direct parameter in the nonlinear fitting. This was accomplished by merging the program which calculated the necessary intensities with the program which implemented the Levenberg-Marquardt algorithm. This modification to the FORTRAN code allowed the optimal correction factor for each spectra to be determined directly by including the correction factor as a parameter in the nonlinear fitting. This was not possible at the time the data were collected due to the complexity of the calculations and the computational resources available. The individual correction factors determined from the nearly

fifty spectra showed a clear linear dependence on density of hydrogen and temperature of the system.

4.3 Absorption Profiles

Three example absorption profiles of the first overtone band of hydrogen, one for each of the temperatures, 77 K, 201 K and 295 K, are shown in Figure 4.4. Like all spectra produced from collision induced dipoles, these show the characteristic broad peaks as compared to the much sharper transitions seen in allowed absorption.

The most striking feature of the profiles is the total lack of absorption from the overlap induction mechanism. While the overlap induction mechanism features quite strongly in the fundamental band of molecular hydrogen as well as the second overtone band, it can be inferred to be absent from the first overtone band due to the complete lack of any dip in the spectra, a critical feature of absorption induced by the short range overlap induction.

It is also clear from a quick visual overview that there is a strong temperature dependence on the width of the peaks as the features narrow and become more distinct as the temperature drops. The reduction in width of the components, which is directly translated to the overall profile, is due to the drop in kinetic energy of the molecules at lower temperatures which results in longer collision durations.

The observed spectra peaks have been labeled with the corresponding component assignment given in Table 4.2 (except for the first peak, all the peak positions were determined by van Nostrand). It is observed that the features become more refined at lower temperatures and additional peaks become visible due to an increase in separation between the various components. In particular the 77 K profile clearly shows two peaks, (5) and (8), which are not readily visible in the spectra recorded at 201 and 295 K.

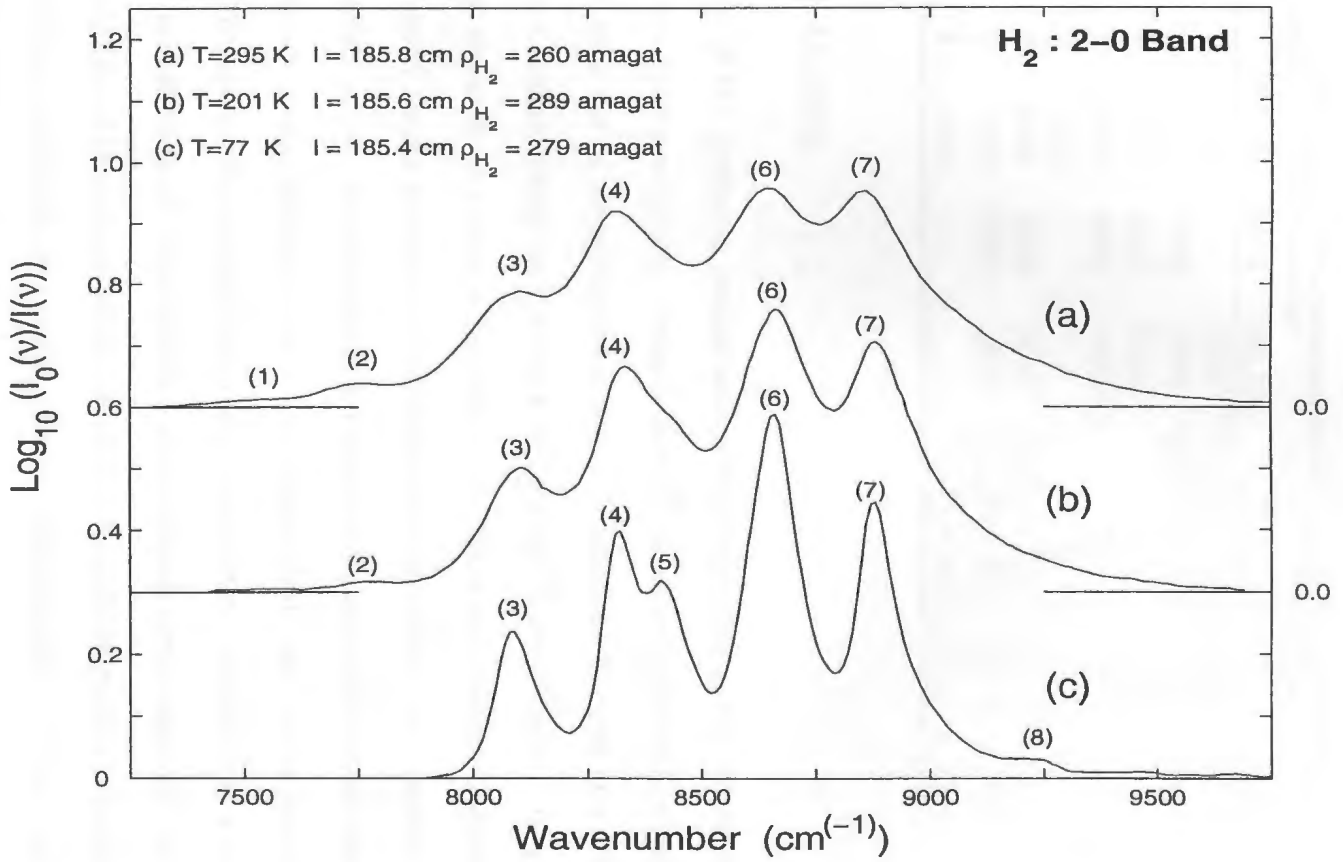

Figure 4.4: Profiles of the collision-induced absorption of H_2 in the first overtone region. See Table 4.2 for peak assignments.

Table 4.2: Assignment for the absorption peaks of the H_2 first overtone band in the pure gas at 77, 201 and 295 K

Peak	Wavenumber			Transitions
	77 K	201 K	295 K	
1			7578	$Q_2(J) + O_0(3), O_2(3) + Q_0(J)$
2		7750	7750	$Q_2(J) + O_0(2), O_2(2) + Q_0(J)$
3	8085	8100	8100	$Q_2(J) + Q_0(J)$
4	8310	8325	8320	$Q_1(J) + Q_1(J)$
5	8410			$Q_2(J) + S_0(0)$
6	8655	8660	8660	$Q_2(J) + S_0(1)$, $Q_1(J) + S_1(0)$
7	8875	8875	8870	$Q_2(J) + S_0(2)$, $Q_1(J) + S_1(1)$
8	9200			$S_2(1) + S_0(1)$, $S_1(1) + S_1(0)$

4.4 Profile Analysis

The generation of the synthetic profile was carried out using a non linear least squares fitting procedure developed in the previous work[44] based on programs originally written by Gillard[17] with use of algorithms outlined in Numerical Recipes and refinements to the convergence criteria based on the work of Le Roy[59] and Watson. It was extended in the current research as noted in section 4.1 to allow an efficient exploration of the matrix adjustment factor as well as modified with extensions for stability and speed such as the ability to perturb the calculated parameters and refit to test robustness and the "compaction" of intensities to allow for a quick first pass fit to generate baseline parameters. The compaction would take a set of intensities and generate a set of pseudo-intensities by compacting all lines within a user defined percentage into one line. This reduced the number of transitions which needed to be calculated per iteration. This was turned off after the initial set of parameters were determined and then the fitting was redone with the full intensity list for maximum precision.

Using the calculated intensities for the spectral components and the Birnbaum-Cohen

lineshape function in the nonlinear fitting program it was found that the agreement between the observed and fitted spectra was rather poor with the calculations performed by van Nostrand. An example of such a fit at 77 K is shown in Figure 4.5.

As previously noted, a similar discrepancy was studied in detail by Gillard[17] in the first overtone band of deuterium. A systematic analysis of the difference between the observed and fitted profiles lead to the discovery of a systematic pattern of too much relative intensity for the transitions involving a vibration change of $\Delta v = 2$. This systematic difference is illustrated at 77 K in Figure 4.6. The same discrepancy was also found to be present in the 201 and 295 K spectra. When the fit was adjusted so that the observed and calculated spectra agree in the regions dominated by the 1-1 transitions (which refer to when $\Delta v = 1$ for both collision partners) namely peaks 4 and 7, the intensity is too high in the regions which are dominated by the 2-0 transitions (which refers to when $\Delta v = 2$ for one molecule and $\Delta v = 0$ for the other which makes a pure rotational transition).

To reduce the intensity of the 2-0 transitions, the corresponding quadrupolar matrix elements were reduced via a multiplicative factor. This factor was adjusted until a best fit was obtained using least squares criteria. Using a similar procedure van Nostrand optimized the synthetic profiles of the first overtone band of hydrogen and found that an average reduction factor of 0.68 gave the best fit for all spectra. Gillard performed the same procedure and found the same average factor to be optimal for the first overtone band of D_2. Xiang used a similar method with the same adjustment factor in the second overtone band of hydrogen.

It should be noted clearly that this correction method does not imply that there is an inherent problem with the quadrupolar matrix elements. The uncertainty or error in the calculated matrix elements is very small, not nearly large enough to induce the magnitude of discrepancy being observed. This reduction of the $\Delta v = 2$ quadrupole matrix elements

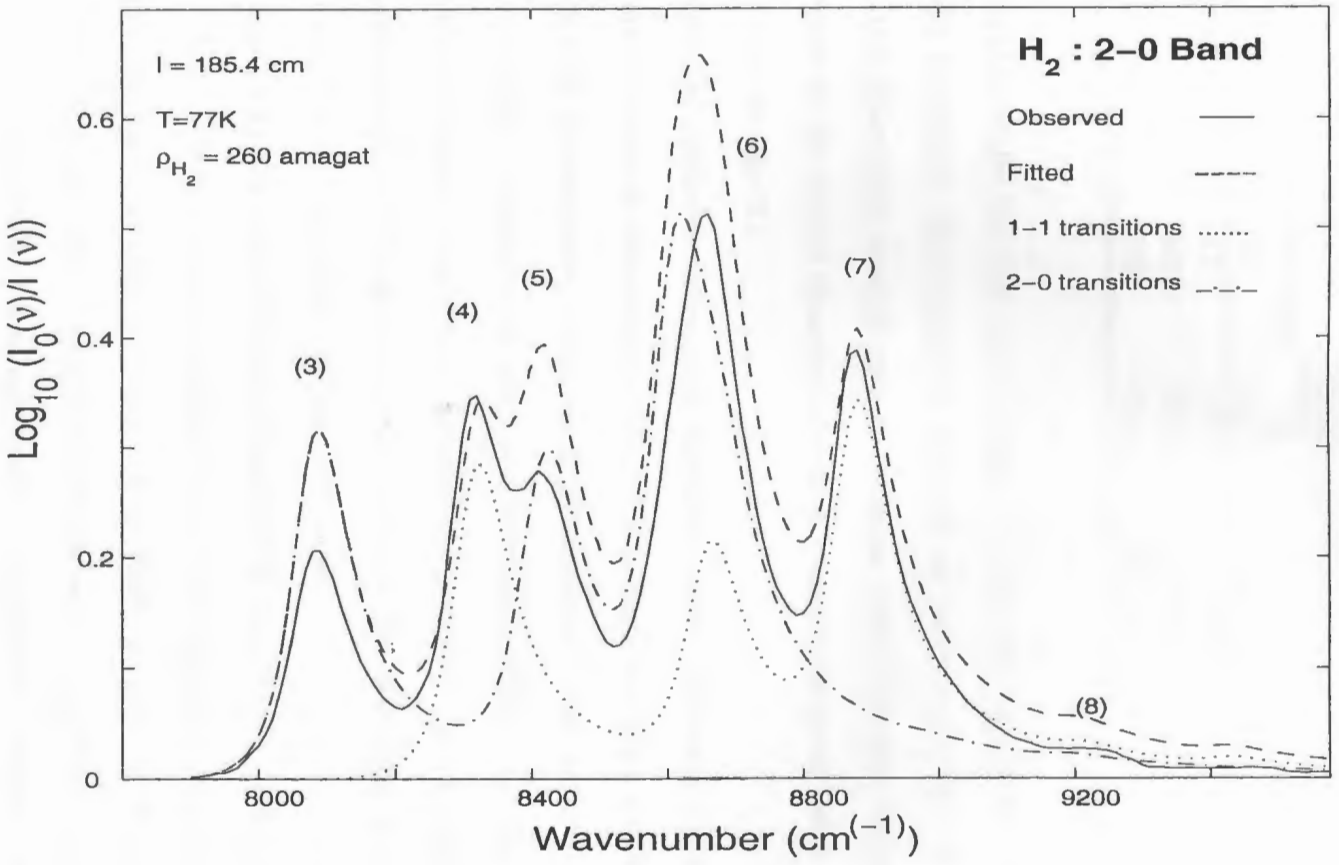

Figure 4.6: A contrast of the 1-1 and 2-0 transitions in a spectrum from the first overtone band of hydrogen at 77 K

Table 4.3: Results of Profile Analysis

Temperature (K)	Halfwidth Parameters δ_1 cm^{-1}	δ_2 cm^{-1}
77	57(3)	108 (20)
201	96(2)	197 (18)
295	120(3)	227 (11)

was just a computationally efficient way to adjust the necessary intensities. The physical behavior of this systematic discrepancy is proposed to be the influence of the mixing term between the anisotropic overlap and quadrupolar induction term which induces a negative influence on the overall absorption of those transitions being reduced as noted by equation 2.11 in section 2.1.

Implementing the nonlinear fitting with the more recent Birnbaum-Cohen lineshape function and matrix element reduction, the Birnbaum-Cohen lineshape was found to give a better fit in a least squares sense (lower residuals) than the fourth power law lineshape used by van Nostrand. In agreement with van Nostrand, Figure 4.7 shows the huge increase in quality of fit due to the use of the matrix adjustment factor, this is the same experimental spectrum at 77 K as shown in Figure 4.5, the difference in agreement is simply due to the effect of the matrix adjustment factor.

Figures 4.8 and 4.9 show sample fits at 201 and 295 K respectively which also show the strong effect of the matrix adjustment factor. Due to the significant increase in number of components at the increased temperatures, 74 for 201K and 101 for 295 K, compared to just 28 at 77 K, the individual component profiles were not plotted for clarity. The fits at 201 and 295 K show the same high quality of agreement between the observed and fitted spectra as the 77 K profiles. The fitted lineshape parameters for all three temperatures are presented in Table 4.3.

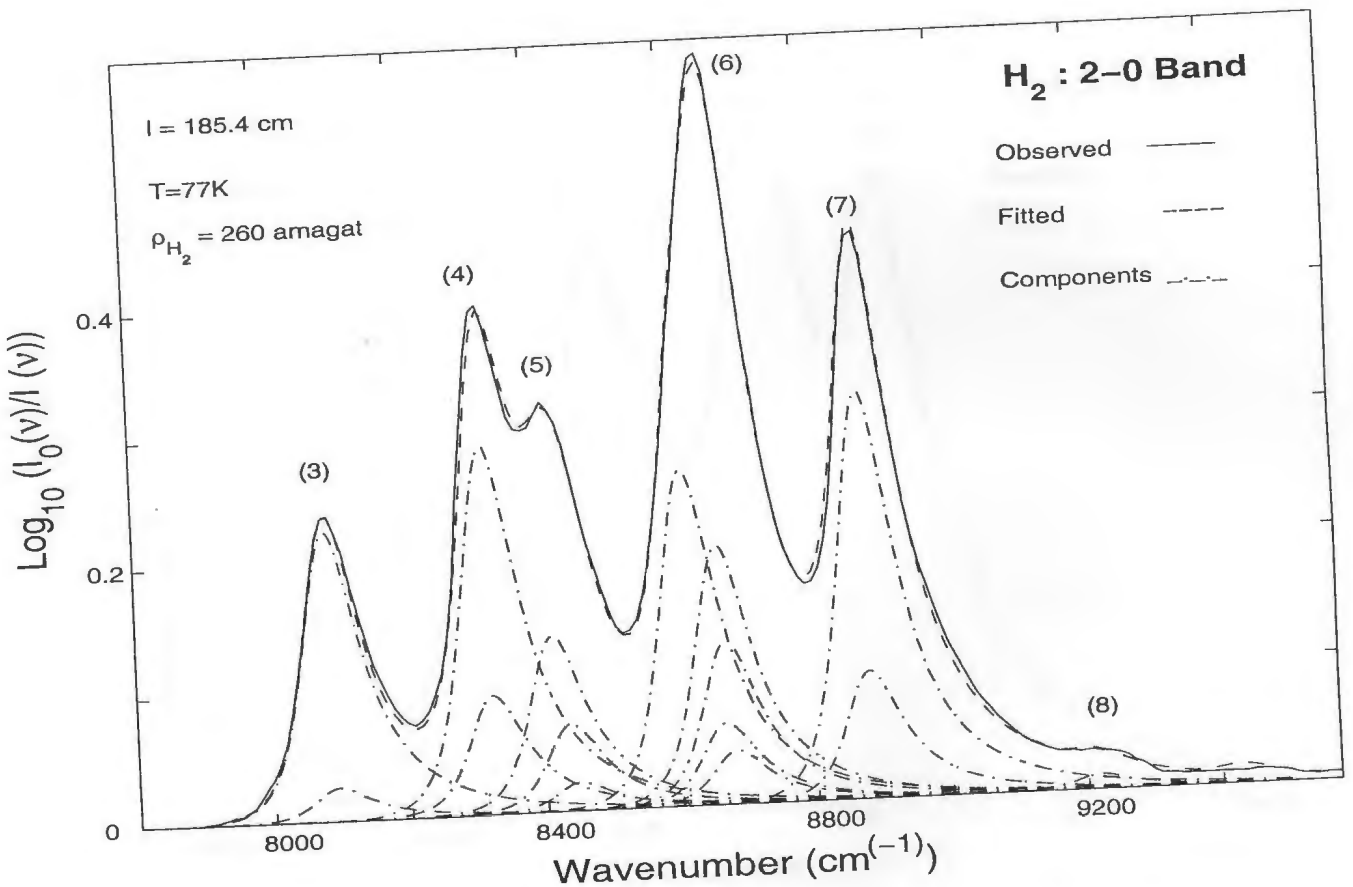

Figure 4.7: Analysis of an absorption profile for the first overtone band of hydrogen at 77 K, with quadrupole matrix element adjustment factor.

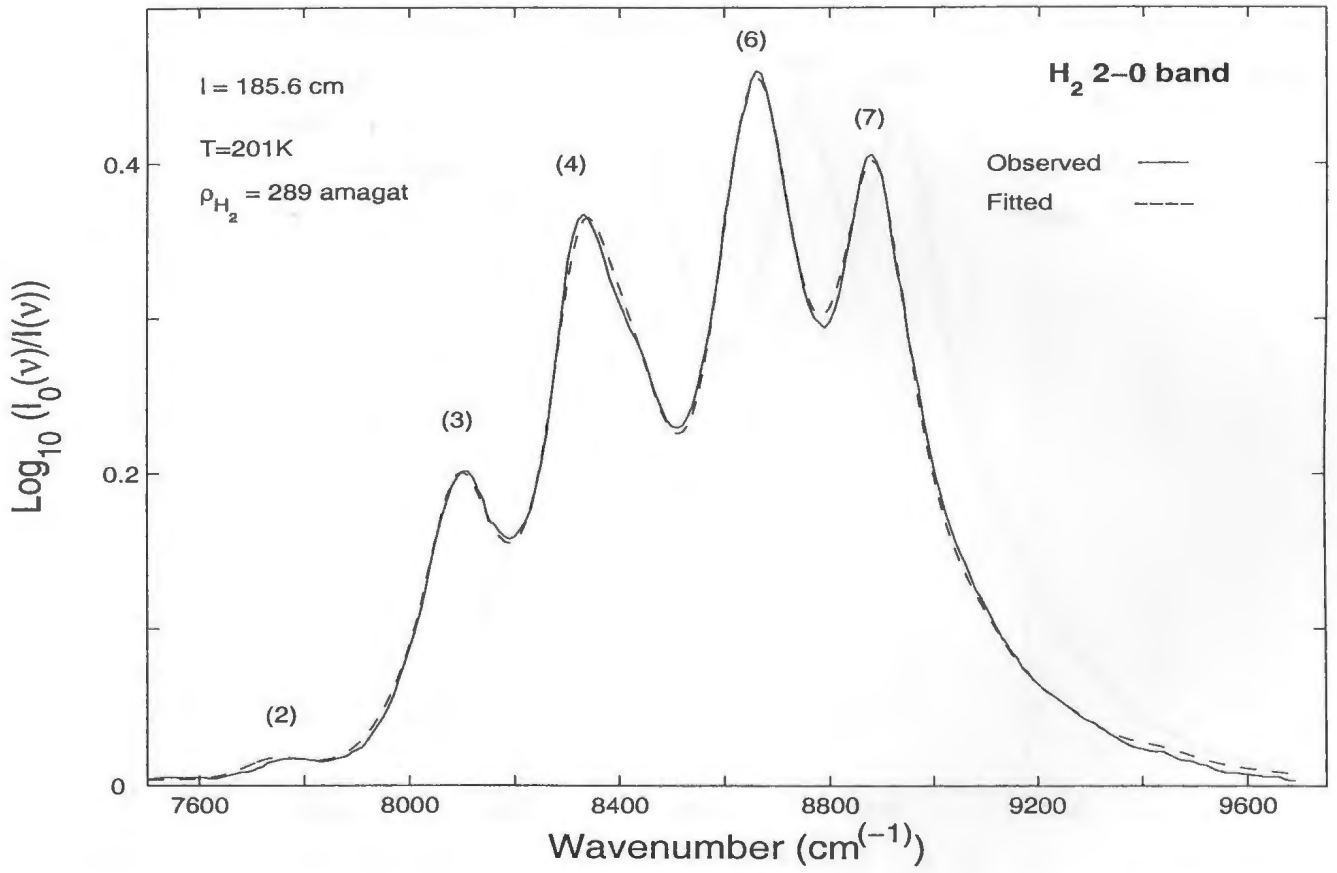

Figure 4.8: Analysis of an absorption profile for the first overtone band of hydrogen at 201 K, with quadrupole matrix element adjustment factor.

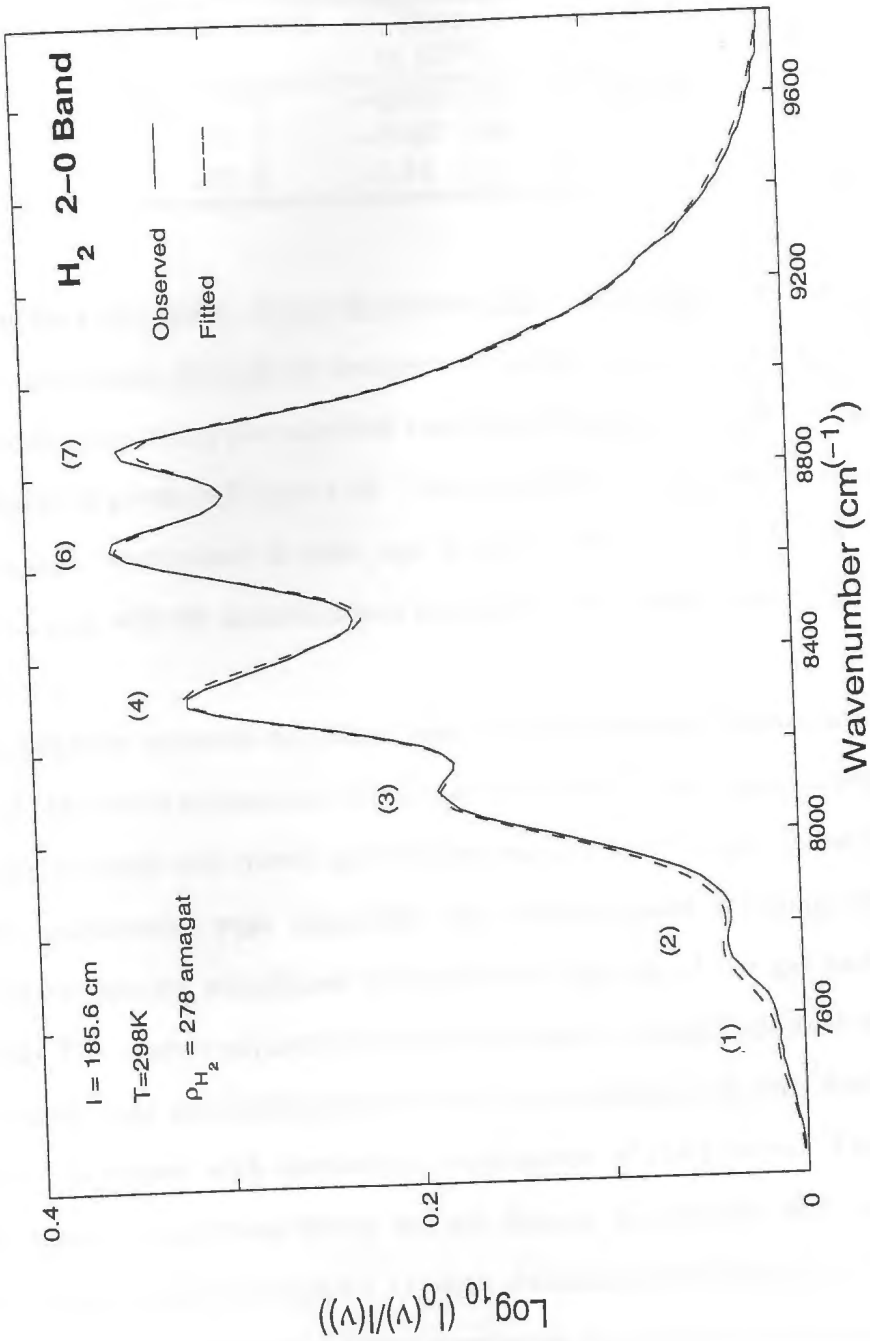

Figure 4.9: Analysis of an absorption profile for the first overtone band of hydrogen at 295 K, with quadrupole matrix element adjustment factor.

Table 4.4: Matrix adjustment factor statistics

Temperature	Slope (x 10^{-3})	Intercept
77 K	−0.481 (15)	0.8046 (40)
201 K	−0.497 (38)	0.779 (10)
295 K	−0.54 (11)	0.777 (27)

The molecular halfwidth δ_1 of the Birnbaum-Cohen lineshape were found to correlate strongly with the square root of the temperature which was found by Van Nostrand for the δ_1 parameter when using the modified Lorentzian lineshape. A plot showing the clear linear correlation is given in Figure 4.10. The slope of the least squares determined line, with the intercept constrained to zero, was found to be 6.83 +/- 0.44 $cm^{-1}/\sqrt{K}$. A fit was also performed with an unconstrained intercept, which was found to not significantly differ from zero.

With the behavior reported by Gillard and others confirmed, a systematic study of the magnitude of the matrix adjustment factor was performed for all spectra, determining the optimal factor for each individual spectrum at each density for all three temperatures. Once all the calculations were completed the results showed a strong and systematic correlation of the matrix adjustment factor to both density of the gas and temperature of the system. The matrix adjustment factor increased in magnitude with decreasing gas density, however does not extrapolate to one (no correction) at zero density, and to a smaller extent increased with decreasing temperature of the system. This relationship between the matrix adjustment factor and the density of hydrogen and the temperature of the system can be seen in Figure 4.11, with statistical details given in Table 4.4.

It is clear there is a very strong linear correlation at all three temperatures, and aside from some spectra with high scatter at low densities (due to the recorded intensities

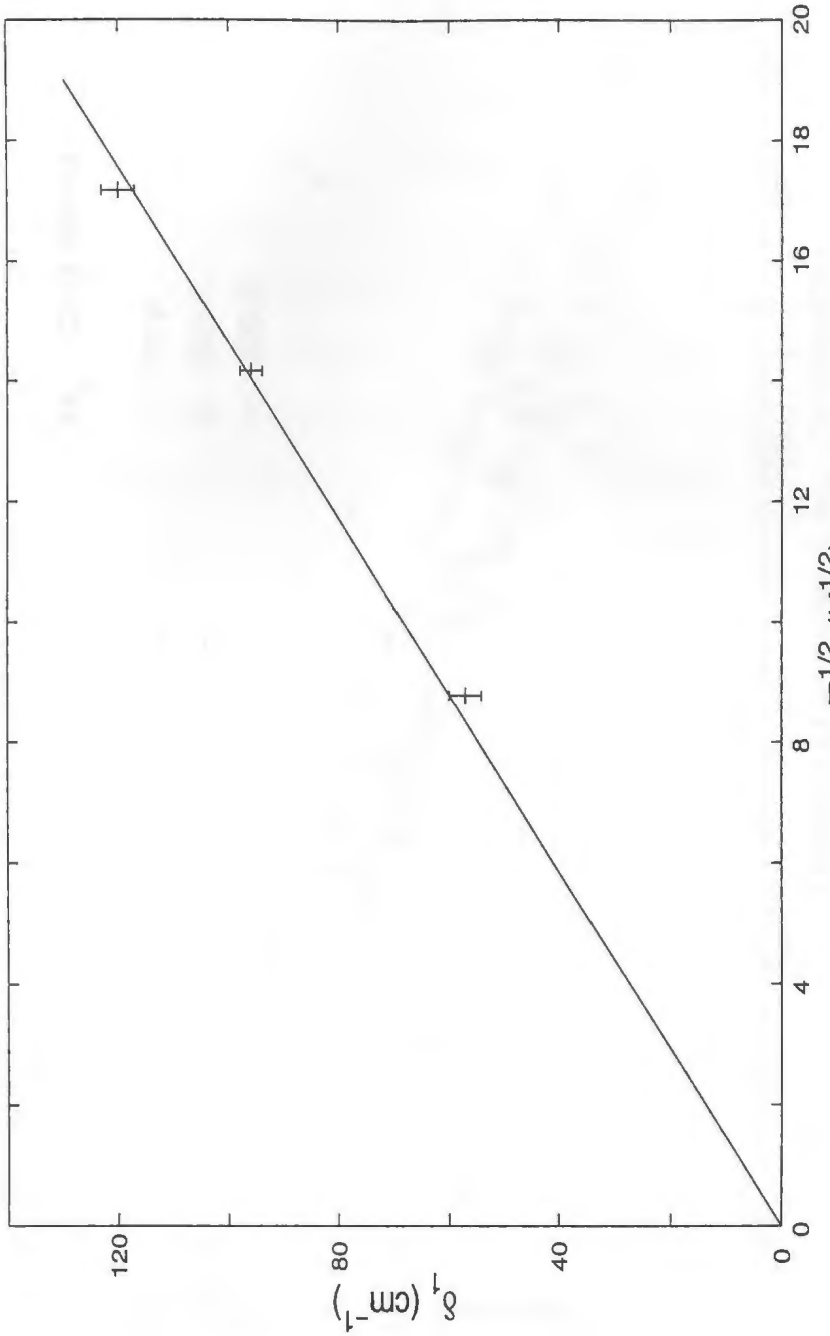

Figure 4.10: The temperature dependence of the BC lineshape parameter δ_1 on density of hydrogen.

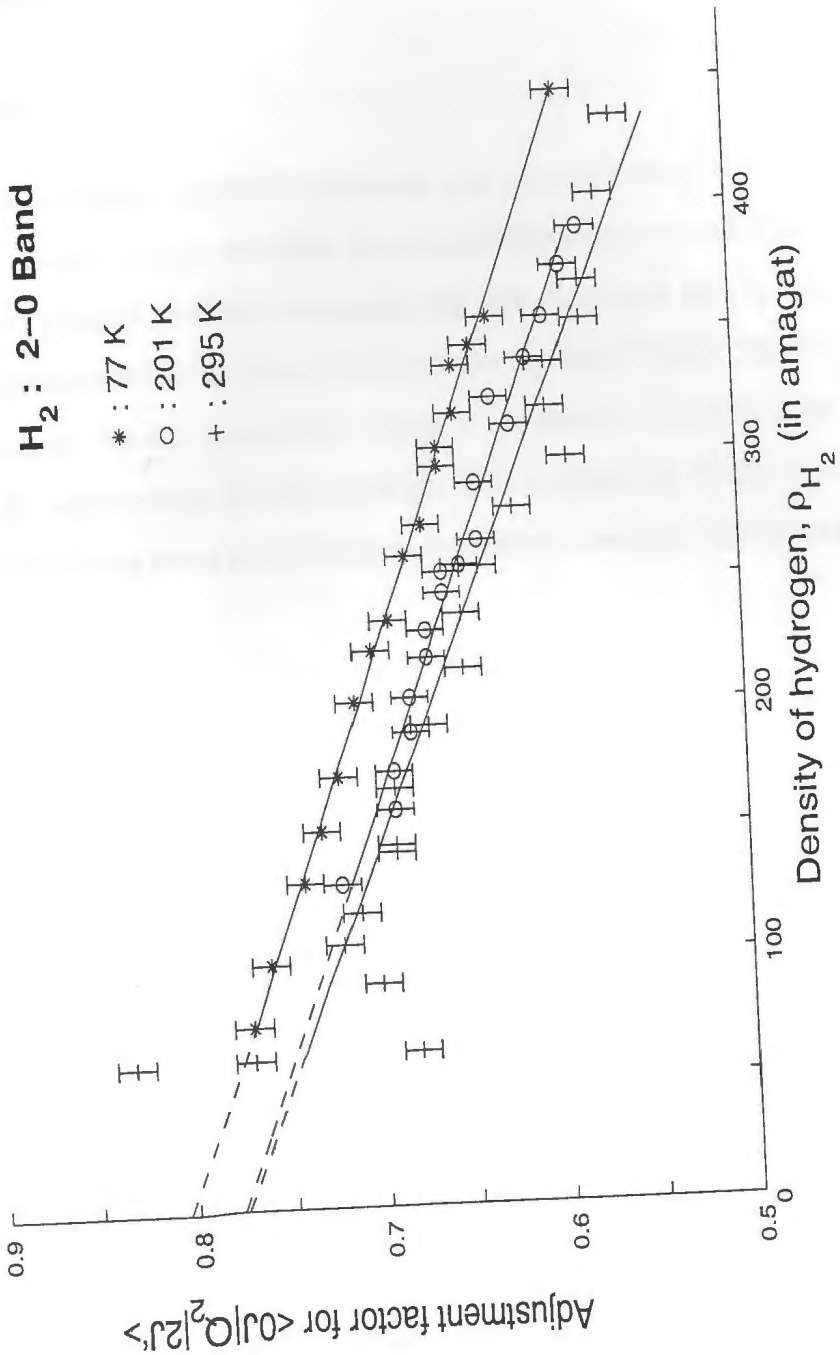

Figure 4.11: Matrix adjustment factors plotted against density of hydrogen at 77, 201 and 295 K. The solid lines are the fits with the dashed lines being the extrapolation to zero density of hydrogen.

being very weak and thus having a low signal to noise ratio), there seems to be a clear temperature separation especially if the 77 K and 295 K data are compared.

4.5 Conclusion

The spectra of first overtone band of hydrogen was analyzed using the Birnbaum-Cohen lineshape as an update to the modified Lorentzian lineshape. In addition, the average matrix adjustment factor of 0.68 determined by van Nostrand was optimized for each spectrum for all densities at the three temperatures studied. These "fudge factors" were found to be strongly density dependent, slightly correlated to temperature, and to not extrapolate to no adjustment at zero density. This adjustment factor is interpreted as the influence of a mixing term containing an anisotropic overlap component.

Chapter 5

The fundamental band of D_2 in D_2-N_2 and D_2-CO mixtures

5.1 Introduction

Collision-induced absorption (CIA) of the infrared fundamental band of D_2 in the pure gas was studied at room temperature by Reddy and Cho[48] and at 22 to 77 K by Watanabe and Welsh[60]. Penny et al.[61] investigated the band in the pure gas at 77, 196 and 298 K and analyzed the absorption profiles using the Levine-Birnbaum line-shape function in the form of a modified Bessel function of the second kind and Van Kranendonk's dispersion-type line-shape function for the intracollisional and intercollisional part, respectively, of the overlap-induced Q components and the symmetrized dispersion line-shape function for the quadrupole-induced O, Q and S transitions. Gillard et al.[62] investigated the $S_1(J) + S_0(J)$ transitions of D_2 in the pure gas at 77 K, also in our laboratory.

The enhancement spectra of the CIA of the fundamental band of D_2 in binary mixtures with He, Ar, and N_2 at room temperature were observed by Pai et al.[63] and with He and Ne at different temperatures in the range 77-298 K by Russell et al.[64]. Those two experimental studies were performed without a detailed analysis of the absorption profiles; the quadrupolar contribution was calculated from the molecular constants of the colliding partners and the overlap contribution was obtained by subtracting the calculated quadrupolar contribution from the total absorption of the band.

In the present chapter the results of a study of the enhancement absorption of data collected by G. Varghese on the fundamental band of D_2 in D_2-N_2 and D_2-CO mixtures

is reported. These experiments were carried out with base densities of D_2 in the range 12 to 20 amagat and the total gas densities up to 130 amagat. When the data were collected the methods used to fit such spectra had not been developed in our laboratory which prevented the analysis from being performed until recently. This chapter presents the results of those methods being applied to these data, in particular the necessary frequencies and intensities for the required transitions were calculated to allow the spectra to be modeled with various semi-empirical lineshapes, and the binary and ternary absorption coefficients of the absorption profiles were determined along with other characteristic spectral quantities such as the band center and division of contributions from the quadrupolar and overlap induction mechanisms to the total profile intensity.

5.2 Experimental Details

A transmission-type absorption cell of sample path length 105.2 cm constructed of stainless steel[43] was used to contain the experimental gases. A Perkin-Elmer Model 112 single-beam double-pass spectrometer equipped with a LiF prism and a Golay detector was used to record the spectra. The light source was a water-cooled Globar operated at about 150 W. An instrumental slit width of 100 μm gave a spectral resolution of 3 cm^{-1} at 2994 cm^{-1}, the origin of the fundamental band of D_2. The known absorption frequencies of atmospheric water vapor [65] and of liquid indene bands [53] were used to calibrate the spectral region. Since the spectral region of D_2 in its high wavenumber wing overlaps with water vapor absorption bands, the optical path was boxed in a polyethylene enclosure which was continuously flushed with dry nitrogen gas.

For the experiments, research grade D_2 and N_2 were supplied by the Matheson Company of Canada. The base densities of D_2 were obtained directly from its isothermal

data[66] and along with the isothermal data of N_2[67] and CO[68] was used in an interpolation method described previously in section 3.6 to determine the partial densities of N_2 and CO.

5.3 Absorption Profiles and Absorption Coefficients

A set of typical experimental profiles of the enhancement of absorption of the induced fundamental band of D_2 in D_2-N_2 and D_2-CO mixtures at room temperature are presented in Figures 5.1 and 5.2 respectively. The base density of D_2 for both mixtures was 15.1 amagat. The positions of the single transitions $O_1(J)$ with J = 2 and 3, $Q_1(J)$ and $S_1(J)$ with J = 0 to 4, calculated from the molecular constants of the free D_2 molecule[69], are marked on the wavenumber axes. All profiles show the usual splitting of the Q branch into two well-defined Q_P and Q_R components with their minima at the position of $Q_1(0)$. The splitting is similar to that observed in the fundamental band of H_2 which is explained by Van Kranendonk[29] as an interference phenomenon occurring between the overlap dipole moments in successive collisions. In the collision-induced-fundamental band of D_2 the isotropic part of the polarizability of D_2 in the quadrupole-induction mechanism contributes to the intensity of the transitions $O_1(J)$, $Q_1(J)$ and $S_1(J)$. The isotropic electron overlap induction mechanism, on the other hand, contributes entirely to the $Q_1(J)$ transitions. The enhancement in the integrated absorption coefficient can be expressed as an expansion in density as shown in section 2.2.

Plots of $(1/\rho_a\rho_b)\ \alpha_{en}$ against ρ_b for both D_2-N_2 and D_2-CO mixtures are shown in Figure 5.3. The intercepts and slopes of the straight line graphs give the binary and ternary absorption coefficients, respectively, which are presented in Table 5.1. The enhancement in the integrated absorption coefficient can also be expressed in dimensionless

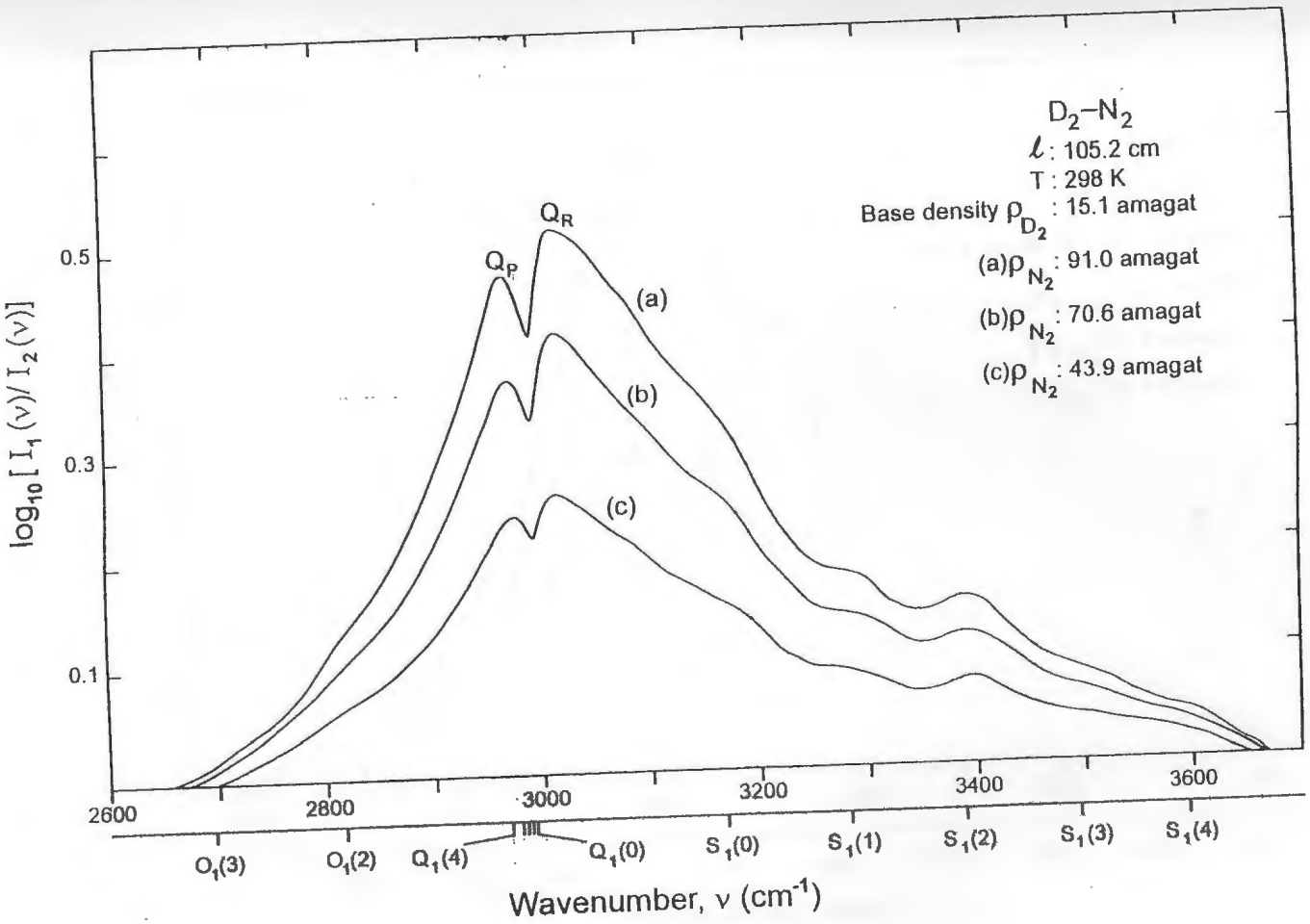

Figure 5.1: Three typical enhancement absorption profiles of the fundamental band of D_2 in D_2-N_2 mixtures at 298 K.

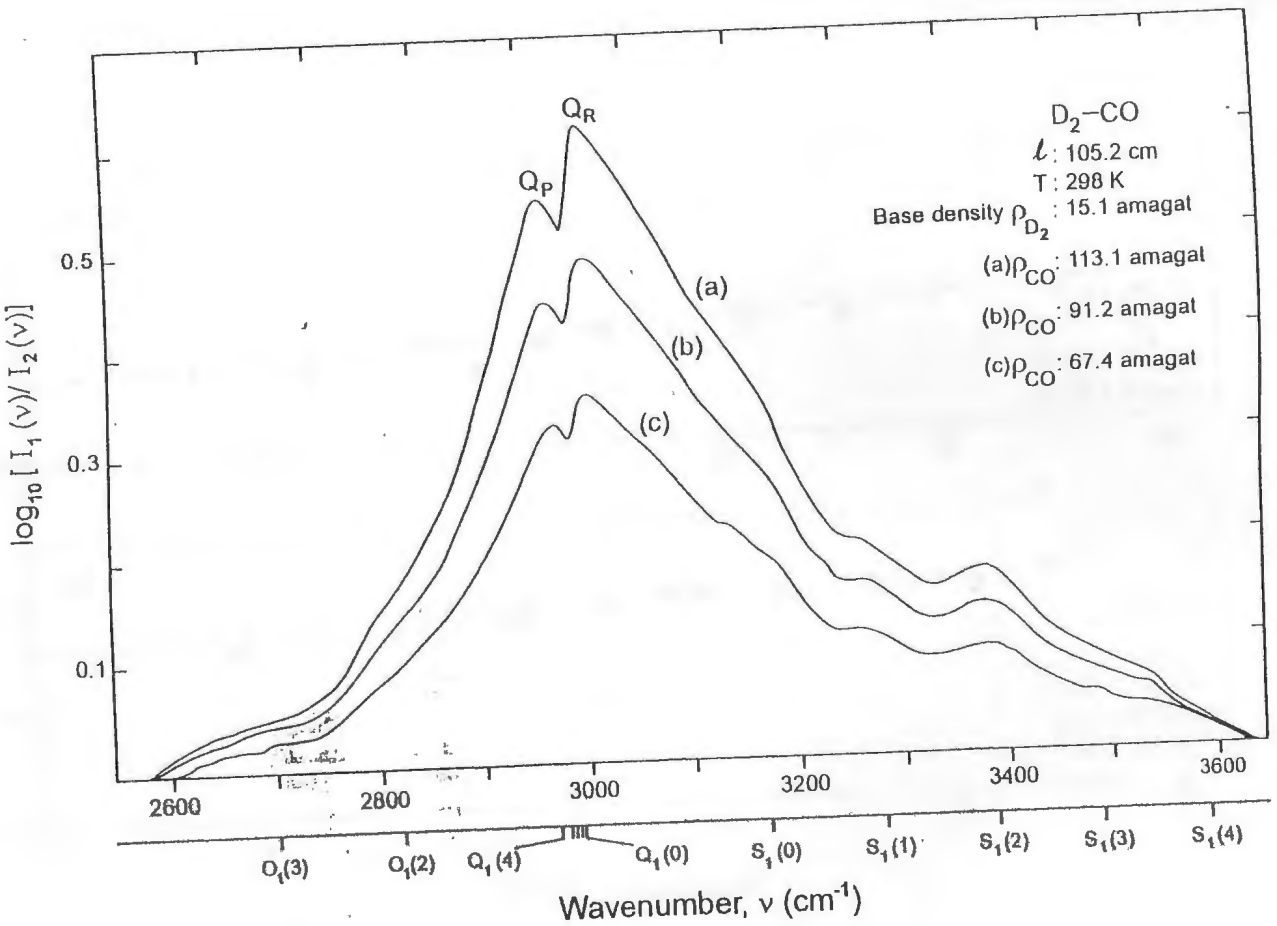

Figure 5.2: Three typical enhancement absorption profiles of the fundamental band of D_2 in D_2-C0 mixtures at 298 K.

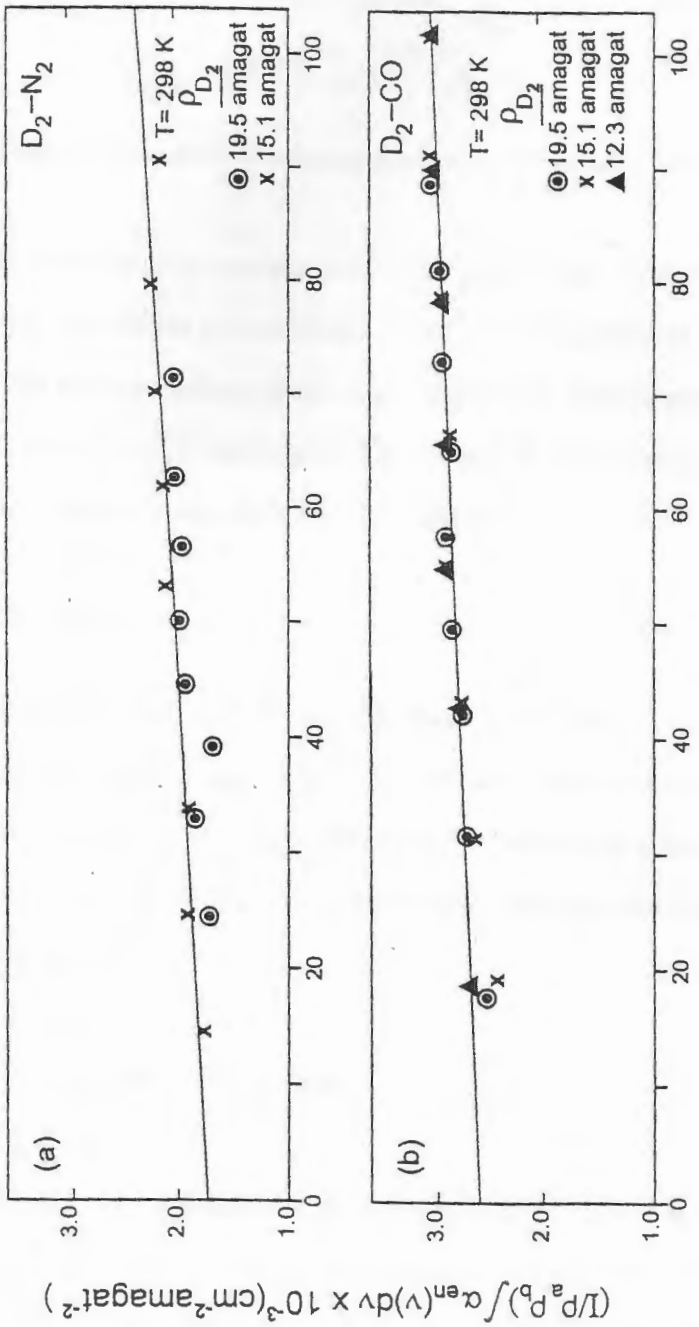

Figure 5.3: Plots of $(1/\rho_a\rho_b)\int \alpha_{en}(\nu)d\nu$ against ρ_b ($\rho_a = \rho_{D_2}$; $\rho_b = \rho_{N_2}$ or ρ_{CO})

Table 5.1: Absorption coefficients for the fundamental band of D_2 enhanced by nitrogen and carbon monoxide.

	Binary abs. coeff.		Ternary abs. coeff.
Mixture	α_{ab} (10^{-3}) cm^{-2} $amagat^{-2}$	$\tilde{\alpha}_{ab}$ (10^{-35}) cm^6 s^{-1}	α_{2ab} (10^{-6}) cm^{-2} $amagat^{-3}$
D_2 - N_2	2.82 (6)	3.73 (8)	5 (1)
D_2 -CO	2.61 (1)	3.53 (1)	3.9 (1)

form as shown previously in section 2.2. The new binary and ternary absorption coefficients represent transition probabilities induced in collisions of the type a-b and a-b-b respectively. The average values of the band center are 3140.0 cm-1 for D_2 - N_2 mixtures and 3074.8 cm-1 for D_2 - CO mixtures. The values of the absorption coefficients in cm^{-6} s^{-1} for these two mixtures are also listed in Table 5.1.

5.4 Profile Analysis

Using values of 1.22[3] and 1.27[26] for the quadrupole matrix element <Q> of N_2 and CO respectively, and 11.8[27] and 13.2[28] for the isotropic polarizability $< \alpha >$ of N_2 and CO respectively, the required binary absorption coefficients were calculated (equations 2.31 and 2.33). For D_2-N_2 or D_2-CO mixtures the following double transitions occur :

$O_1(J)$ (D_2) + $Q_0(J)$ $(N_2$ / CO)

$Q_1(J)$ (D_2) + $Q_0(J)$ $(N_2$ / CO)

$S_1(J)$ (D_2) + $Q_0(J)$ $(N_2$ / CO), and

$Q_1(J)$ (D_2) + $S_0(J)$ $(N_2$ / CO).

At room temperature the rotational quantum number J takes values 0 to 4 for D_2 and 0 to 25 for N_2 or CO. As a result, the computation for the overlap component was performed for five J values (0 to 4), but for the quadrupolar contribution there are a

Table 5.2: Overlap and quadrupolar components in the CIA 1-0 band of D_2 in D_2-N_2/CO mixtures at 298 K.

D_2 + N_2 / CO	Number of components
Overlap components	5
$Q_{Overlap}(J)$, J=0 to 4	
Quadrupolar components	
$O_1(J)$[1], j=2 to 4 + $Q_0(J)$[2], J= 0 to 25	78
$Q_1(J)$, j=2 to 4 + $Q_0(J)$, J= 0 to 25	130
$S_1(J)$, j=2 to 4 + $Q_0(J)$, J= 0 to 25	130
$Q_1(J)$, j=2 to 4 + $S_0(J)$[3], J= 0 to 25	130
Total number of quadrupolar components	468

[1] Subscript 1 indicates $\Delta v = +1$.
[2] $Q_0(J)$ indicates orientational transition.
[3] $S_0(J)$ indicates pure rotational transition.

series of transitions to be considered for each gas mixture producing five overlap and 468 quadrupolar transitions as listed in Table 5.2. These were used in the appropriate line-shape functions (equations 2.50 and 2.51) to compute the synthetic profile.

Examples of profile analysis of the enhancement absorption profiles of the D_2 fundamental band in D_2-N_2 and D_2-CO mixtures are shown in Figures 5.4 and 5.5. Here there is an overall good agreement between the experimental and synthetic absorption profiles. The best fits are obtained without any shift in the overlap components $Q_{ov}(J)$ but there is density-dependent negative shift for the quadrupolar components. The results of the profile analysis are presented in Table 5.3 which also includes the percentage contributions of the overlap and quadrupolar induction mechanisms to the enhancement profiles are also listed.

In the present profile analysis the BC lineshape function was also used for the quadrupole components, but did not provide an improvement over the dispersion lineshape. However

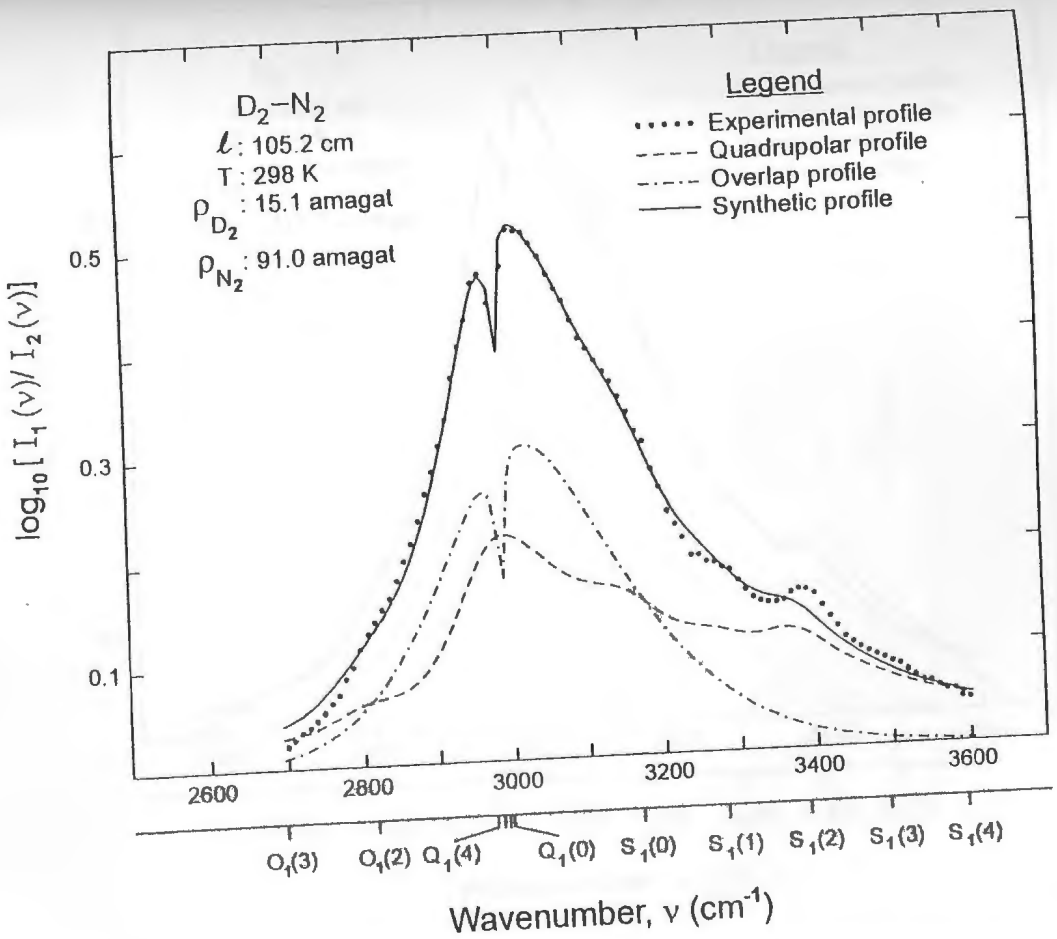

Figure 5.4: Analysis of an enhancement absorption profile of the fundamental band of D_2 in a D_2-N_2 mixture at 298 K. The dots (...) represent the experimental profile. The dashes (- - -) represent the sum of the quadrupolar components. The dash-dot curve (-.-) represents the sum of the overlap components. The solid curve is the total synthetic profile.

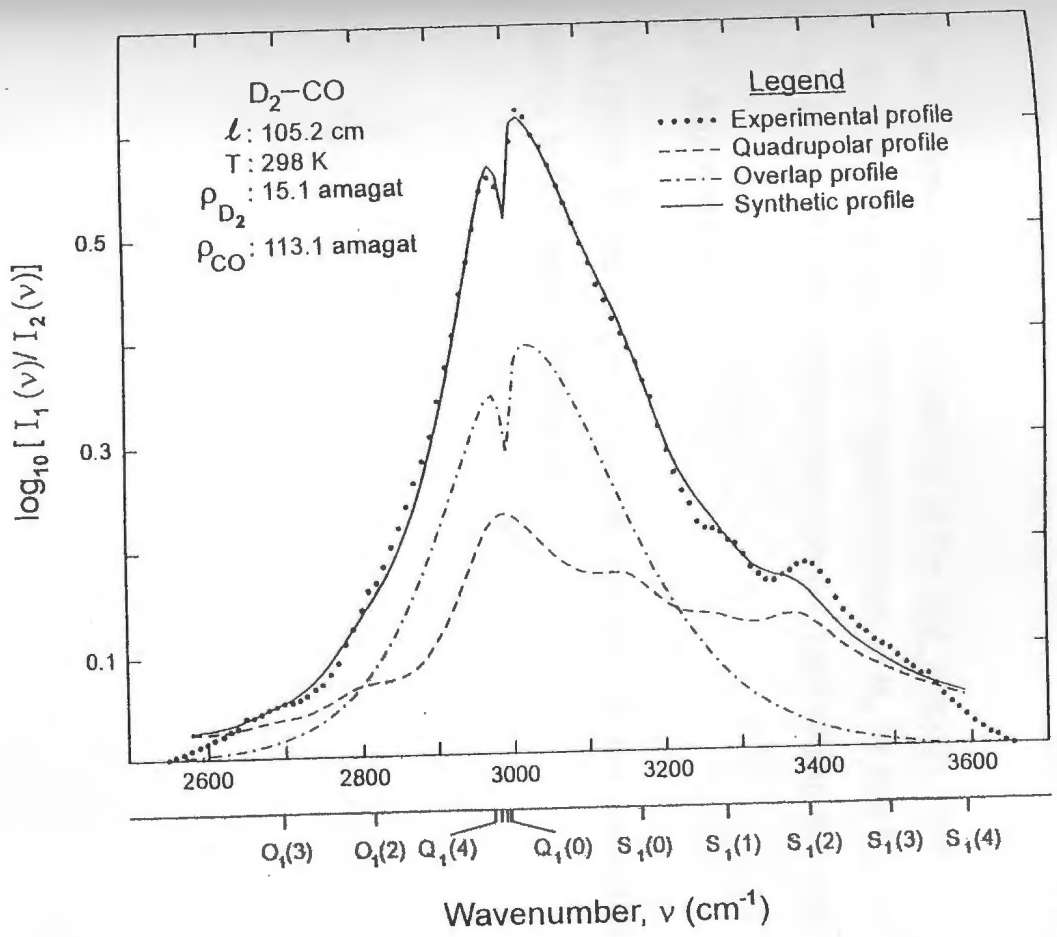

Figure 5.5: Analysis of an enhancement absorption profile of the fundamental band of D_2 in a D_2-CO mixture at 298 K. The dots (...) represent the experimental profile. The dashes (- - -) represents the sum of the quadrupolar components. The dash-dot curve (-.-) represents the sum of the overlap components. The solid curve is the total synthetic profile.

Table 5.3: Lineshape parameters for the fundamental band of D_2 enhanced by nitrogen and carbon monoxide.

Perturbing Gas	δ_d cm^{-1}	δ_c cm^{-1}	δ_q cm^{-1}	τ_d 10^{-14}	τ_q 10^{-14}	% Contribution Overlap	% Contribution Quadrupolar
N_2	131 (4)	1.5-2.5	71 (3)	4.1	7.5	46	54
CO	132 (2)	1.0-1.7	70 (3)	4.0	7.5	47	53

in the analysis of the CIA spectra of the first overtone band of H_2 in the pure gas at 77, 201 and 295 K and in the binary mixtures of H_2-Kr and H_2-Xe[62], the BC lineshape gave a better fit to the experimental spectra, especially in the wings.

5.5 Annotation

This results of this chapter have been published in the Journal of Quantitative Spectroscopy and Radiative Transfer[15].

Chapter 6

The fundamental band of D_2 enhanced by helium, argon, and krypton

The fundamental band of deuterium was studied in the binary mixtures of D_2-He, D_2-Ar, and D_2-Kr, for several base densities of D_2 and mixture densities of D_2 with He, Ar and Kr, at 298 K, details are given in Table 6.1.

6.1 Absorption Profiles

Three examples of the enhancement absorption profiles of the D_2-He mixtures are shown in Figure 6.1, similar profiles for the D_2-Ar enhancement band in Figure 6.2, and for the D_2-Kr enhancement band in Figure 6.3. As with all spectra produced from collision induced dipoles, these show the characteristic broad peaks as compared to the much sharper transitions seen in allowed aborption. The contribution of the overlap induction mechanism is quite strong as illustrated by the sharp dip at approximately 3000 cm^{-1}. The observed spectra peaks have been labeled with the corresponding component assignment given in Table 6.2.

Table 6.1: Experimental details

Gas	Number of base densities	Range of D_2	Number of mixtures	Range of perturber
		amagat		amagat
He	4	16 - 42	29	10 - 300
Ar	4	3 - 20	17	10 - 280
Kr	3	9 - 20	18	10 - 110

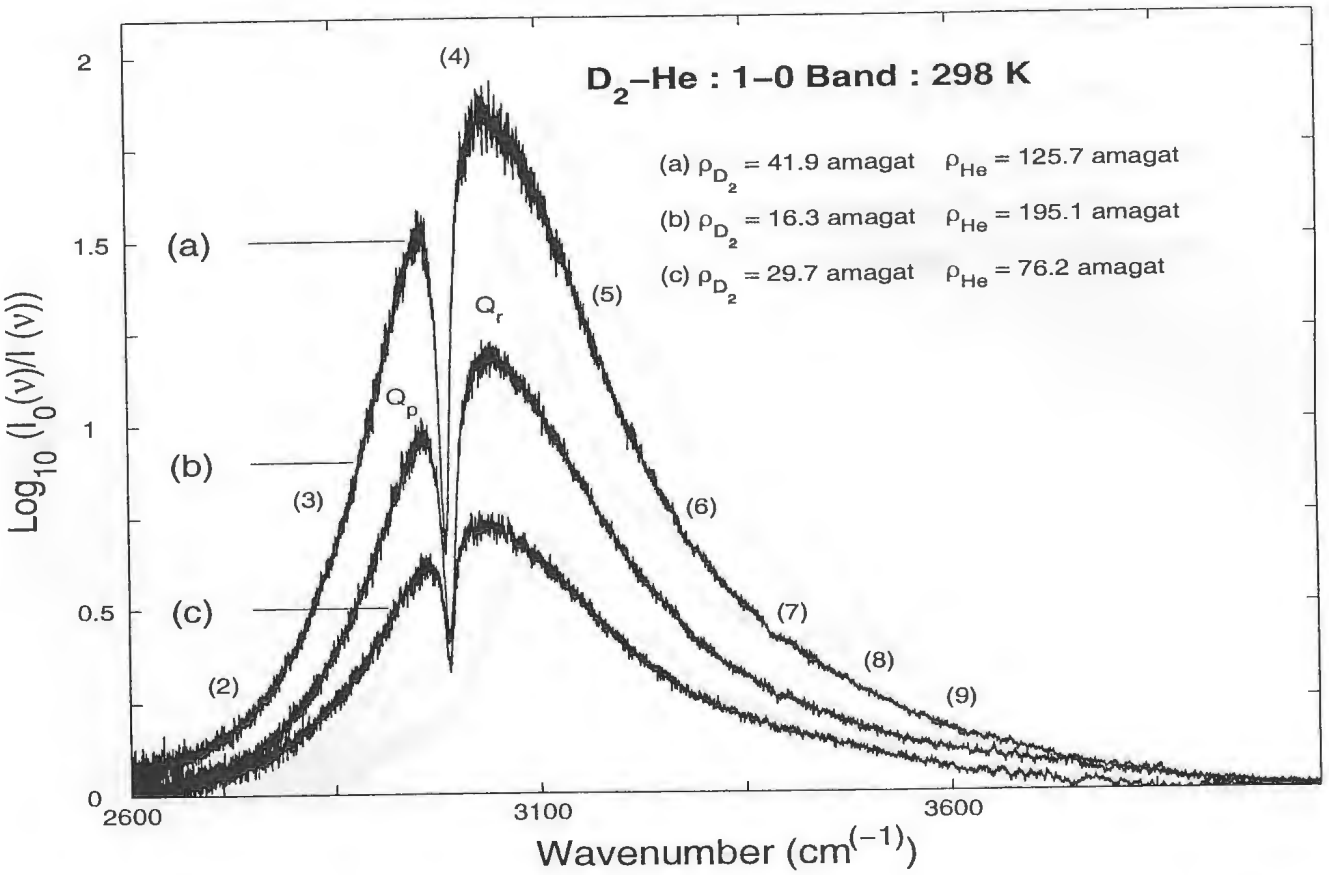

Figure 6.1: Profiles of the collision-induced enhancement absorption of D_2 in the fundamental band in D_2-He mixtures. See Table 6.2 for peak assignments.

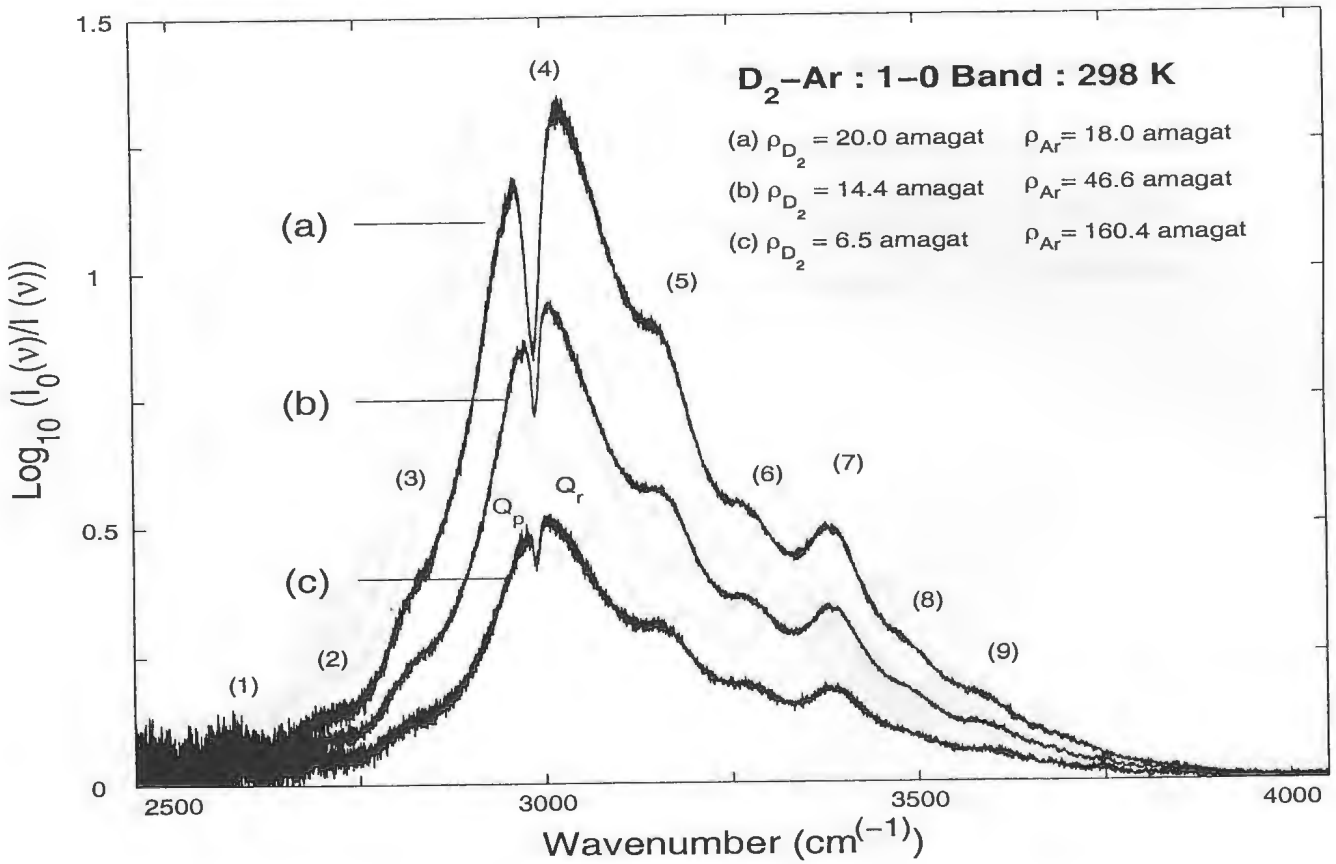

Figure 6.2: Profiles of the collision-induced enhancement absorption of D_2 in the fundamental band in D_2-Ar mixtures. See Table 6.2 for peak assignments.

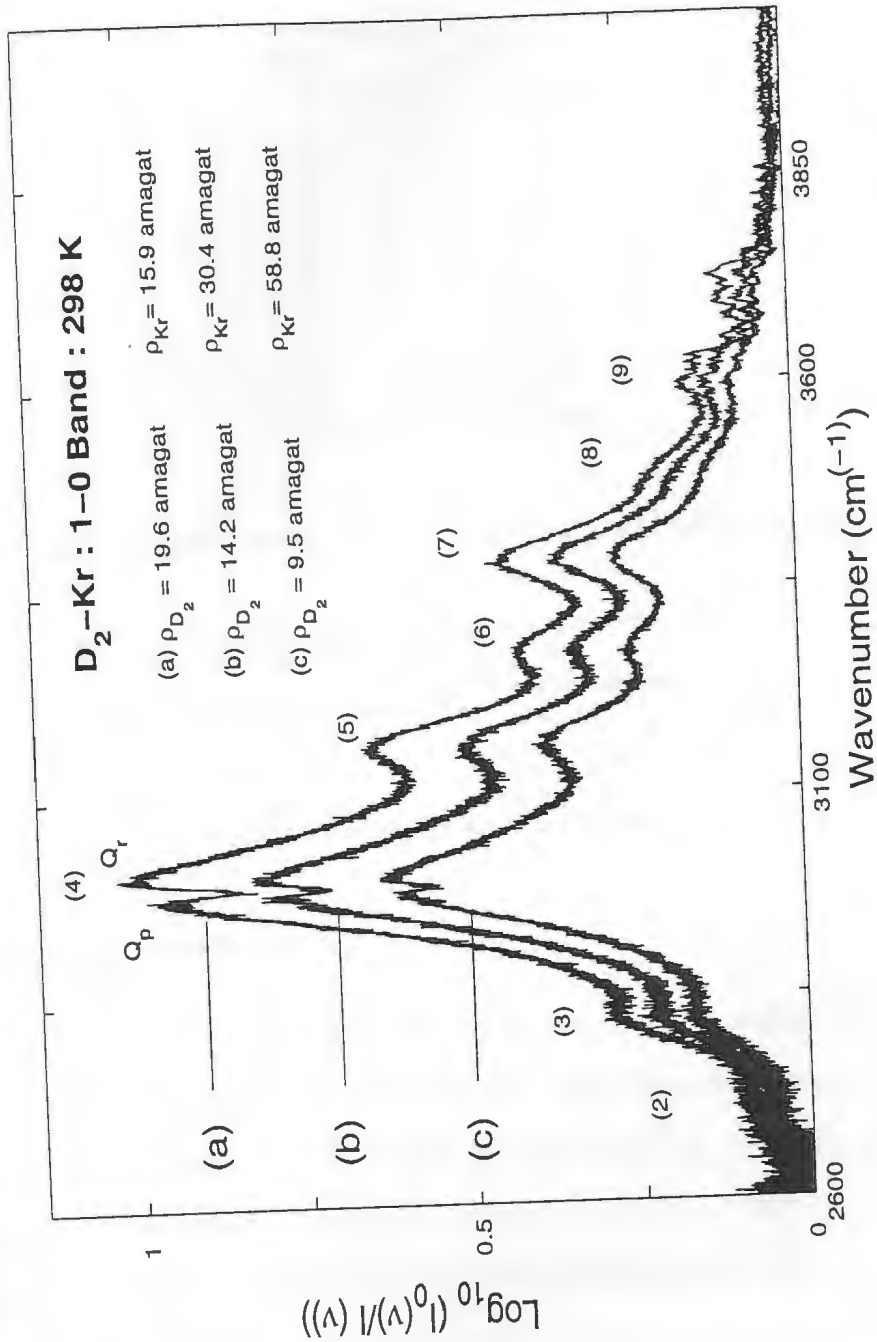

Figure 6.3: Profiles of the collision-induced enhancement absorption of D_2 in the fundamental band in D_2-Kr mixtures. See Table 6.2 for peak assignments.

Table 6.2: Assignment for the absorption peaks of the D_2 fundamental band enhanced by He, Ar, and Kr at 298 K.

Peak	Transitions
1	$O_1(2) + Q_0(J)$
2	$O_1(3) + Q_0(J)$
3	$O_1(4) + Q_0(J)$
4	$Q_1(J) + Q_0(J)$
5	$S_1(0) + Q_0(J)$
6	$S_1(1) + Q_0(J)$
7	$S_1(2) + Q_0(J)$
8	$S_1(3) + Q_0(J)$
9	$S_1(4) + Q_0(J)$

Table 6.3: Absorption coefficients for the fundamental band of D_2 enhanced by helium, argon, and krypton

Perturbing gas	α_{ab} (x10^{-3}) cm^{-2} amagat^{-2}
He	0.79 (1)
Ar	3.01 (4)
Kr	3.98 (4)

6.2 Absorption Coefficients

The spectral intensities were integrated to obtain the total absorption which was fitted using a linear regression model to determine the absorption coefficients. It was found that the influence of ternary absorption was not significant ($p < 0.05$) so only the binary coefficient was well determined. Values of the binary absorption coefficients so determined for the mixtures are given in Table 6.3. One of the main reasons for the extreme difference in the absorption coeffients is the polarizability matrix elements are quite different as noted in Section 2.4.

6.3 Profile Analysis

The generation of the synthetic profiles was carried out using a non linear least squares fitting procedure adapted from programs originally written by Gillard[17] with use of algorithms outlined in Numerical Recipes and refinements to the convergence criteria based on the work of Le Roy[59] and Watson[70]. Using the calculated intensities for the components and the Birnbaum Cohen lineshape function it was found that the agreement between the observed and fitted spectra was good, with standard errors of approximately 1 for the majority of the spectra. Comparisons of the synthetic profile and the experimental data are given in Figures 6.4, 6.5, and 6.6, for D_2-He, D_2-Ar and D_2-Kr respectively. The full list of parameters for all spectra for D_2-He is given in Table 6.4 to illustrate the distribution of the parameters in detail, similar spreads were found with D_2-Ar and D_2-Kr. The overlap induction halfwidth δ_d was quite consistent, the quadrupolar halfwidths δ_1 and δ_2 less so, and for a few of the spectra the δ_2 parameter diverged and the lineshape in effect was reduced to the dispersion lineshape as noted in section 2.5. The parameter δ_c was found to be density-dependent on the amount of helium, ($p < 0.05$), as shown in Figure 6.7, for D_2-He, Figure 6.8 for D_2-Ar mixtures. and Figure 6.9 for D_2-Kr mixtures. A weighted average was used to estimate the values for the overlap induction halfwidth δ_d, and quadrupolar halfwidths δ_1 and δ_2 with the results given in Table 6.5.

As noted previously the influence of the overlap induction mechanism is quite strong. Specifically the percentage absorption due to the two induction mechanisms is given in Table 6.6. A histogram for the quadrupolar percentage for D_2-He is given in Figure 6.3, to illustrate the spread is unskewed normal for the percentage absorption, the overlap spread was identical in behavior. The spread for the percentages in D_2-Ar and D_2-Kr followed the same distribution.

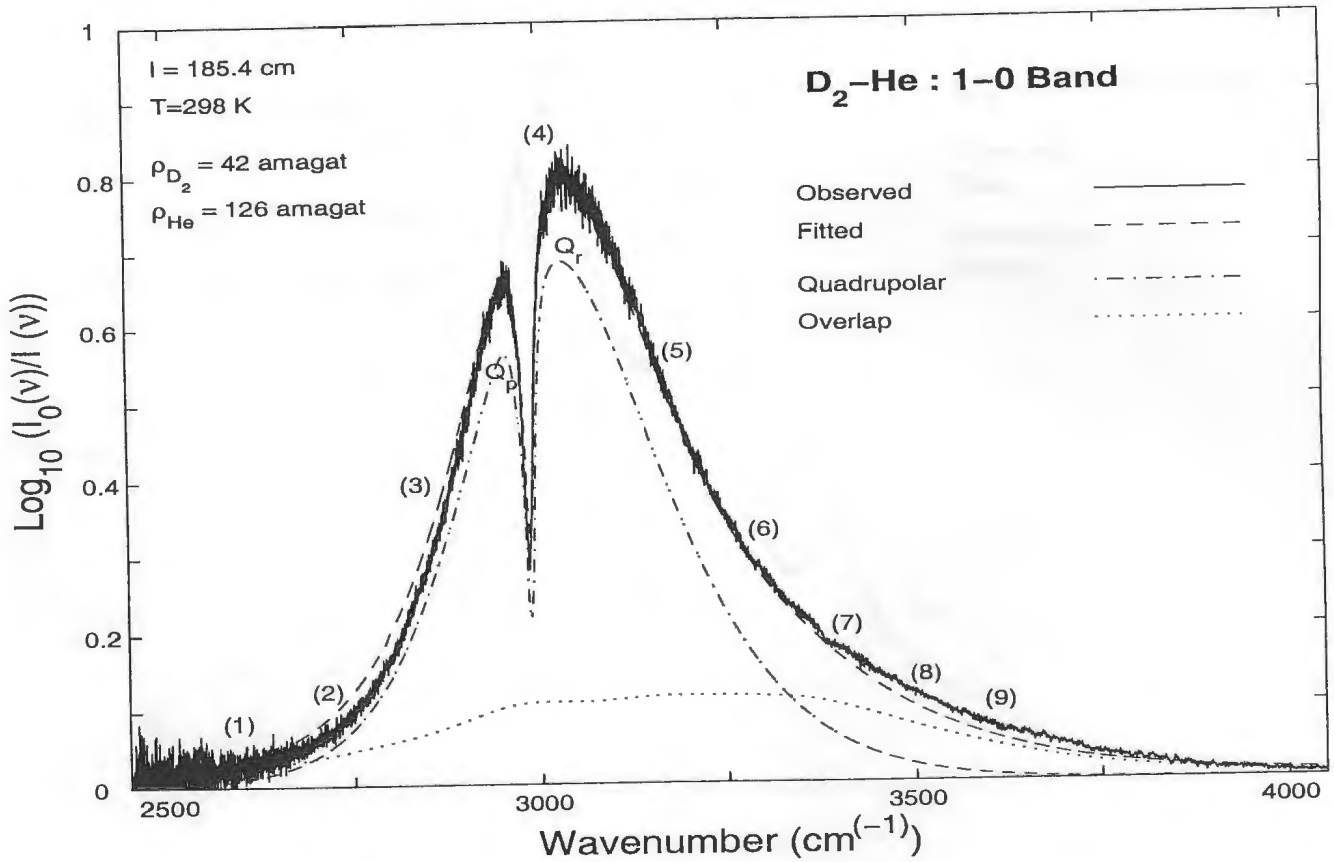

Figure 6.4: Analysis of an absorption profile for the enhancement of the fundamental band D_2-He at 298 K.

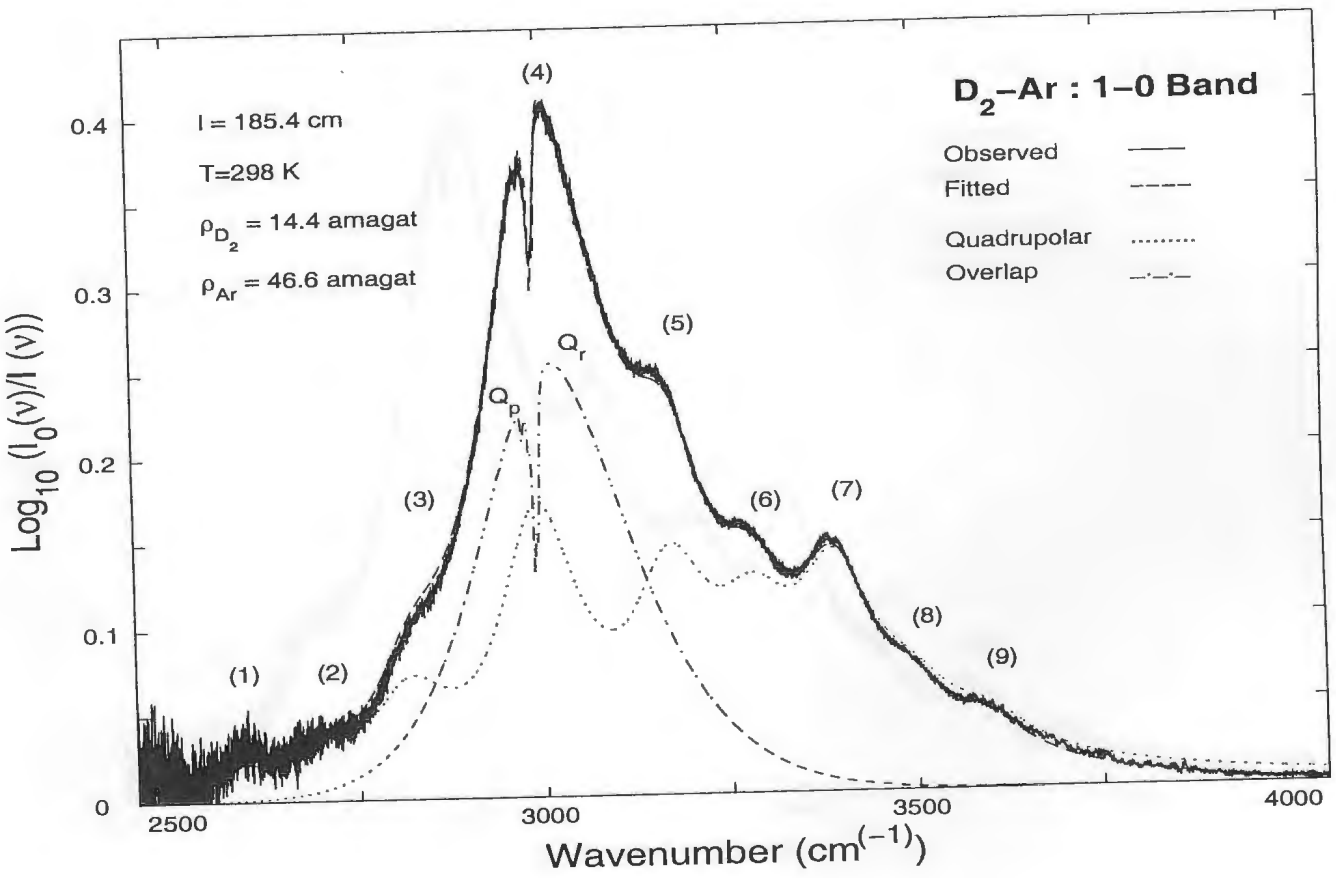

Figure 6.5: Analysis of an absorption profile for the enhancement of the fundamental band in D_2-Ar at 298 K.

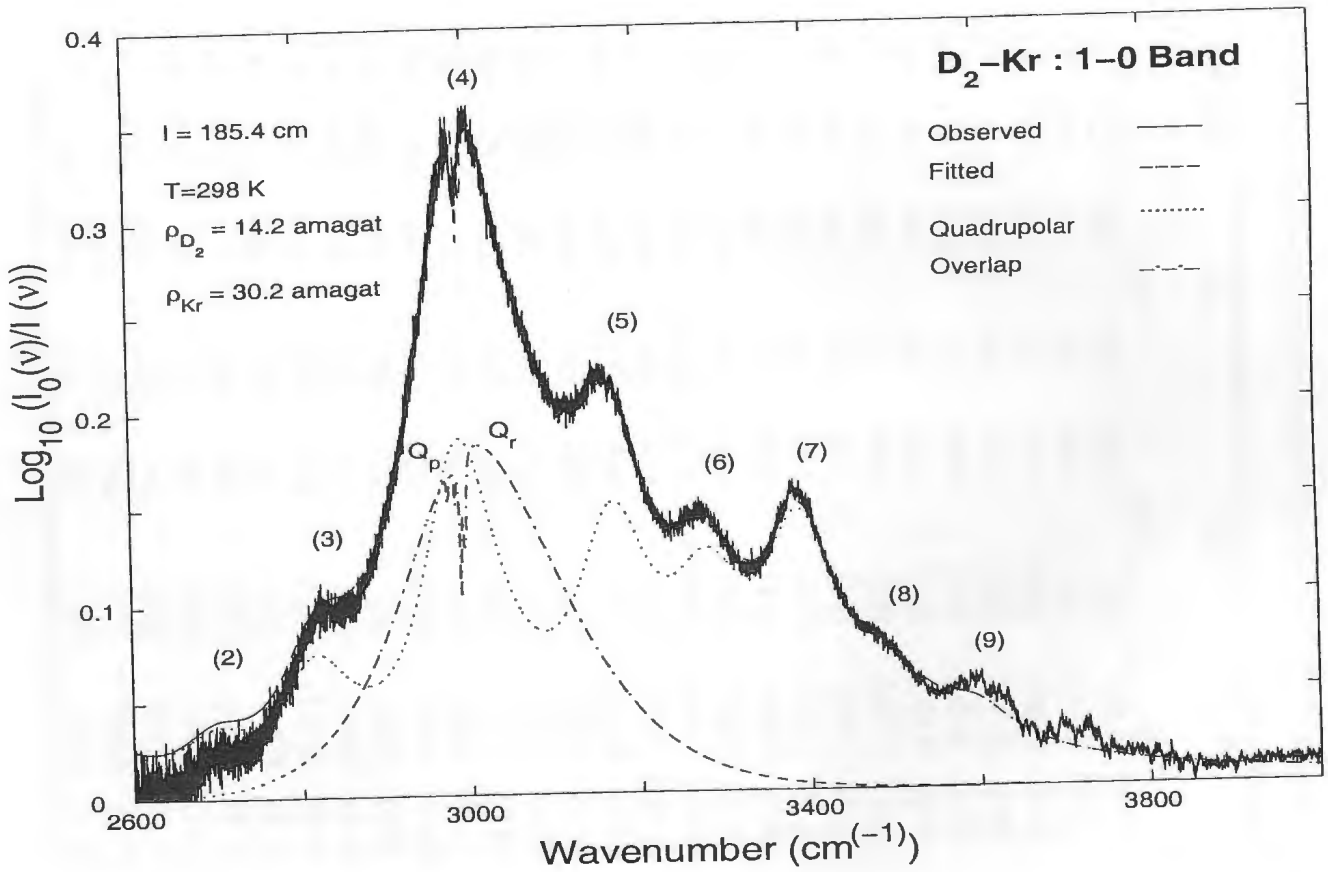

Figure 6.6: Analysis of an absorption profile for the enhancement of the fundamental band in D_2-Kr at 298 K.

Table 6.4: Lineshape parameters for the fundamental band of D_2 enhanced by helium.

Density		δ_{d1}		δ_{d2}		δ_d	
D_2	He						
amagat		cm^{-1}		cm^{-1}		cm^{-1}	
16	302	156	(2)	321	(8)	148.8	(0.1)
16	195	140	(2)	245	(8)	142.2	(0.2)
16	127	161	(3)	271	(14)	148.0	(0.2)
16	41	130	(16)	250	(96)	157.6	(0.8)
22	128	173	(3)	269	(10)	145.8	(0.1)
22	98	164	(4)	284	(16)	146.9	(0.2)
22	72	183	(5)	347	(26)	147.7	(0.2)
22	55	142	(4)	241	(18)	142.5	(0.3)
22	37	120	(6)	219	(31)	149.9	(0.5)
22	27	124	(7)	234	(43)	148.9	(0.6)
22	17	128	(16)	230	(85)	148.0	(1.1)
22	8	141	(140)	359	(1300)	146.6	(2.2)
30	168	149	(2)	284	(7)	149.1	(0.2)
30	114	149	(3)	268	(13)	148.9	(0.3)
30	76	130	(3)	356	(24)	149.5	(0.3)
30	46	121	(3)	241	(19)	148.8	(0.4)
30	28	115	(4)	239	(32)	152.0	(0.6)
30	17	95	(7)	247	(76)	159.1	(1.1)
30	8	130	(47)	250	(270)	167.5	(2.0)
42	126	153	(2)	270	(8)	149.2	(0.2)
42	106	149	(2)	281	(10)	148.7	(0.2)
42	82	150	(3)	273	(13)	147.9	(0.3)
42	62	158	(3)	262	(13)	146.3	(0.3)
42	50	150	(4)	273	(17)	148.7	(0.3)
42	39	133	(4)	246	(18)	144.2	(0.4)
42	27	241	(13)	214	(23)	151.4	(0.5)
42	17	184	(16)	189	(33)	149.6	(0.7)
42	9	130	(10)	250	(53)	148.1	(1.3)

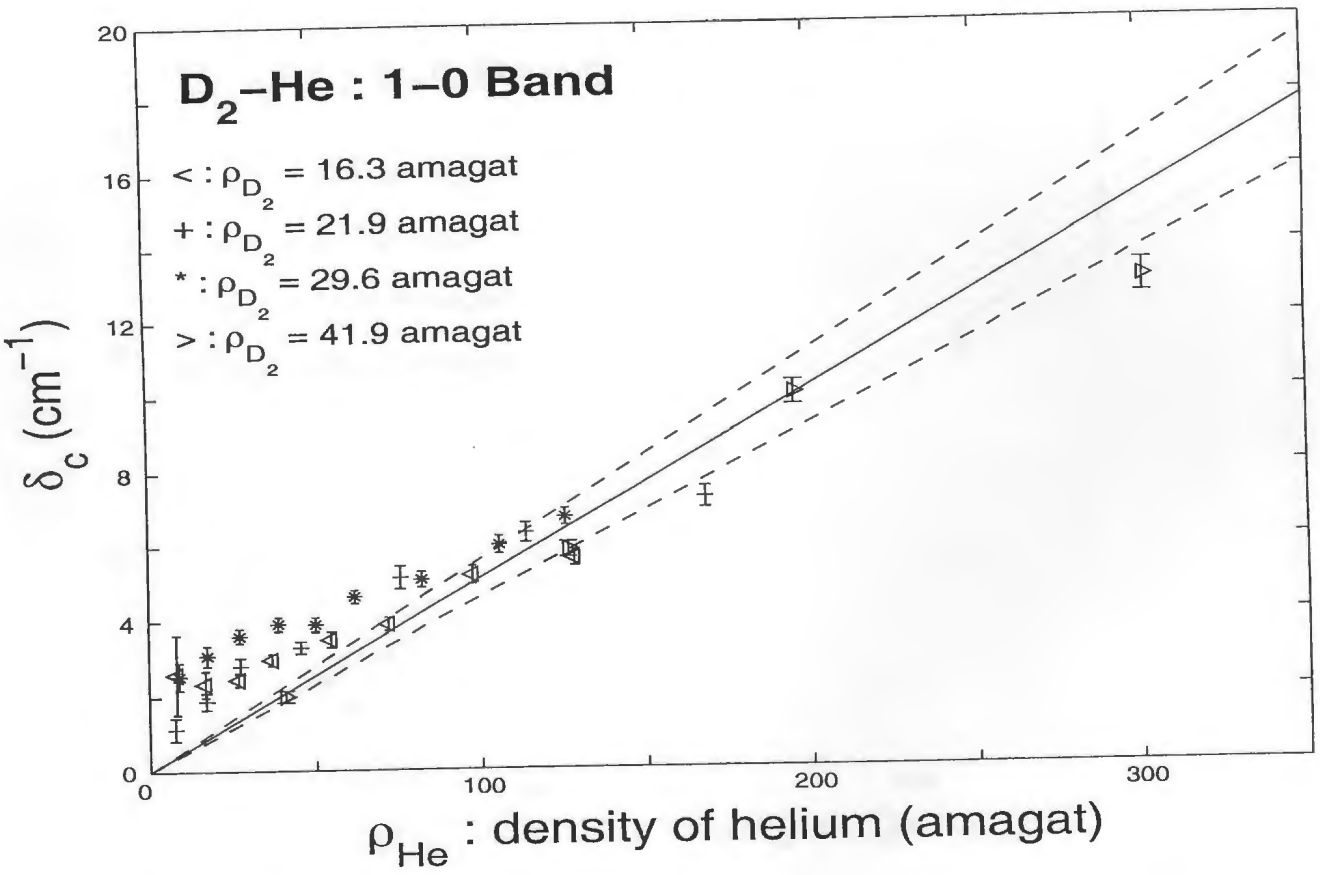

Figure 6.7: Dependence of the dip parameter δ_c on the density of helium in the fundamental band of D_2 in D_2-He mixtures.The dashed lines are the 95% confidence intervals for the slope.

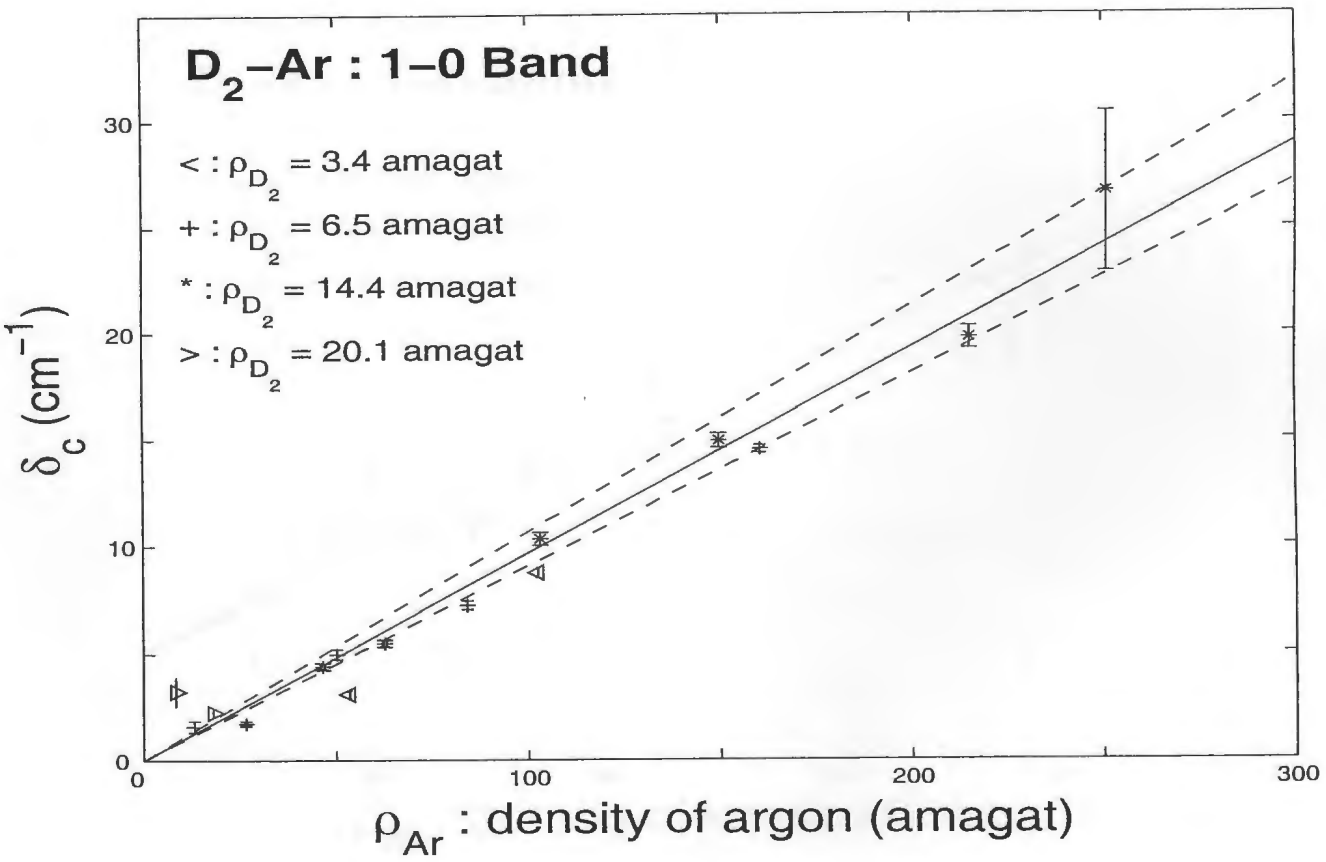

Figure 6.8: Dependence of the dip parameter δ_c on the density of argon in the fundamental band of D_2 in D_2-Ar mixtures. The dashed lines are the 95% confidence intervals for the slope

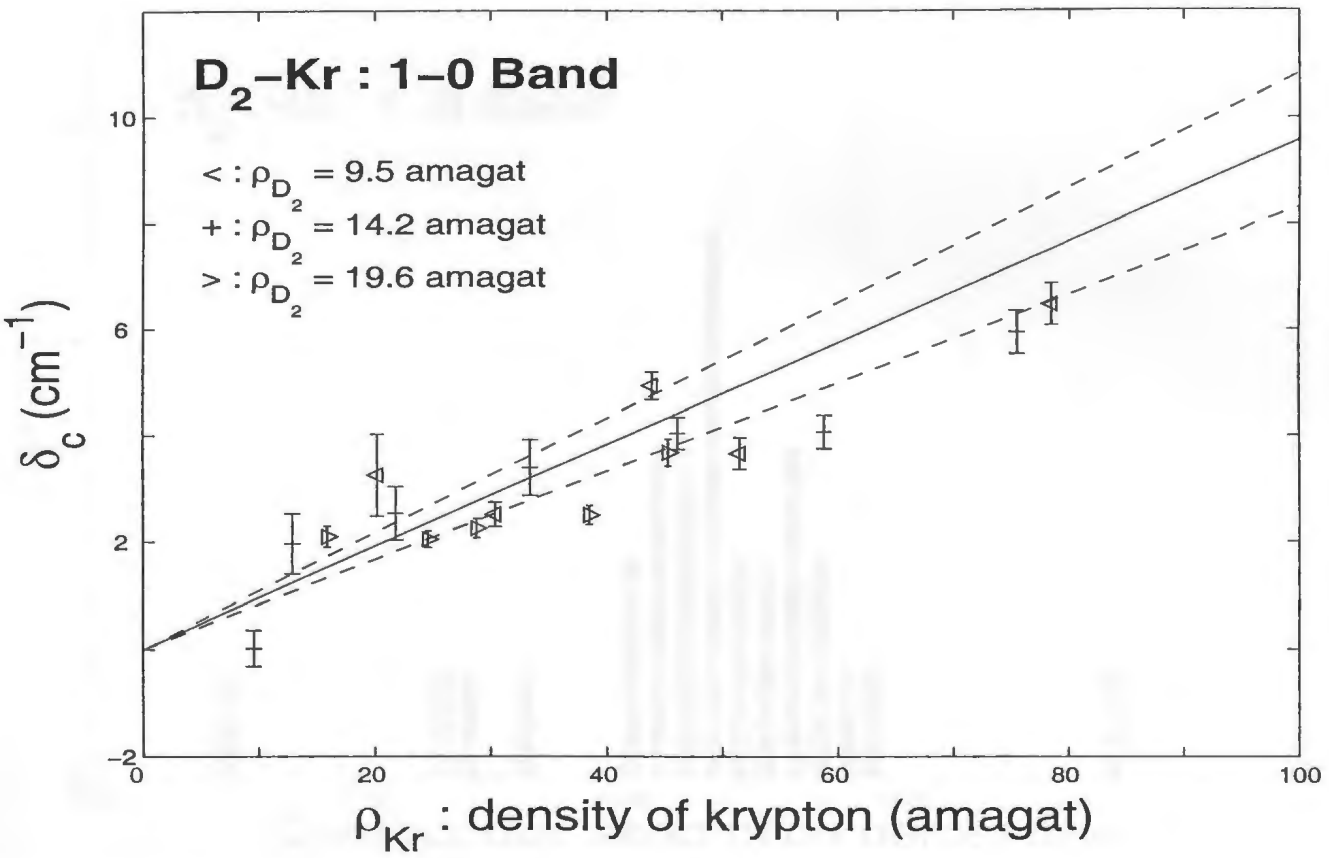

Figure 6.9: Dependence of the dip parameter δ_c on the density of krypton in the fundamental band of D_2 in D_2-Kr mixtures. The dashed lines are the 95% confidence intervals for the slope

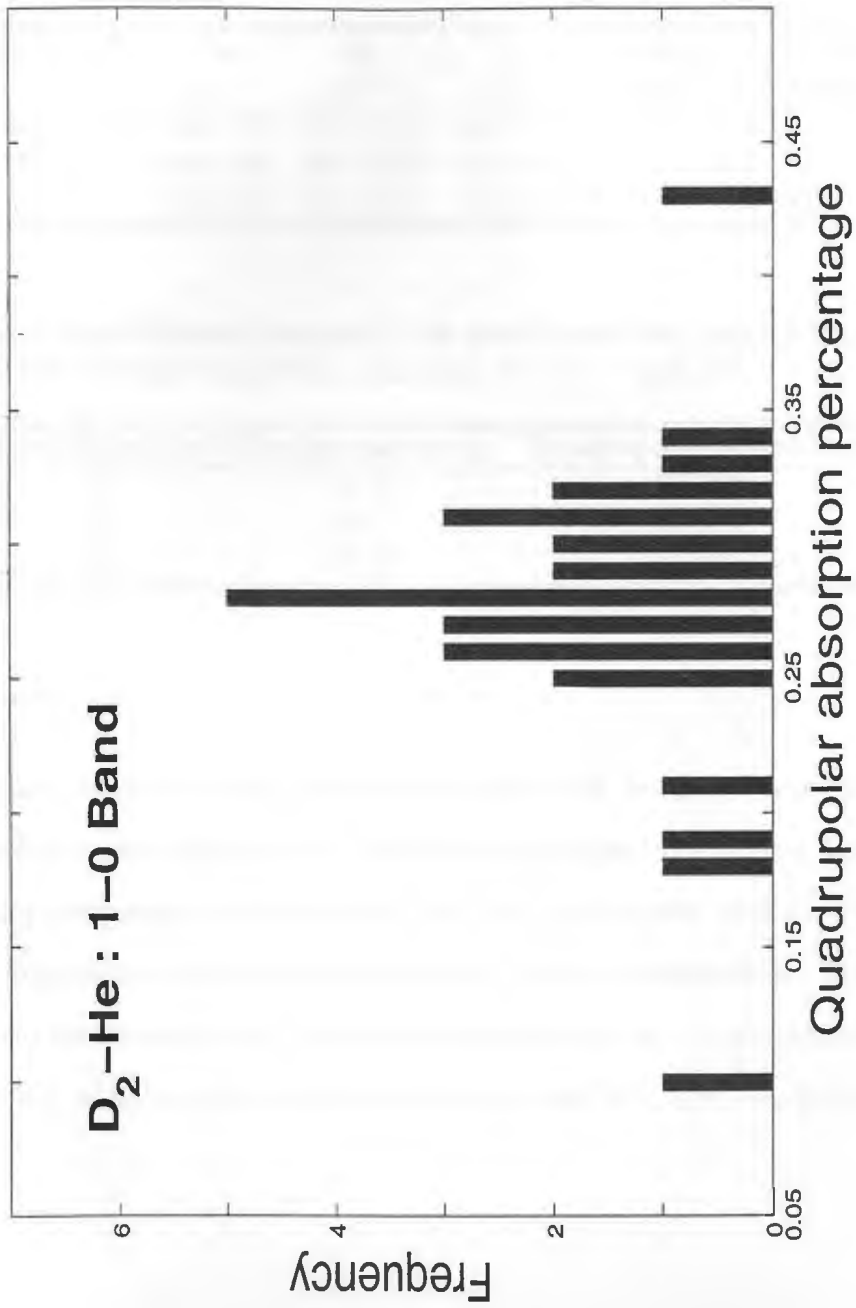

Figure 6.10: Histogram illustrating the normal spread of fractional quadrupolar absorption in the 1-0 band of D_2 in D_2-He mixtures.

Table 6.5: Lineshape parameters for the fundamental band of D_2 enhanced by helium, argon and krypton.

Perturbing Gas	δ_{d1} cm^{-1}	δ_{d2} cm^{-1}	δ_d cm^{-1}	slope for δ_c vs density ($x10^{-2}$ cm^{-1} $amagat^{-1}$)
He	148 (3)	273 (5)	148.8 (9)	5.0 (3)
Ar	64.8 (9)	291 (25)	112.8 (5)	9.7 (3)
Kr	54.6 (4)	319 (10)	109.3 (4)	9.6 (9)

Table 6.6: Percentage of absorption due to the quadrupolar and overlap induction mechanisms in the fundamental band of D_2 enhanced by He, Ar and Kr.

Perturbing Gas	Overlap percentage	Quadrupolar percentage
He	72 (2)	28 (1)
Ar	60 (1)	40 (1)
Kr	67 (1)	33 (1)

6.4 Conclusion

The enhancement spectra of the fundamental band of D_2 in mixtures with He, Ar, and Kr was studied at room temperature. The binary absorption coefficients were calculated along with the percentage of absorption from the quadrupolar and overlap induction mechanisms. Appropriate lineshape functions were used to determine the synthetic profile and thus obtain the characteristic lineshape parameters and relevant density dependence. The parameter δ_c of the overlap induction lineshape was found to be density-dependent.

Chapter 7

Conclusions

A brief summary of the work previously described in this thesis as well as a short commentary on possible refinements to the methods and the experimental setup and possible future avenues of exploration are described in the rest of this chapter.

7.1 First overtone band of hydrogen

Chapter 4 was a refinement to the lineshape analysis performed by van Nostrand on the 2-0 band of hydrogen. With a method first proposed by Gillard for the work on the 2-0 band of deuterium and later used by Xiang on the analysis of the 3-0 band of hydrogen, van Nostrand used a multiplicative "fudge factor" adjustment to the calculated spectral intensities to allow the synthetic profiles to match with the experimental profiles.

Chapter 4 examined this "fudge factor" in detail which was previously calculated as an average correction for all spectra, but in this chapter it was included as a parameter in the lineshape analysis which allowed it to be refined to an individual "fudge factor" for each absorption profile at a given density and temperature. This made it possible to determine a definite correlation between the magnitude of the "fudge factor" and the density and temperature of the gas.

Specifically the "fudge factor" has a linear dependence on the density of hydrogen and it increased as the density of the system decreased; however it did not extrapolate back to one (which would be no correction) at zero gas density. The "fudge factor" also tended to increase with decreasing temperature; however as only three temperatures (77, 201

and 295 K) were available, there was not enough temperature data to give a statistically sound correlation.

This "fudge factor" correction to the 2-0 calculated intensities in the overtone band of H_2 is proposed to account for a mixed term between the anisotropic overlap term and the quadrupolar induction term which gives a negative contribution to the total intensity of the 2-0 transitions.

7.2 The fundamental band of D_2 in D_2-N_2 and D_2-CO mixtures

The CIA fundamental band of D_2 in D_2-N_2 and D_2-CO mixtures was found to show the expected properties of collision induced absorption such as the broad peaks and relatively low intensities compared to the allowed spectra. In addition, the absorption profiles showed the specific Q_P and Q_R splitting due to the presence of the overlap induction mechanism.

The integrated absorption of the band was found to have a slight but meaningful ternary coefficient showing the influence of triple collisions on the total intensity which was characterized by the ternary absorption coefficient, α_{2ab}, representing collisions of the type D_2-D_2-X, where X is either N_2 or CO. The binary absorption coefficients were also calculated.

The spectra were fitted with a number of semi-empirical lineshapes and were best fit by the dispersion lineshape which accounted well for the spectral intensity except for a small discrepancy in the region 3400 cm^{-1}, which accounts approximately for one percent of of the total intensity. This discrepancy between the experimental and synthetic spectra was not reduced by the more complex lineshapes such as the BC lineshape as the δ_2 parameter diverged to infinity which reduced the BC lineshape to the form of the dispersion lineshape.

As these spectra did not contain both the 1-1 and 2-0 transitions as presented in the work on the 2-0 band of hydrogen in Chapter 4 a "fudge factor" was not necessary to give a satisfactory fit of the synthetic profiles to the experimental profiles.

7.3 The fundamental band of D_2 in binary mixtures D_2-He, D_2-Ar, and D_2-Kr.

The CIA spectra of the fundamental band of D_2 enhanced by helium, argon, and krypton showed the same general structure for collision induced absorption spectra of D_2-N_2 and D_2-CO mixtures as shown in Chapter 5. The spectra of Chapter 6 showed the same broad features characteristic of CIA and the specific dip due to the overlap induction mechanism found in the spectra of the fundamental and first overtone bands. The main difference between the spectra in Chapter 6 and the spectra presented in Chapter 5 is that in Chapter 6 mixtures produced enhancement spectra and thus the perturbers only underwent orientational transitions as they lack a quadrupole moment. The spectra of Chapter 5 have perturbers with quadrupole moments and thus N_2 and CO can undergo rotational transitions along with the vibration-rotation transitions of the deuterium molecule.

The results of the analysis showed a significant difference in these spectra in regard to the integrated absorption as the ternary absorption coefficient was not found to be significant for the enhancement spectra of Chapter 6 though it was for the D_2-N_2 and D_2-CO mixtures of Chapter 5. In the lineshape fitting a much better agreement to the experimental data was achieved as compared to the work presented in Chapter 5 which showed more discrepancy between the experimental and synthetic profiles, particularly in the wings. This improvement is due to three factors, first the lack of a significant ternary interaction gave a better estimate of the $\tilde{A}_{IM}$ factor in equation 2.39, second the enhancement spectra do not have the level of approximation of the D_2-N_2 and D_2-CO

intensities which assumed a constant quadrupole and polarizability for the perturbing gases of which the J dependence was not known which added a level of uncertainly to the calculations. Finally many of the experimental methods had been refined since the D_2-N_2 and D_2-CO data were collected which allowed the enhancement spectra of D_2-He, D_2-Ar, and D_2-Kr mixtures to be collected and reduced with a much higher precision. In particular there was no smoothing of the experimental data which illustrates the level of noise in a meaningful way and the much better tapering to zero of the profiles in the wings due to the refinements of the procedures used to deduce the absorption coefficient from the recorded spectral intensities as described in Section 3.7.

7.4 Possible suggestions for improvement

It is suggested that the experimental setup could be improved in a few ways. A number of alternative light sources were used during the course of the work as the traditional lamps used have shorter lifetimes. There are a number of very long lifetime lamps available, such as regular car headlights; however, the filament image is not suitable and thus the intensities obtained were too low. A custom version of the same basic lamp would solve the problem of frequent lamp replacements which produce significant down time because as the lamp is replaced new base spectra have to be recorded so the mixtures have to be started over from the base density.

Secondly the greatest source of uncertainty in the spectral frequency is the lack of definite knowledge of the step counts. It was possible for the spectra which were to be averaged to be different by one to two step counts due to a number of factors such as load on the line which could cause the motor controller to skip. This was dealt with by the methods as described in Section 3.7 and this could be refined if the exact angular rotation of the screw was recorded independently and there are devices in the market

which would allow such a determination to be made. This would not functionally change the nature of the information which would be obtained, but would just allow slightly more precision, especially in calibration.

For the analysis of the experimental data, the main refinement would be a shift away from mean centered analysis and towards median based statistics which would be a major undertaking as it would require all affected programs to be completely recoded. Some of the programs for the data analysis were shifted to median based statistics during the course of the present work, but some are still mean based including the main program for the fitting of the spectral data.

In terms of experimental work, an obvious extension would be to use the data of the 2-0 band of D_2 recorded by Gillard and the data of the 3-0 band of H_2 recorded by Xiang and perform a similar "fudge factor" analysis as was carried out on the 2-0 hydrogen data of van Nostrand and verify if the correlation holds for the other two gases. Additional temperature data could also be collected using a boiling water bath for example to determine if a systematic connection could be found between the "fudge factor" and temperature.

Bibliography

[1] J. Topping. *Errors of Observation and their treatment.* The institute of Physics, London, 1955.

[2] M. F. Crawford, H. L. Welsh and J. L. Locke . *Phys. Rev.*, 75:1607, 1949.

[3] J. Van Kranendonk. *Physica*, 24:347–62, 1958.

[4] L. Frommhold. *Collision Induced Absorption in Gases.* (Cambridge University Press, Cambridge, 1993).

[5] H. L. Welsh. *in MTP International Review of Science, Physical Chemistry, Vol. 3, Spectroscopy.* edited by D. Ramsay (Butterworths, London, 1972).

[6] S. P. Reddy. *in Phenomena Induced by Intermolecular Interactions.* edited by G. Birnbaum (Plenum, New York, 1985).

[7] J. Van Kranendonk. *Physica*, 23:825, 1957.

[8] J. Van Kranendonk. *Physica*, 25:337–62, 1959.

[9] J. Van Kranendonk. *Physica*, 73:156, 1974.

[10] J. C. Lewis. *Phenomena Induced by Intermolecular Interactions, edited by G. Birnbaum (Plenum Publishing Corporation, New York)*, page 215, 1985.

[11] J. D. Poll. *Proceedings of the International School of Physics Enrico Fermi, Course LXXV, Intermolecular Spectroscopy and Dynamical Properties of Dense Systems.* North-Holland Publishing Company, New York, 1980.

[12] G. Birnbaum and E. R. Cohen. *Can. J. Phys.*, 54:593, 1976.

[13] G. Birnbaum, B. Guillot, and S. Bratos. *Adv. Chem. Phys.*, 51:49, 1982.

[14] N. H. Rich and A. R. W. McKellar. *Can. J. Phys.*, 54:486, 1976.

[15] S.P. Reddy, G. Varghese, and C. Stamp. *J. Quant. Spectrosc. Radiat. Transfer*, 87:387–397, 2004.

[16] E. van Nostrand. Master's thesis, Memorial University of Newfoundland, 1983.

[17] P. G. Gillard. PhD thesis, Memorial University of Newfoundland, 1983.

[18] J. D. Poll and J. Van Kranendonk. *Can. J. Phys.*, 39:189, 1961.

[19] J. D. Poll and J. L. Hunt. *Can. J. Phys.*, 54:461, 1976.

[20] M. E. Rose. *Elementary Theory of Angular Momentum.* John Wiley & Sons, Inc., New York, 1957.

[21] J. D. Poll, H. L. Hunt, and J. W. Mactaggart. *Can. J. Phys.*, 53:954, 1975.

[22] J. D. Poll and H. L. Hunt. *Can. J. Phys.*, 54:461–470, 1976.

[23] R.D.G. Prasad,P.G. Gillard,S. P. Reddy. *J. Chem. Phys.*, 107:4906–4910, 1997.

[24] J. D. Poll. *Proceedings I.A.U. Symposium 40 on Planetary Atmospheres (Reidel, Dordrecht)*, page 384, 1971.

[25] G. Karl, J. D. Poll, and L. Wolniewicz. *Can. J. Phys.*, 19:1781, 1975.

[26] R. M. Hill and W.V. Smith. *Phys. Rev.*, 82:451, 1951.

[27] A. J. Bridge, and A. D. Buckingham. *J. Chem. Phys.*, 40:2733–4, 1964.

[28] J.O. Hirschfelder, C. F. Curtiss, and R. B. Bird. *Molecular Theory of Gases and Liquids.* John Wiley and Sons Inc., New York, 1954.

[29] J. Van Kranendonk. *Can. J. Phys.*, 46:1173–9, 1968.

[30] S. P. Reddy, A. Sen, and R. D. G. Prasad. *J. Chem. Phys.*, 72:6102, 1980.

[31] J. C. Lewis, and J. A. Tjon. *Physica A*, 91:161, 1978.

[32] J. C. Lewis. *private communication.*

[33] J. C. Lewis. *Spectral Lineshapes.* edited by Roger M Herman and published by the American Institute of Physics, 1999.

[34] P. A. Egelstaff. *Proceedings Symposium on Inelastic Neutron Scattering, IAEA.* Vienna, 1960.

[35] A. Borysow, and L. Frommhold. *Astrophys. J.*, 311:1043, 1986.

[36] A. Borysow, L. Frommhold, and W. Meyer. *Physica A*, 40:6931–6949, 1989.

[37] W. Meyer, A. Borysow, and L. Frommhold. *Physica A*, 47:4065–4077, 1993.

[38] Y. Fu, C. Zheng, and A. Borysow. *J. Quant. Spectrosc. Radiat. Transfer*, 67:4:303, 2000.

[39] A. Borysow, L. Frommhold, and W. Meyer. *Physica A*, 41:264–270, 1990.

[40] J. Boissoles, R. H. Tipping, and C. Boulet. *J. Quant. Spectrosc. Radiat. Transfer*, 51:615–627, 1994.

[41] S. P. Reddy, F. Xiang, G. Varghese. *Phys. Rev. Lett.*, 74:3:367–369, 1995.

[42] M. Massimo, and L. Frommhold. *Phys. Rev. Lett.*, 74:3:363–366, 1995.

[43] R. B. Bishop. Master's thesis, Memorial University of Newfoundland, 1966.

[44] C. Stamp. Master's thesis, Memorial University of Newfoundland, 1999.

[45] James T. McGlave, and P. George Benson. *Statistics for Business and Economics.* Dellen Publishing Company, San Franisco, 1991.

[46] Philip R. Bevington, and D. Keith Robinson. *Error analysis for the physical sciences.* McGraw-Hill, Inc., New York, 1992.

[47] E.J. Le Roy. *Chemical Physics Research Report*, CP-629, 1997.

[48] S. P. Reddy and C. W. Cho. *Can. J. Phys.*, 43:2331, 1965.

[49] P. Gillard. *Private Communication.*

[50] H. W. Press, B. P. Flannery, S. A. Teukolsky, W. T. Vetterling. *Numerical Recipes The art of Scientific Computing.* Cambridge University Press, Cambridge, 1986.

[51] I. M. Sobol. *The Monte Carlo Method.* MIR, Moscow, 1975.

[52] Ilya M. Sobol, Alya Sobol, I. M. Sobol. *A Primer for the Monte Carlo Method.* CRC Press, Florida, U.S.A, 1994.

[53] A. R. H. Cole. *Tables of Wavenumbers for the Calibration of Infrared Spectrometers.* Pergamon Press Inc., New York, 1977.

[54] A. R. Downie,M. C. Magoon, Thomasine Purcell, and Bryce Crawford, Jr. . *J. Opt. Soc. Am.*, 43:11:941–951, 1953.

[55] Cameron Reed. *Am. J. Phys.*, 57:642–646, 1989.

[56] Derek York, Norman M. Evenson. *Am. J. Phys.*, 72:367–375, 2004.

[57] F. Xiang. Master's thesis, Memorial University of Newfoundland, 1995.

[58] James P. A. Youden. Bachelor's Thesis (Honours), Memorial University of Newfoundland, 1985.

[59] R. Le Roy. Paper FB10. 52nd Ohio State University International Symposiumm on Molecular Spectroscopy, 1997.

[60] A. Watanabe, and H. L. Welsh. *Can. J. Phys.*, 43:818–28, 1965.

[61] R.J. Penny, R.D.G. Prasad, and S.P. Reddy. *Can. J. Phys.*, 77(1):131–41, 1982.

[62] P.G. Gillard, R.D.G. Prasad, and S. P. Reddy. *J. Chem. Phys.*, 81:3458–62, 1987.

[63] S.T. Pai, S. P. Reddy and C. W. Cho. *Can. J. Phys.*, 44:2893–903, 1966.

[64] W. E. Russell, S.P. Reddy,and C. W. Cho. *J. Mol. Spect.*, 52:72–81, 1974.

[65] E. K. Plyler, and L. R. Blaine. and M. Nowak. *J. Res. Nat. Bur. Stand.*, 58:195–200, 1957.

[66] A. Michels, and M. Goudeket. *Physica*, 8:352–60, 1941.

[67] A. Michels, H. Wouters, and J. De Bohr. *Physica*, 1:587, 1934.

[68] J.G. Hust, and R.B. Stewart. *NBS Technical Note*, No. 2002, 1963.

[69] A. R. W. McKellar, and T.Oka. *Can. J. Phys.*, 51:1315–20, 1978.

[70] J. K. G. Watson. *private communication*, 1994.